



**Politecnico  
di Torino**

**POLITECNICO DI TORINO**

---

DEPARTMENT OF STRUCTURAL, GEOTECHNICAL AND BUILDING  
ENGINEERING  
Course of Civil Engineering

MASTER'S DEGREE THESIS

**ELASTIC-PLASTIC-SOFTENING EVOLUTIONARY ANALYSIS OF  
MASONRY ARCHES:  
THE APPLICATION OF THE COHESIVE/OVERLAPPING  
CRACK MODEL**

Supervisor:  
**Prof. Alberto Carpinteri**

Candidate:  
**Giulia Delo**

Co-supervisors:  
**Prof. Stefano Mariani**  
**Dr. Eng. Federico Accornero**  
**Eng. Renato Cafarelli**

---

**Academic Year: 2020-2021**



# Acknowledgements

I wish to express my gratitude to Prof. Alberto Carpinteri, Prof. Stefano Mariani, Dr. Federico Accornero and Eng. Renato Cafarelli for their support in the realisation of this Thesis.



# Abstract

The structural behaviour of masonry arches has been deeply investigated over the centuries, starting with the first theoretical approach by Hook in 1675. Later, with the introduction of the Theory of Elasticity, the graphical procedure illustrated by Méry (1840) gained high recognition in the field of arch design. More recently, following the formulation by Heyman (1966), which is based on Plastic Theory concepts, the modern Limit Analysis was introduced. Nevertheless, all these models are not able to describe the behaviour of arch structures in a comprehensive way, since they are not capable to predict the damage evolutionary process that affects the load bearing capacity of masonry arches.

Recent studies have provided a model to analyse masonry arches based on Linear Elastic Fracture Mechanics, leading to the definition of the fracturing benefit, which, analogously to the plastic benefit for Limit Analysis, describes how the arch thrust line is affected by crack formation and the maximum admissible load evaluated by means of Fracture Mechanics is larger than the load predicted by Theory of Elasticity. In this framework, the Cohesive/Overlapping Crack Model is able to simulate the transition between cracking or crushing failure in the arch cross section, highlighting a strong correlation between the structural behaviour of the arch and its size. In the present Master Thesis, the Cohesive/Overlapping Crack Model is extended to the study of masonry or plain concrete arch structures, which are subjected to off-center compression. Multi-cracking and multi-crushing damage phenomena are simulated by means of the Crack Length Control Scheme, in order to obtain a complete load history of the arch structure. This Non-linear Fracture Mechanics model reveals a high capability in predicting the elastic-plastic-softening behaviour of the arch as well as the local mechanical

instabilities, such as snap-back and snap-through, occurring during the post-cracking regime. In this framework, the model is able to highlight an analogy between arches curvature and the bridging effects provided by reinforcement in reinforced concrete structures.

In the first part of this Thesis, the main models proposed in the scientific literature for arch analysis are briefly summarised. Then, the principles of Nonlinear Fracture Mechanics are introduced, with particular focus on the Cohesive/Overlapping Crack Model. In the third part of the Thesis, the new model for arch analysis is introduced and a description of the adopted numerical procedures is provided. In the last part, some parametric analyses about scale effects in masonry arches are reported together with the results obtained for the Mosca Bridge case-study. Finally, some future developments and applications of the model are presented.



# Contents

<b>Acknowledgements</b>	<b>i</b>
<b>Abstract</b>	<b>iii</b>
<b>Introduction</b>	<b>1</b>
<b>1 Masonry arches off-centre compression</b>	<b>3</b>
<b>2 Nonlinear fracture mechanics</b>	<b>17</b>
2.1 The cohesive crack model . . . . .	18
2.2 Carpinteri algorithm . . . . .	24
<b>3 The crushing issue and the overlapping crack model</b>	<b>29</b>
3.1 The overlapping crack model . . . . .	31
3.2 Uniaxial compression test . . . . .	34
<b>4 The cohesive/overlapping crack model</b>	<b>37</b>
<b>5 A new algorithm for arches analysis</b>	<b>44</b>
5.1 Zero-thickness elements . . . . .	45
5.2 Algorithm definition . . . . .	49
<b>6 Description of the routines</b>	<b>55</b>
6.1 The routine Master.py . . . . .	55
6.2 The routine MeshGenerator.py . . . . .	57
6.3 The file arch.pro and the related sub-routines . . . . .	57
6.4 The routine CohesiveOverlappingSolver.py . . . . .	59
6.5 The routine MeshManagement.py . . . . .	60

6.6	The routine OutputDiagrams.py . . . . .	62
<b>7</b>	<b>Algorithm results</b>	<b>63</b>
7.1	Material mechanical properties . . . . .	63
7.2	Scale effects analysis . . . . .	65
7.3	The Mosca bridge case study . . . . .	81
<b>8</b>	<b>Conclusions</b>	<b>92</b>
	<b>List of figures</b>	<b>94</b>
	<b>Bibliography</b>	<b>97</b>



# Introduction

Masonry arches are widespread structures in the historical and architectural heritage. The arch shape has been broadly used in the construction of masonry bridges throughout the civilised world. Indeed, there are many examples of such bridges, dating back to the period of the Roman Empire but still in service today. Therefore, an accurate evaluation of their structural behaviour becomes of primary importance.

Various studies tried to analyse arches structural response to introduce new critical approaches for their design and safety assessment, starting from purely geometric and empiric ones, which were introduced yet in the Seventeenth Century, and early kinematic approaches, which arose in the Eighteenth Century. A widely held method has been proposed by Méry [1]. According to Navier's studies in 1833 [2]. It introduced the arch Elastic Analysis, based on the concept of line of thrust. More recently, instead, a Limit Plastic Analysis has been spread, following Heyman's theories [3–5]. However, these traditional methods only provide a partial understanding of the arch structural behaviour. The Elastic Analysis provides a conservative load limit, and the Plastic Analysis can hardly be used to describe the response and damage in a structure subjected to moderate or service loads.

For these structures, it was observed that the cracking process drives the collapse. Therefore, it is crucial to study them through Fracture Mechanics Theory to assess their actual loading capacity. Recent studies by Carpinteri *et al.* [6] proposed a method based on the Linear Elastic Fracture Mechanics (LEFM) that enables the assessment of the damaging process in arches with a step-by-step procedure. It investigates the arches behaviour after the overcoming of elastic limits but before the reaching of plastic limits. Consequently, it defines a “fracturing benefit” from the comparison of the results

with the limits provided by Elasticity theory.

The present work aims to extend these studies to the field of Non-Linear Fracture Mechanics, with the application of the Cohesive/Overlapping Crack Model, to perform a more accurate masonry arch evolutionary analysis, taking into account the cohesive crack growth and the failure for crushing of the masonry block. The Cohesive/Overlapping algorithm was introduced by Carpinteri *et al.* [7] and Corrado [8], based on previous studies by Carpinteri [9–11].

It is still based on a step-by-step procedure, in which the loading process is evaluated through the advancement of a cohesive fictitious crack tip and an overlapping fictitious crack tip. The final goal is the development of a numerical code in which to implement the Cohesive/Overlapping algorithm in the cross sections of a masonry arch bridge. It is done through the positioning of specific “zero thickness elements” in the Finite Element Method (FEM) framework, which allow for modelling the evolution of the crack in the arch.

# Chapter 1

## Masonry arches off-centre compression

The structural behaviour of masonry arches has been investigated using different approaches developed over the centuries. Firstly, arches design was solely based on their geometrical characteristics [12, 13], finding a solution to the static problem. One of the most used empirical approaches follows the statement written by Robert Hooke in 1675 in the form of an anagram: “Ut pendet continuum flexile, sic stabit contiguum rigidum inverse” [**hooke**], which translates as, “As hangs the flexible line, so but inverted will stand the rigid arch”.

It generalises the idea of the catenary shape that a string takes under a set of loads. If rigidified and inverted, this shape illustrates a path of compressive forces for an arched structure to support the same set of inverted loads, as stated by Poleni [14] in his studies on the Dome of St. Peter’s (Figures 1.1 - 1.2 ). The ideal funicular shape was found experimentally by hanging weights from a string [15].

Graphical analysis has been considerably exploited to understand and design different structures. In addition, recent studies at MIT produced new graphic tools for the analysis of arches behaviour, based on the evaluation of the equations of equilibrium and compatibility, allowing for interactive parametric modelling [16–18].

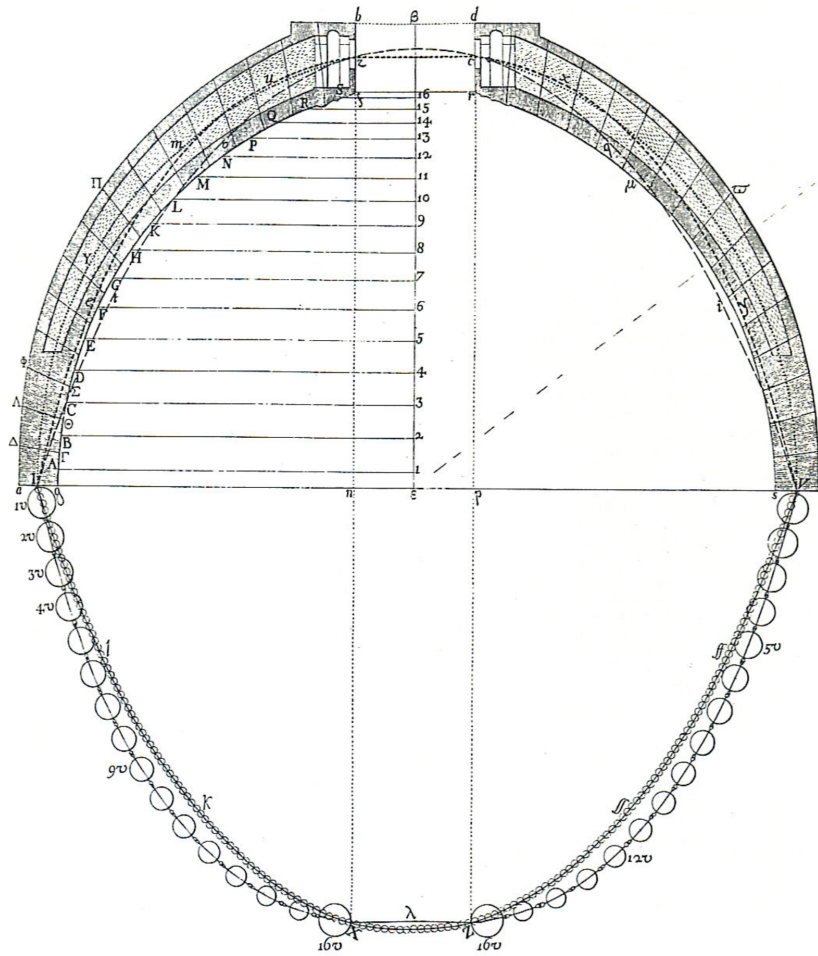


Figure 1.1: Poleni's drawing of his analysis of the Dome of St. Peter's in Rome, [14].



duced the Elastic Analysis [2] to study the stress distribution at the interfaces of arch segments.

In agreement with Navier, Mery's graphical approach, published in 1840 [1], was extensively used in the arches design. However, some hypotheses of elasticity theory encountered critics, as the concepts of homogeneity and isotropy are not compliant with the actual conditions of damaged and cracked materials.

These structural principles for the design of arch bridges geometry are based on the concept of line of thrust, or line of pressure, which is defined as the set of lines of action of the resultant forces acting on a structure, or rather, that act as internal constraint reactions, proceeding from one end to the other end of the structure. According to this definition, if an arch is realized with the exact form of its line of pressure, then it will only be subjected to axial compressive forces because the bending moment vanishes.

This is an ideal condition for structures realized with materials having no tensile strength. However, it cannot easily be obtained, especially because the variable actions on the structure must be considered, changing the position of the line of thrust. Therefore, according to the Elastic Theory, the line of thrust should lie within the central kern of each cross section, to prevent tensile stress with all the possible load conditions. It is the so-called rule of the middle third, which is the central kern in the case of a rectangular cross section. Still, this rule is known to be very conservative for most arches, as highlighted by Accornero *et al.* [23].

The following studies on the masonry arches led to the modern Kinematic Approach or Limit Analysis. One of the most significant revisions concerning the Eighteenth Century theories was formulated by Heyman in 1966 [3]. Referring to Kooharian's studies in 1953 [24], he proposed to apply the Plastic Analysis theorems to solve the issue of the stability of masonry arches in kinematic terms.

Heyman introduced three basic assumptions for such application:

- "Stone has no tensile strength";
- "Stone has infinite compressive strength";

- “The sliding of a stone on another cannot occur” because the friction between masonry blocks is able to avoid sliding failure.

Though, the second assumption on masonry infinite compressive strength is not safe because it does not allow to evaluate the arch failure upon reaching the material compressive strength. According to these hypotheses, the formation of a hinge occurs in the section where the thrust line is tangential to the arch at the edges. Thus, a rigid rotation of the faces of the two adjacent segments takes place around the extreme fibre of the section, as shown by Gilbert and Melbourne [25].

Three tangential points lead to the formation of three hinges; this results in a statically determinate structure. The limit to trigger a kinematic collapse mechanism lies in the development of a fourth hinge [26]. As a result, Limit Analysis consists of the identification of the lowest possible load multiplier that generates a line of thrust that is always contained within the arch volume and tangential to arch edges at four points, as shown in Figure 1.3. The kinematic mechanisms and the load required to cause them, nowadays, can be easily evaluated using software which can rapidly search all possible mechanisms, with reasonings on the rate of change in the potential energy of the system due to virtual rotations [27–29].

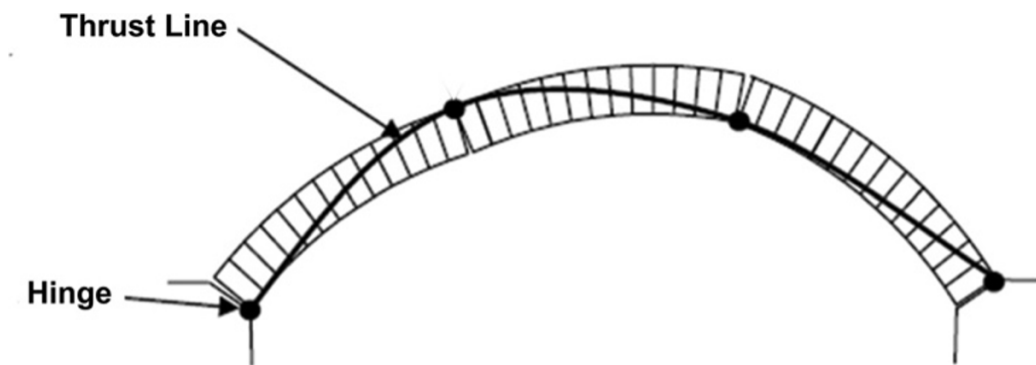


Figure 1.3: Four Hinges arch-collapse mechanism, [4].

More recent studies concern the development of Finite Element Method (FEM) tension models [30, 31], or non-linear FEM in which the non-linearities related to the tensile behaviour arise from the theories of Fracture Mechanics.

Furthermore, studies by Carpinteri *et al.* [6, 23, 32, 33] proposed a method to evaluate masonry arch structure stability based on an incremental analysis of the fracturing process according to Linear Elastic Fracture Mechanics theory.

LEFM can be used to capture the process of damage that can take place in arch structures when the limits of linear Elastic Analysis are overcome, but before reaching the limits established by the Plastic Analysis, enabling to study the arch entire service-life.

It evaluates how the initiating and growth of cracks, with the consequent redistribution of internal stresses, may influence the arch structural behaviour [32]. An elastic-softening law is used [34, 35], corresponding to an elastic law in which the possibility to have a fracturing process is introduced, as shown by Hillerborg *et al.* in 1976 [36]. In addition, it allows evaluating the maximum admissible load on the structure, introducing a “fracturing benefit”, which is the increment in the admissible load given by the LEFM-based approach, if compared to the ones predicted by Elastic Analysis.

Linear Elastic Fracture Mechanics theory is based on the concept of stress intensification. It evaluates the magnitude of stress amplification due to the presence of a sharp crack, which is usually the case of masonry structures. Indeed, in this kind of crack, the amplification of stress at the crack tip tends to be infinite, so it is impossible to assess the behaviour using the concept of stress concentration, which just gives the stress amplification at the tip of a notch.

Whence, structures weakened by internal cracks are evaluated using the stress-intensity factor  $K_I$  to measure the severity of crack opening if a Mode I crack opening is assumed.

The shear effect is neglected, as the line of thrust affects the joint with a slope that is lower than the angle of friction, so there is no mutual sliding. Moreover, compressive stresses reduce the risk of having a Mode II (shear) failure.

The structure reaches collapse when  $K_I = K_{IC}$ , which is the critical value of the stress-intensity factor. For this reason, it is important to extend the evaluation of  $K_I$  for different kind of geometries and load conditions.

In the case of arches, we can study the structure as a curved beam, with a

rectangular cross section, that is rigidly fixed at the abutments. For each cross section, it is possible to evaluate the internal actions, which provide an off-centre compression. Given the cross section properties, also shown in Figure 1.4:

- $h$ : height of the rectangular cross section.
- $t$ : thickness of the rectangular cross section.
- $e$ : eccentricity of the axial force  $F$ .
- $a$ : crack length
- $\xi = a/h$  : crack depth, also called brittle hinge [37] or damage parameter.

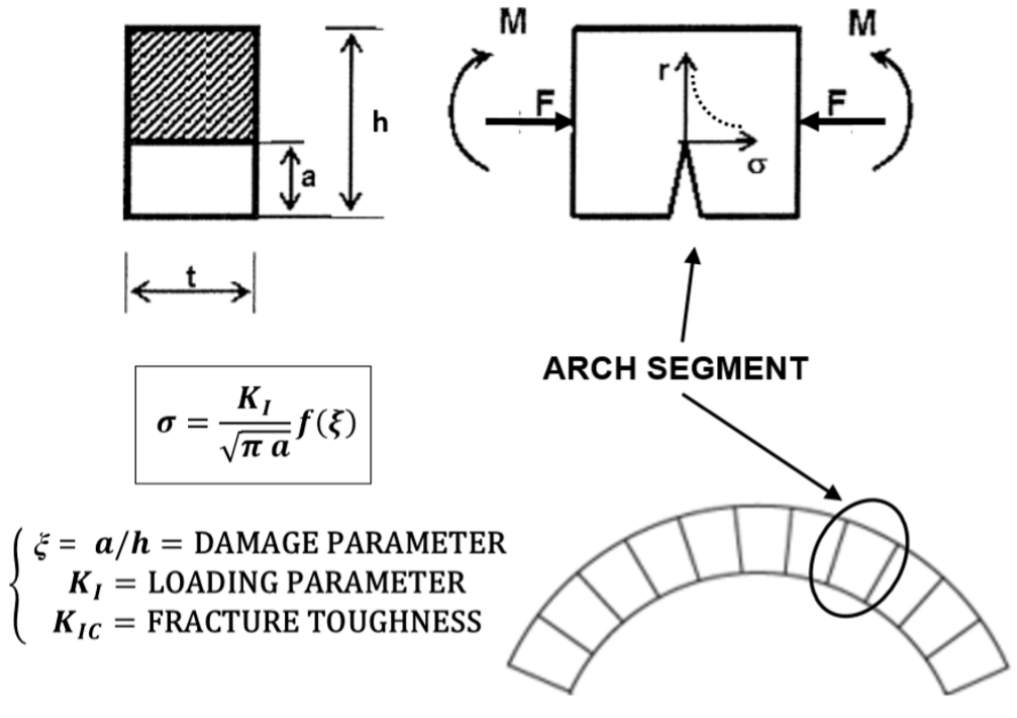


Figure 1.4: Arch segment subjected to off-centre Compression, [33].

The stress intensity factor,  $K_I$ , is evaluated through the superimposition principle as it follows:

$$K_I = K_{IM} - K_{IF} \quad (1.1)$$

In which:

- $K_{\text{IM}}$  is the stress-intensity factor for the bending moment,  $M = Fe$ , which tends to open the crack.
- $K_{\text{IF}}$  is the stress-intensity factor for the compressive axial force,  $F$ , which tends to close the crack.

$$K_{\text{IM}} = \frac{M}{th^{3/2}} Y_{\text{M}}(\xi) \quad (1.2)$$

$$K_{\text{IF}} = \frac{F}{tb^{1/2}} Y_{\text{F}}(\xi) \quad (1.3)$$

Then:

$$K_{\text{I}} = \frac{F}{th^{1/2}} \left[ \frac{e}{h} Y_{\text{M}}(\xi) - Y_{\text{F}}(\xi) \right] \quad (1.4)$$

Where  $Y_{\text{M}}(\xi)$  and  $Y_{\text{F}}(\xi)$  are the shape functions for a relative span length  $0 \leq \xi \leq 0.7$ :

$$Y_{\text{M}}(\xi) = 6 (1.99\xi^{1/2} - 2.47\xi^{3/2} + 12.97\xi^{5/2} - 23.17\xi^{7/2} + 24.80\xi^{9/2}) \quad (1.5)$$

$$Y_{\text{F}}(\xi) = 1.99\xi^{1/2} - 0.41\xi^{3/2} + 18.7\xi^{5/2} - 38.48\xi^{7/2} + 53.86\xi^{9/2} \quad (1.6)$$

The critical condition,  $K_{\text{I}} = K_{\text{IC}}$ , in which the applied axial force is the critical one,  $F_{\text{C}}$ , gives a relationship between the crack depth,  $\xi$ , and the load relative eccentricity,  $e/h$ .

$$\tilde{F}_{\text{C}} = \frac{F_{\text{C}}}{th^{1/2}K_{\text{IC}}} = \frac{1}{\frac{e}{h}Y_{\text{M}}(\xi) - Y_{\text{F}}(\xi)} \quad (1.7)$$

$\tilde{F}_{\text{C}}$  is the non-dimensional critical axial force. It can be used to evaluate the process of cracking with reference to the  $\xi$ , for the different values of  $e/h$  (Figure 1.5). If it has a descending branch, it means that it is not possible to have an increase in the relative crack depth without unloading the system, so it represents an unstable branch. Instead, an ascending branch represents

a stable process of cracking. In the case of arches' cross section, there are initial unstable branches and then stable ones, creating different curves with the variation of the parameter  $e/h$ . So, if the system is in a condition along the unstable curve and the load is not reduced, a catastrophic behaviour with a snap-through instability may occur, leading the system to the nearest point on the curve ( $e/h = \text{constant}$ ) having the same  $\tilde{F}_C$ , with a higher value of  $\xi$ .

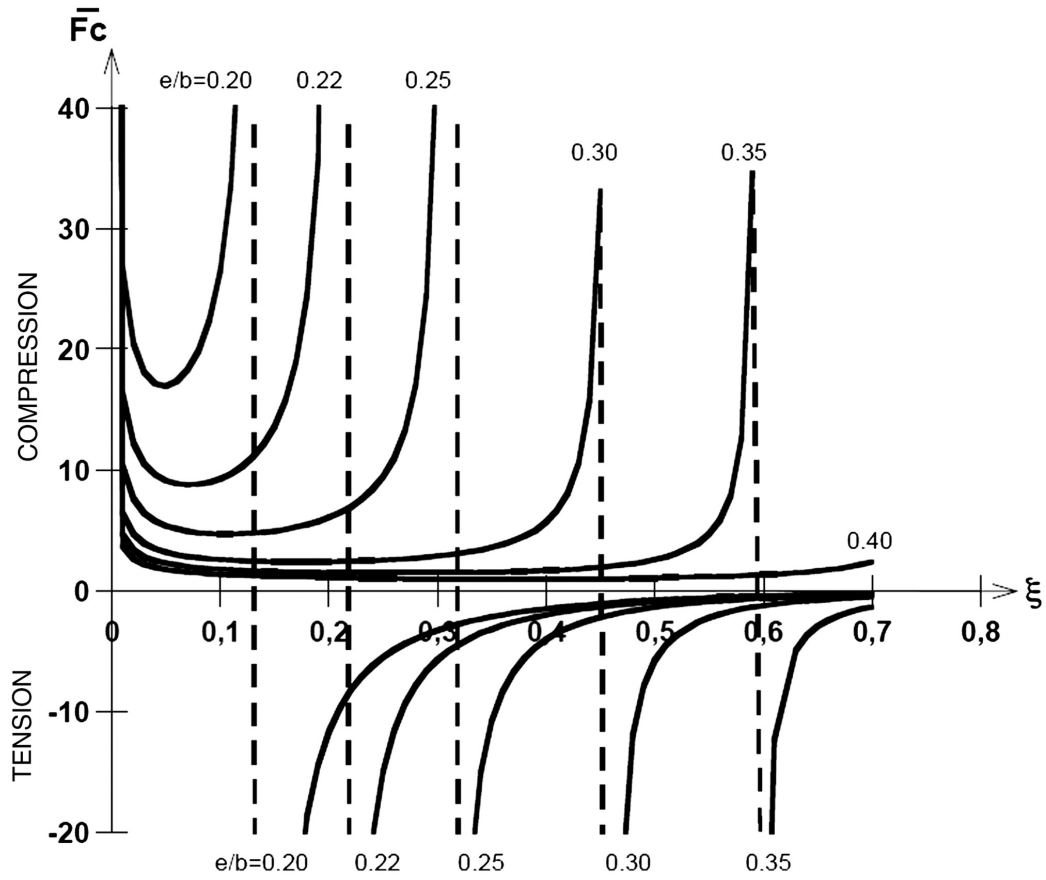


Figure 1.5: Snap-Through Instability for off-centre Compression ( $h=b$ ), [6].

It can be noted that for each value of  $\xi$ , there exists a relative load eccentricity,  $e/h$ , below which the crack tends to close again [6]. The limit condition to have a closing effect is given by:

$$K_I = \frac{F}{th^{1/2}} \left[ \frac{e}{h} Y_M(\xi) - Y_F(\xi) \right] = 0 \quad (1.8)$$

Which leads to:

$$\frac{e}{h} = \frac{Y_F(\xi)}{Y_M(\xi)} \quad (1.9)$$

If  $K_I \leq 0$ , with a fixed value of  $e/h$ , the crack reduces its depth, at list partially, from an initial value of  $\xi$ , to  $\xi^*$ , as shown in Figure 1.6.

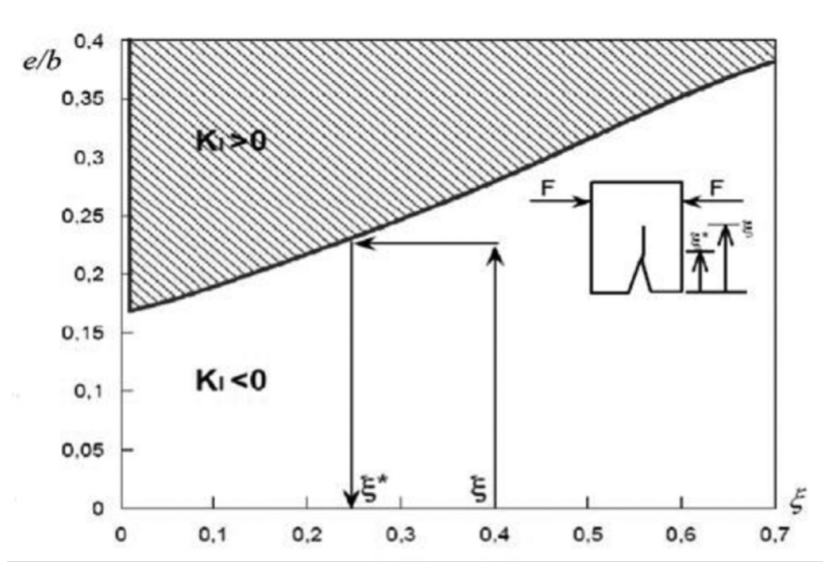


Figure 1.6: Crack closure curve, [6].

Moreover, it is interesting to consider the scale effects that arise due to the different dimensions of  $K_{IC}$  and the ultimate strength,  $\sigma_u$ .

From:

$$K_{IC} = \frac{F_C}{th^{1/2}} \left[ \frac{e}{h} Y_M(\xi) - Y_F(\xi) \right] \quad (1.10)$$

It is possible to divide both members by the product  $\sigma_u h^{1/2}$ :

$$\frac{K_{IC}}{\sigma_u h^{1/2}} = \frac{F_C}{\sigma_u t h} \left[ \frac{e}{h} Y_M(\xi) - Y_F(\xi) \right] \quad (1.11)$$

In the previous equation we can identify the brittle number:

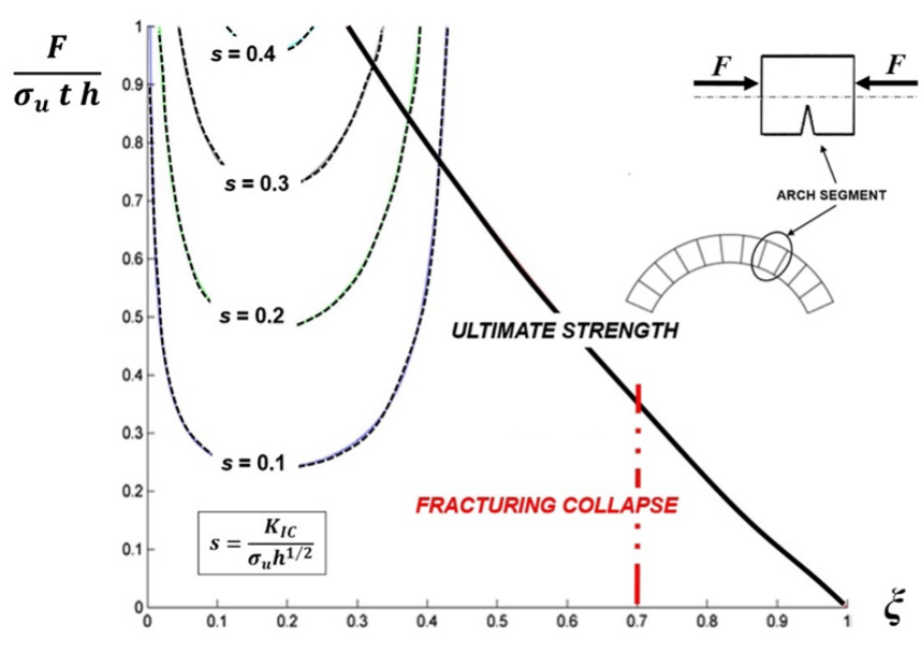
$$s = \frac{K_{IC}}{\sigma_u h^{1/2}} \quad (1.12)$$

Consequently, the normalised axial load is given by the following equation:

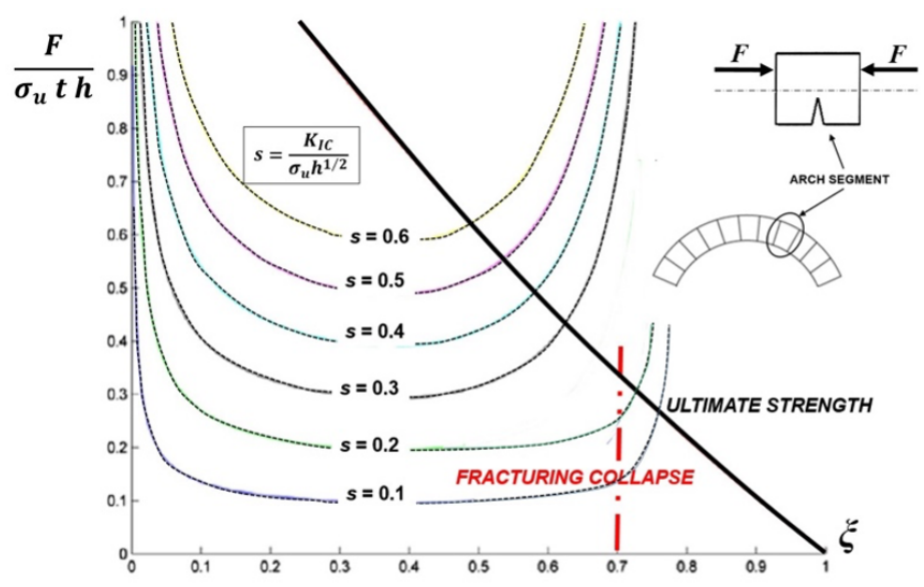
$$\frac{F_C}{\sigma_u t h} = \frac{s}{\left[ \frac{e}{h} Y_M(\xi) - Y_F(\xi) \right]} \quad (1.13)$$

Different curves representing the critical axial load with the variation of  $\xi$  may be evaluated, due to the variation of the brittle number or the relative eccentricity, as in Figure 1.7.

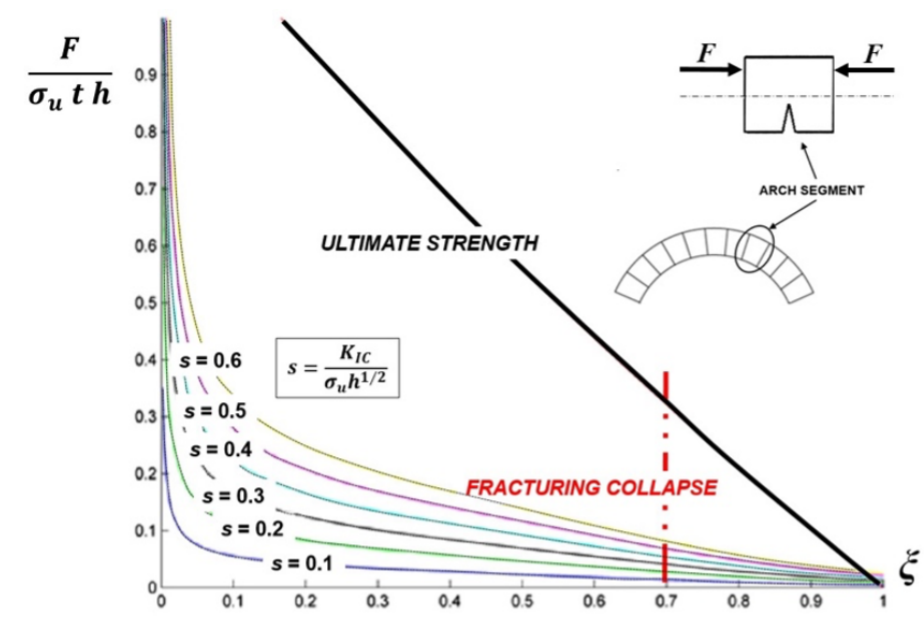
They can be compared with the curve representing the condition in which the structure reaches the ultimate strength. Then, as the structure reaches the collapse due to crack propagation only if  $\xi \geq 0.7$  (70% of the cross section is damaged) [6, 38], it occurs if, at  $\xi \geq 0.7$ , the fracturing process occurs before the reaching of ultimate strength.



(a)



(b)



(c)

Figure 1.7: Scale effects in masonry arch structures: Dimensionless load of brittle crack propagation versus normalised crack depth,  $\xi$ , for  $e/h = 0.15$  (a);  $e/h = 0.20$  (b);  $e/h = 0.35$  (c), [33].

The whole masonry arch, finally, can be analysed through a Finite Element framework, subdividing the arch into beam elements, considering the applied loads and the elements stiffness.

If the elements are uncracked, they behave as perfectly fixed joints, instead, if they are cracked, they carry the internal actions as elastically fixed joints [23, 34], with a stiffness that may be evaluated through an energy balance between the elastic work and the fractured one. Therefore, the cracked elements stiffness matrix is modified into the algorithm, exclusively by the four rotational terms [6, 39–43].

The rotational stiffness of an elastically fixed joint is:

$$W = \frac{h^2 t E}{2 \int_0^\xi Y_M^2(\xi) d\xi} \quad (1.14)$$

Applying the principle of virtual work to a beam with an elastic hinge to simulate the crack at the midspan, the stiffness matrix is given in (1.15) :

$$\begin{bmatrix} \frac{EA}{l} & 0 & 0 & -\frac{EA}{l} & 0 & 0 \\ 0 & \frac{12EI}{l^3} & -\frac{6EI}{l^2} & 0 & -\frac{12EI}{l^3} & -\frac{6EI}{l^2} \\ 0 & -\frac{6EI}{l^2} & \frac{EI(3EI+4IW)}{l(EI+lW)} & 0 & \frac{6EI}{l^2} & \frac{EI(3EI+2IW)}{l(EI+lW)} \\ -\frac{EA}{l} & 0 & 0 & \frac{EA}{l} & 0 & 0 \\ 0 & -\frac{12EI}{l^3} & \frac{6EI}{l^2} & 0 & \frac{12EI}{l^3} & \frac{6EI}{l^2} \\ 0 & -\frac{6EI}{l^2} & \frac{EI(3EI+2IW)}{l(EI+lW)} & 0 & \frac{6EI}{l^2} & \frac{EI(3EI+4IW)}{l(EI+lW)} \end{bmatrix} \quad (1.15)$$

Where E is the Young's modulus of the material, A and I are the area and the moment of inertia of the cross section, and l is the length of the beam finite element.

It can be noted that, if W tends to infinity, the four rotational terms in the matrix return to the standard values of the uncracked beam finite element. The LEFM-based approach is implemented following a step-by-step procedure, increasing progressively the applied load. For each step the routine gives the load increment, but also the axial force applied on each segment with its own eccentricity. Therefore, it is possible to update the crack depth  $\xi$  and the stiffness properties [6, 23, 32].

If the updated  $\xi$  is the same as the previously determined one, the process

stabilizes.

If the updated  $\xi$  is lower than the previously determined one, there is a closure effect, which identifies the maximum admissible crack depth.

Instead, if  $\xi$  grows within the load increments and reaches 0.7, the segment becomes inefficient, giving a fracturing collapse.

The routine also monitors another parameter that is related to the maximum compressive stress, because when the ultimate compressive strength is reached, then a crushing collapse may occur.

The previously explained method has been applied to some case studies, to compare the results with the ones given by the Elasticity Theory or the Limit Analysis, and to evaluate the so-called “fracturing benefit”.

Among these case studies we have the Porta Napoli multi-span Bridge, located in Taranto, Italy [44]; the Mosca Bridge and the Vittorio Emanuele I Bridge, located in Turin, Italy; the Limyra Bridge, a late Roman monumental arch bridge located in West Turkey; three masonry arch bridges are located in the Lanzo Valleys (Italy): Forno di Lemie Bridge, Fucine di Viù Bridge, and the Devil’s Bridge, Ponte del Roch [23].

## Chapter 2

# Nonlinear fracture mechanics

Linear Elastic Fracture mechanics assumes that the stress field is amplified and tends to infinity at the crack tip in an infinitesimal area. However, in real materials, there is a greater damaged area with finite dimensions, which is ahead of the crack tip, and the stress field is finite [45].

The non-damaged area can be evaluated through a linear behaviour, while in the damaged area, also known as the process zone, there is a diffused dissipation of energy. Indeed, the theory of LEFM correctly represents only the cases in which this process zone is microscopic.

From the characteristics and the behaviour of the process zone, it is possible to study the most suitable nonlinear model. If damage is distributed uniformly in the process zone, the *Diffused Damage Crack Model* can be used. If the mechanical damage is confined along the crack and there is still an interaction between the two sides of the crack, the *Cohesive Crack Model* can be introduced. It enables an evaluation of the effect of interlocking that may occur between the grains through an equivalent closing stress field which is evaluated as a function of the crack mouth opening displacement,  $w^t$  (CMOD).

The *Bridged Crack Model* is suggested when the crack is subjected to a bridging effect because of the presence of reinforcement. In this case, the fibres of reinforcement introduce a closing force, and the crack opening continues locally between two adjacent fibres. It has been exploited for under-reinforced concrete beams and fibre reinforced elements [46, 47]. In addition,

the *Microcrack-Interacting Model* is used to represent elements in which the process zone, ahead of the crack tip, is subjected to a cloud of micro-cracks. The following section presents the Cohesive Crack Model in further detail.

## 2.1 The cohesive crack model

The Cohesive Crack Model can be used to describe the response of materials with a strain-softening behaviour. Therefore, it is helpful to understand the behaviour of plain concrete or masonry structures, in which an interlocking effect may introduce closing actions on the crack. It has been firstly proposed by Hillerborg *et al.* in 1976 [36]. The Cohesive Crack model is similar to Dugdale's model [48]. Dugdale simulates the plastic area through a uniform distribution of stress directly applied to the sides of a fictitious crack, which is longer than the real crack, as shown in Figure 2.1.

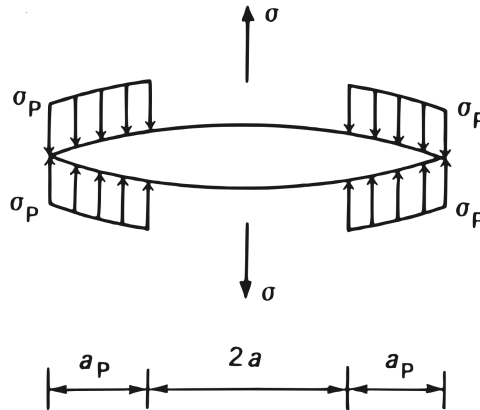


Figure 2.1: Representation of the plastic zone on a crack according to Dugdale model [48] , from Carpinteri, *Advanced Structural Mechanics*, [49].

The length of the fictitious crack is identified by imposing that the total stress-intensity factor is equal to zero:

$$K_I(\sigma) + K_I(\sigma_p) = 0 \quad (2.1)$$

In which, the first term is related to the applied stress, while the second term is related to the restraining effect due to the  $\sigma_p$  on the fictitious crack. The

main difference is that in the Cohesive Crack Model, the distribution of the cohesive forces is not uniform but decreases as the crack opening increases, following a softening law.

It is analysed with the introduction of a strength failure criterion to describe the initiation of the cracking process when a point reaches the ultimate tensile stress. From this condition, the fracture area grows. The process zone is modelled as an extension of the real crack, or a fictitious crack, in which closing stresses arise, with a  $\sigma - w^t$  law [50, 51]. A mode I failure is analysed (Figure 2.2).

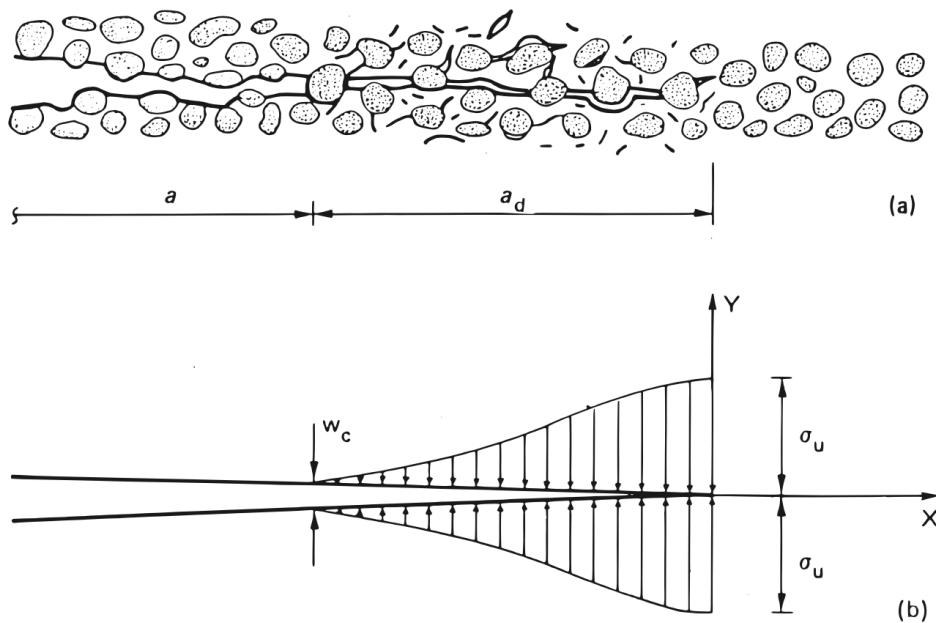


Figure 2.2: Developing of the macrocrack, still partially sutured by inclusions, aggregates, or fibres (a);  $\sigma - w$  law (b), from Carpinteri, Advanced Structural Mechanics, [49].

The point of the crack in which the stress drops to zero and the crack opening reaches the critical width  $w_{cr}^t$  is defined as the real crack tip. The point between the process zone and the undamaged material is defined as the fictitious crack tip. In this model, shear stress on the crack faces is neglected. In the non-damaged material, a linear constitutive law can be introduced,

until the ultimate stress and strain,  $(\sigma_t, \epsilon_t)$ , are reached. In the process area, for the sake of simplicity, the stress field can be studied as linear, with the maximum value,  $\sigma_t$ , at the fictitious crack tip, and a stress-free condition at the real crack tip, as shown in Figure 2.3.

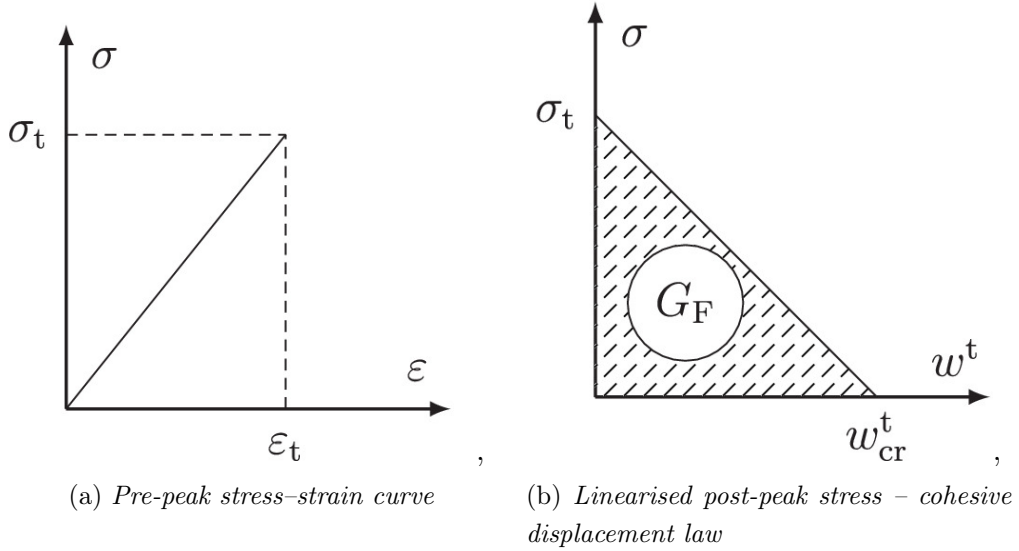


Figure 2.3: Simplified Cohesive Crack Model relationship, [52].

The area below the curve represents the fracture energy,  $G_F$ . The constitutive law is therefore represented by the following equation:

$$\begin{cases} \sigma = E\epsilon & \epsilon \leq \epsilon_t \\ \sigma = \sigma_t \left(1 - \frac{w^t}{w_{cr}^t}\right) & w \leq w_{cr}^t \\ \sigma = 0 & w \geq w_{cr}^t \end{cases} \quad (2.2)$$

Consequently, it is possible to evaluate the displacement,  $\delta$ , at the top of a specimen, fixed at the base with length  $\ell$  and width  $b$  subjected to tensile forces, as shown in Figure 2.4.

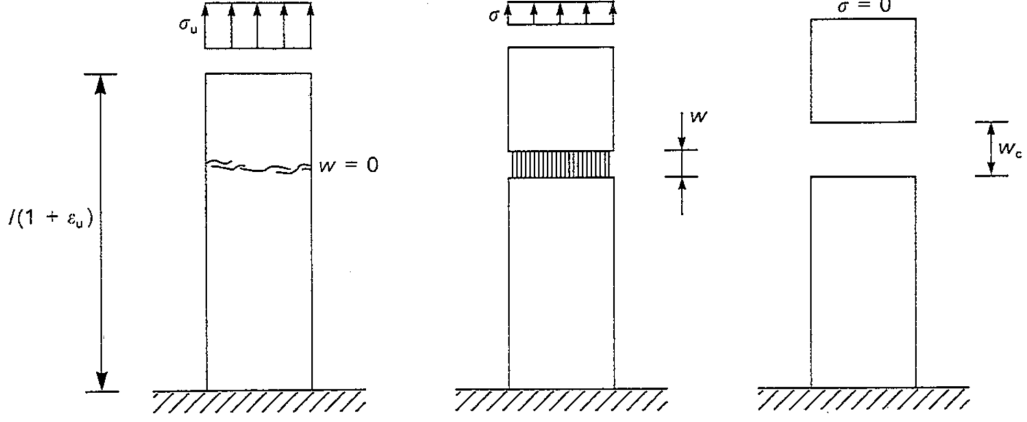


Figure 2.4: Loading process of a specimen, fixed at the base and subjected to tensile stress, [53].

In the first step:

$$\delta = \frac{\sigma}{E} \ell \quad \epsilon \leq \epsilon_t \quad (2.3)$$

When  $\epsilon$  reaches the ultimate value in the Elastic field, there is the initiation of a crack and the development of the cohesive area.

Consequently, the displacement is given by:

$$\delta = \frac{\sigma}{E} \ell + w^t \quad w \leq w_{cr}^t \quad (2.4)$$

Introducing the Eqn.(2.2) into the Eqn.(2.3), if  $w \leq w_{cr}^t$ :

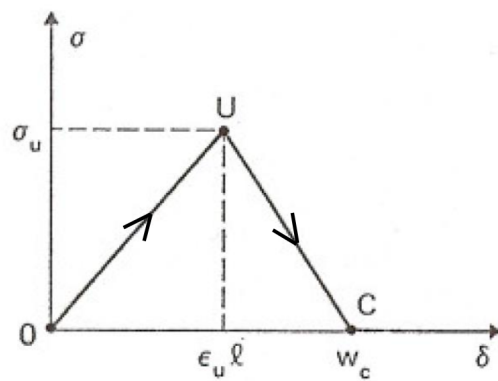
$$\begin{aligned} \delta &= \frac{\sigma}{E} \ell + w_{cr}^t \left( 1 - \frac{\sigma}{\sigma_t} \right) \\ &= \sigma \left( \frac{\ell}{E} - \frac{w_{cr}^t}{\sigma_t} \right) + w_{cr}^t \end{aligned} \quad (2.5)$$

It represents a straight line and the behaviour is evaluated according to its slope:

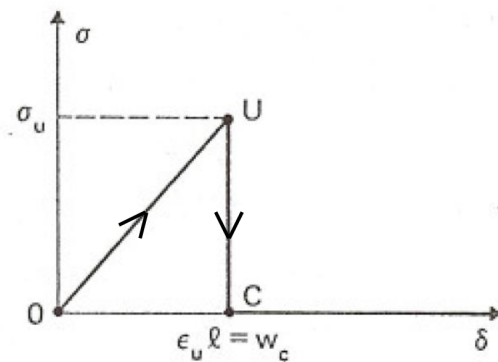
$$\frac{d\delta}{d\sigma} = \left( \frac{\ell}{E} - \frac{w_{cr}^t}{\sigma_t} \right) \quad (2.6)$$

- If  $w_{cr}^t > \frac{\sigma_t \ell}{E}$ , the slope is negative. The behaviour consists in a softening branch which is stable if loading is displacement controlled, (Figure 2.5a).

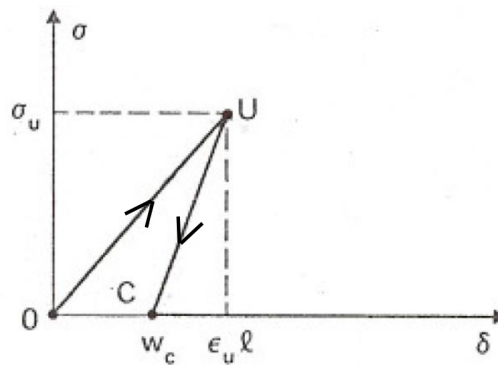
- If  $w_{\text{cr}}^t = \frac{\sigma_t \ell}{E}$ , there is a vertical drop, even with a displacement-controlled analysis, (Figure 2.5b).
- If  $w_{\text{cr}}^t < \frac{\sigma_t \ell}{E}$ , the slope is positive, with a reduction in both stress and displacement. A catastrophic softening, or snap-back behaviour, occurs, (Figure 2.5c).



(a) *Strain softening behaviour*



(b) *Catastrophic softening*



(c) *Catastrophic softening with snap-back*

Figure 2.5: Post peak stress-displacement response, [54].

The snap-back behaviour is due to brittle fracturing of the concrete or masonry. In the analysis of a cracked beam, it can be evaluated by controlling

the crack mouth opening displacement instead of the beam deflection [54]. The condition giving snap-back instability can be rewritten as it follows:

$$\frac{w_{\text{cr}}^t/2b}{\epsilon_t \ell/b} < \frac{1}{2} \quad (2.7)$$

With the assumption of a linear stress-displacement field in the process zone  $G_{\text{F}}$  is given by:

$$G_{\text{F}} = \frac{1}{2} \sigma_t w_{\text{cr}}^t \quad (2.8)$$

It follows:

$$\frac{w_{\text{cr}}^t}{2b} = \frac{G_{\text{F}}}{\sigma_t b} = s_{\text{E}} \quad (2.9)$$

Where,  $s_{\text{E}}$  is the energy brittleness number.

Introducing also the slenderness ratio of the element  $\lambda = \ell/b$ , the condition to have a snap-back becomes:

$$\frac{s_{\text{E}}}{\epsilon_t \lambda} \leq \frac{1}{2} \quad (2.10)$$

It highlights that the mechanical behaviour of the element has a size-scale dependency. In detail, if the slenderness  $\lambda$  and the scale of the element are relatively high and the fracture energy  $G_{\text{F}}$  is low, there is the tendency toward a brittle behaviour [54].

## 2.2 Carpinteri algorithm

The post-peak behaviour is analysed through a numerical procedure proposed by Carpinteri [9–11]. It is based on a Finite Element Method (FEM) approach, and it has been applied mainly on concrete beams.

The algorithm simulates the fracture process by evaluating the development of a crack opening. Each step of the analysis is governed by the crack mouth opening displacement (CMOD) to study the growth of the fictitious crack and to be able to assess an eventual snap-back instability.

Therefore, at each step, the loading on the element is an additional unknown value, which is evaluated, together with the displacement, with an iterative

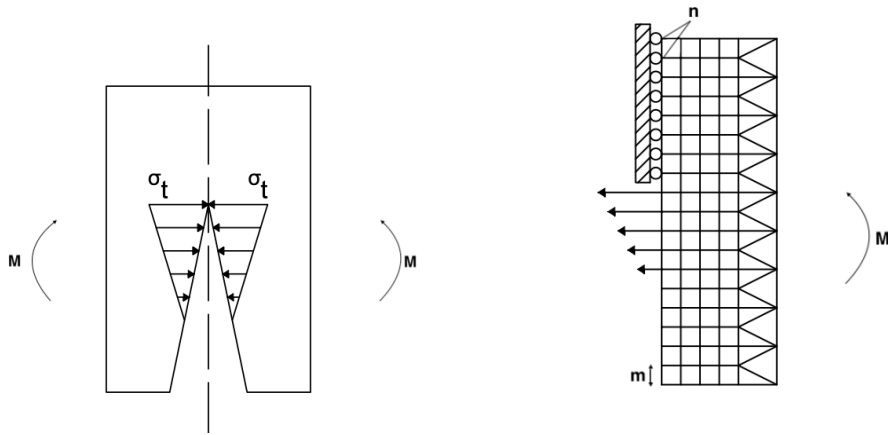
process. The analysed setup is that of a three-point bending test, with the following characteristics:

- $\ell$ : length of the beam;
- $t, b$ : dimensions of the beam cross section;
- $\delta$ : midspan deflection.

The midspan cross section is modelled through  $n$  nodes, and the distance between two nodes,  $m$ , as shown in Figure 2.6.

These parameters have to satisfy the following condition to avoid numerical issues:

$$m \leq 600w_{cr}^t \quad (2.11)$$



(a) *Stress distribution across the cohesive zone*      (b) *Equivalent nodal forces in the FEM discretization*

Figure 2.6: Potential fracture line: physical and numerical schemes, from Carpinteri algorithm, [10].

Given the main assumptions [55]:

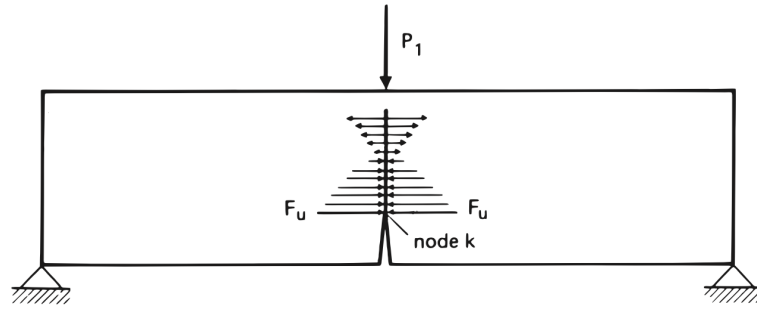
1. The cohesive fracture zone (process zone) begins to develop when the maximum principal stress achieves the ultimate tensile strength  $\sigma_t$ .
2. The material in the process zone is partially damaged but is still able to transfer stress. Such a stress is dependent on the CMOD  $w^t$ .

The crack opening process is governed by:

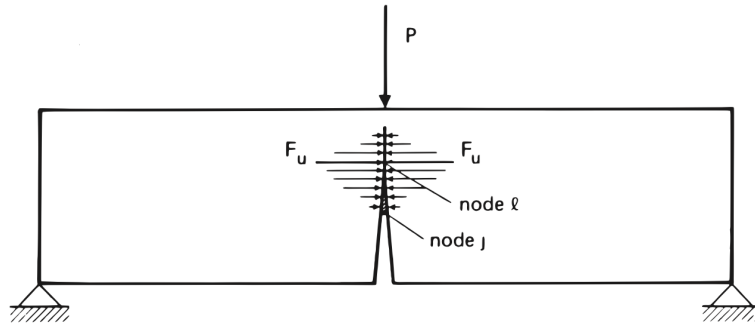
$$\{w\} = [K]\{F\} + \{C\}P + \{\Gamma\} \quad (2.12)$$

In which:

- $\{w\}$ : vector of nodal crack opening displacement;
- $[K]$ : matrix of coefficients of influence, with nodal displacements for unit applied nodal force  $\{F\}$ ;
- $\{F\}$ : vector of nodal forces;
- $\{C\}$ : vector of coefficients of influence, with crack displacements for unit external load  $P$ ;
- $P$ : external load at the midspan of the beam;
- $\{\Gamma\}$ : vector of crack opening due to the specimen weight.



(a) *Initial phase, without process zone*



(b) *Intermediate phase, with the cohesive process zone*

Figure 2.7: Three Point Bending Test with Carpinteri algorithm, [55].

In the first phase, the process zone is absent ( Figure 2.7a). From node 1 to node  $k$ , there is the initial crack. In node  $k$   $w^t = 0$  and the ultimate force is reached. Therefore, the system is governed by  $(2n)$  equations with the unknowns  $\{w\}$  and  $\{F\}$ :

$$F_i = 0, \quad i = 1, 2, \dots, (k - 1) \quad (2.13a)$$

$$w_i = 0, \quad i = k, \dots, n \quad (2.13b)$$

In the second phase, with the presence of the fictitious crack ( Figure 2.7b), a system of  $(2n + 1)$  equations is needed due to the presence of the additional

variable  $P$ .

$$F_i = 0, \quad i = 1, 2, \dots, (j - 1) \quad (2.14a)$$

$$F_i = F_u \left( 1 - \frac{w_i^t}{w_{cr}^t} \right), \quad i = j, \dots, l \quad (2.14b)$$

$$w_i^t = 0, \quad i = 1, \dots, n \quad (2.14c)$$

The beam deflection  $\delta$  is evaluated from:

$$\delta = \{C\}^T \{F\} + D_P P + D_\gamma \quad (2.15)$$

Where  $D_P$  is the deflection for  $P = 1$ , and  $D_\gamma$  is the displacement generated by the weight of the specimen.

In the steps with the cohesive zone between two nodes,  $k$  and  $(k + 1)$ , the external load is computed so that the ultimate nodal force is applied at node  $(k + 1)$ . The fictitious crack is then incremented by one finite element, and the deflection is evaluated. When the fictitious crack tip reaches node  $n$ , the routine ends.

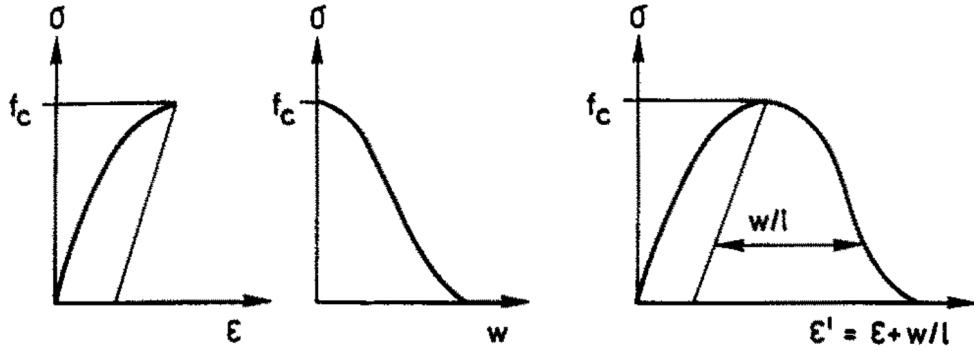
## Chapter 3

# The crushing issue and the overlapping crack model

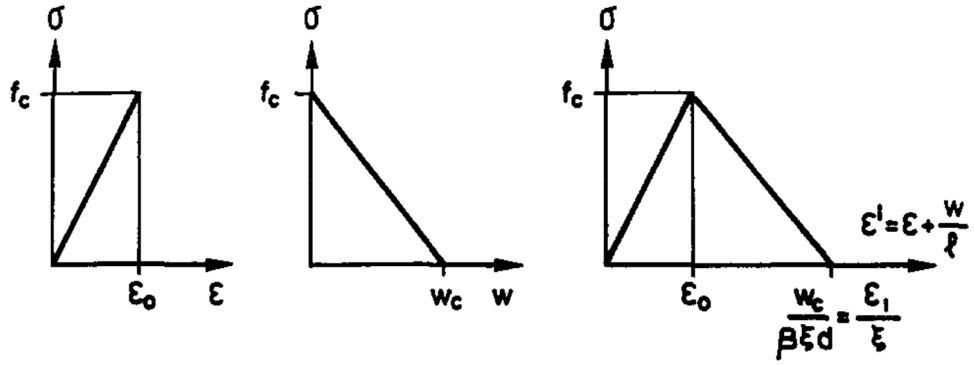
The *Cohesive Crack Model* is used to model the opening and development of cracks in quasi-brittle structural elements that are subjected to tensile forces. Though, it does not allow to assess the problems related to the crushing failure that may occur due to compressive forces.

The commonly used constitutive laws for concrete in compression are the elastic-perfectly plastic one, the parabolic-perfectly plastic one and Sargin's parabola, but they do not consider size dependency of the response. However, the compressive behaviour of this typology of materials, especially concrete, has been deeply studied. In particular, Hillerborg [56] introduced a model based on the concepts of strain softening and localisation in the compressed area. In addition, different theoretical models and laboratory tests analysed the post-peak compression behaviour and confirmed the presence of size-effects [57–61]. Consequently, the *Overlapping Crack model* has been proposed by Carpinteri *et al.* [7, 62, 63].

Hillerborg's model concerns the evaluation of moment and rotational capacity of concrete beams, taking into account the material compressive failure. If concrete is subjected to uniaxial compression, in the post-peak phase, it can be subjected to microcracks development and fragmentation. Therefore, the assumptions related to the commonly used constitutive laws and the hy-



(a) Complete relationship



(b) Simplified relationship

Figure 3.1: Compressive stress-strain relationship, with an ascending stress-strain curve and a descending stress-deformation curve, [56].

pothesis of the cross section planarity in the deformed configuration are not sufficiently accurate. However, Hillerborg tried to develop a simplified numerical model to represent the localisation of stresses and the size-dependency of the behaviour with the assumption that plane sections remain plane and linear stress-strain relationships can be used.

In the initial linear elastic brach, concrete reaches  $(\epsilon_0, \sigma_c)$ . In the second brach, a softening law  $(\sigma - w^c)$  is assumed as shown in Figure 3.1. The strain localisation is introduced to evaluate the energy dissipation in the localisation length  $\ell$ , which is a function of the depth of the neutral axis  $\xi d$ :

$$\ell = \beta \xi d \quad (3.1)$$

In which,  $\beta$  is evaluated from experimental tests, or it is assumed equal to 0.8. Following these assumptions, Hillerborg evaluated the beam's moment-curvature diagrams realising a first attempt to introduce fracture mechanics concepts for compressed concrete.

### 3.1 The overlapping crack model

The *Overlapping Crack Model* is able to simulate the behaviour and the damage process of concrete and generic quasi-brittle materials when they are subjected to compressive actions. The compressive damage is also known as *crushing*. Its evaluation is complex because it depends on the friction between concrete surfaces and loading surfaces, and also on the specimen slenderness and size [59, 64]. The crushing zone is described by a fictitious interpenetration of the material, while the other part of the cross section remains in elastic field [65]. Consequently, in analogy with the Cohesive Crack Model, it is necessary to introduce a first  $\sigma - \epsilon$  relationship, until the compression strength,  $\sigma_c$ , is achieved (Figure 3.2a), and a  $\sigma - w^c$  relationship to describe concrete crushing (Figure 3.2b), in which  $w^c$  is the fictitious overlapping displacement, until the critical value  $w_{cr}^c$  is reached. The area below the  $\sigma - w^c$  curve represents the crushing energy,  $G_C$ , which is a material property.

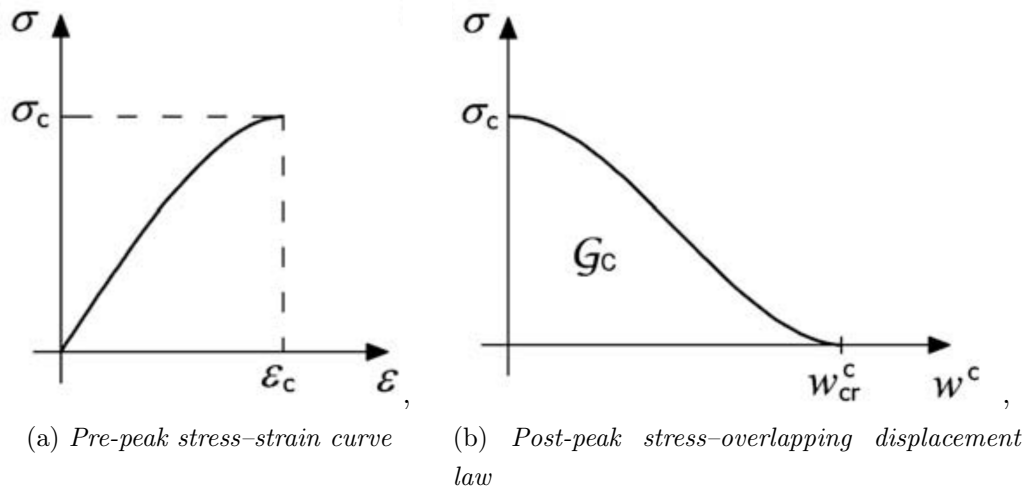


Figure 3.2: Overlapping Crack Model relationship, [7].

According to this model, the crushing zone grows perpendicular to the second principal stress, and it is subdivided into two parts. Similarly to the Cohesive Crack Model, there is the part in which the fictitious overlapping displacement is lower than the critical value  $w_{cr}^c$ , where the element is damaged, but it is still able to transfer stresses, while the other part, where  $w^c \geq w_{cr}^c$ , is a stress-free area.

In the experimental tests, for the evaluation of  $w^c$ , the  $\sigma - \delta$  relationship is considered. The value of  $w^c$  is given by the whole displacement reduced of the elastic displacement  $\delta_{el}$ , caused by the reduction of the applied stress in the post-peak regime, and the pre-peak plastic deformation,  $\delta_{pl}$ , as shown in Figure 3.3.

$$\delta_{el} = \frac{\sigma}{E_{ci}} \ell \quad (3.2)$$

Where,  $\ell$  is the length of the specimen and  $E_{ci}$  is the tangent elastic modulus.

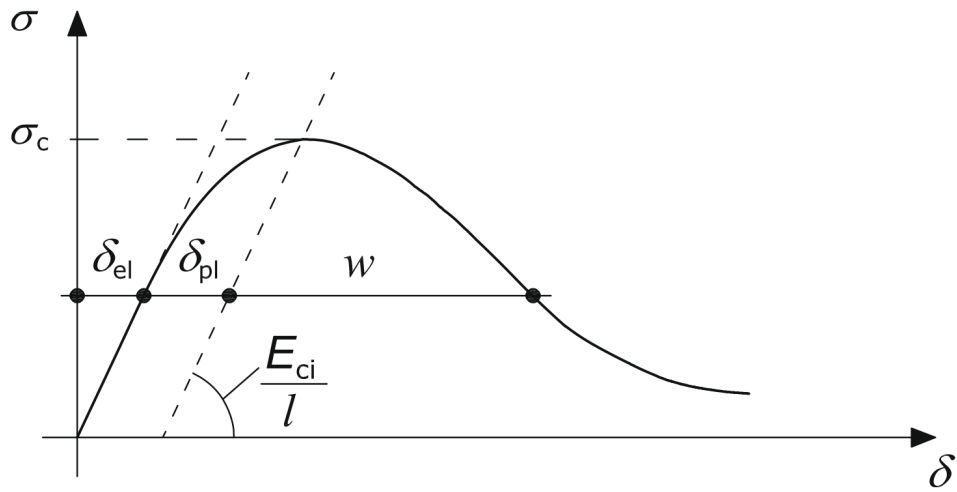


Figure 3.3: Estimation of the localised interpenetration,  $w^c$ , from the total shortening of the specimen,  $\delta$ , [65].

For the numerical analysis, it is possible to simplify the constitutive laws adopting a linearised overlapping law, as shown in Figure 3.4.

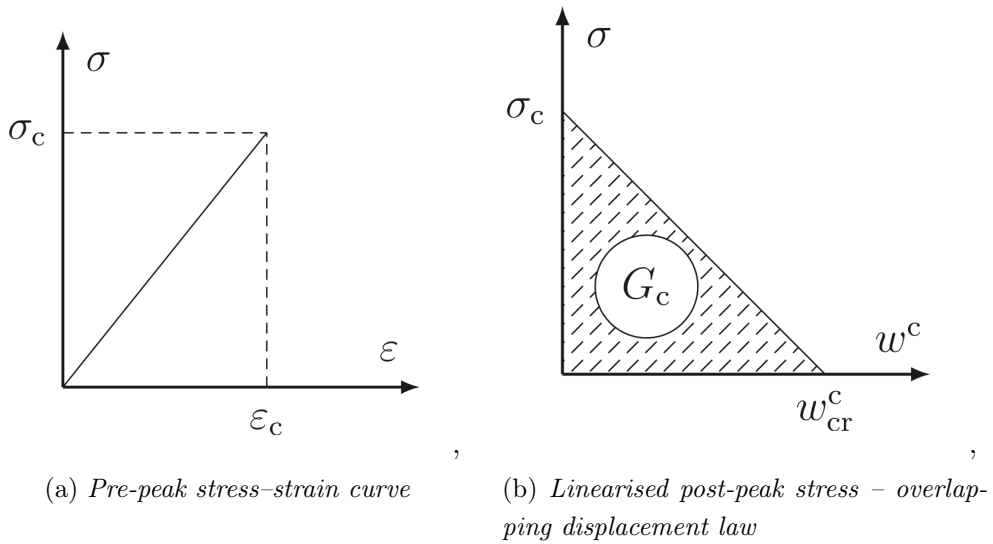


Figure 3.4: Simplified Overlapping Crack Model relationship, [52].

The constitutive law is therefore represented by the following equation:

$$\begin{cases} \sigma = E\epsilon & \epsilon \leq \epsilon_c \\ \sigma = \sigma_c \left(1 - \frac{w^c}{w_{cr}^c}\right) & w^c \leq w_{cr}^c \\ \sigma = 0 & w^c \geq w_{cr}^c \end{cases} \quad (3.3)$$

### 3.2 Uniaxial compression test

The Overlapping Crack Model can be used to evaluate the response of a specimen subjected to uniaxial compression, having a length equal to  $\ell$  and width  $b$ . Firstly, the specimen behaves according to the elastic constitutive

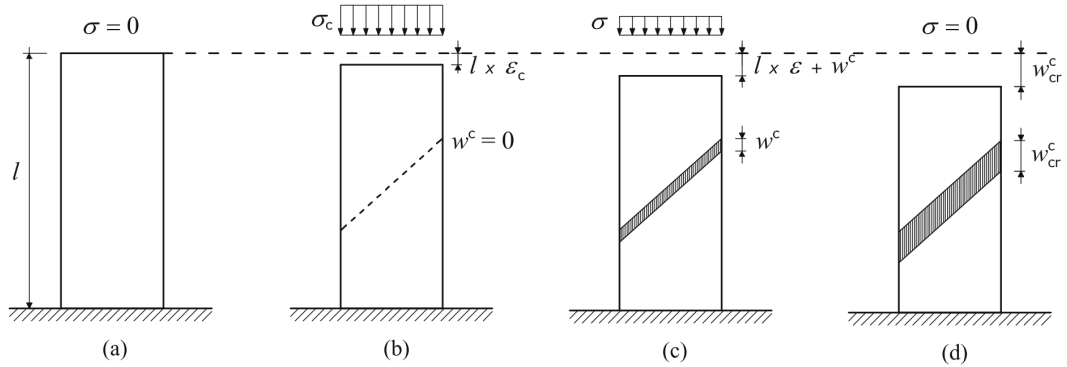


Figure 3.5: The loading process of a uniaxial compression test, [65].

law, without any damage (Figure 3.5a). The displacement,  $\delta$ , is given by:

$$\delta = \epsilon \ell = \frac{\sigma}{E} \ell \quad \epsilon \leq \epsilon_c \quad (3.4)$$

When the ultimate elastic condition is reached (Figure 3.5b), damage starts to localise on a sloped crushing band. Instead, in the non-damaged area, the behaviour is still elastic. In this phase, the displacement is incremented by the value of interpenetration,  $w^c$ , (Figure 3.5c).

$$\delta = \frac{\sigma}{E} \ell + w^c \quad w^c \leq w_{cr}^c \quad (3.5)$$

Introducing (3.3) in (3.5):

$$\delta = \frac{\sigma}{E}\ell + w_{\text{cr}}^c \left(1 - \frac{\sigma}{\sigma_c}\right) \quad w^c \leq w_{\text{cr}}^c \quad (3.6)$$

In the third phase (Figure 3.5d),  $w_{\text{cr}}^c$  is reached. Therefore, the material is completely damage and it is not able to transfer stress ( $\sigma = 0$ ). From the rearrangement of 3.6, it is possible to represent a straight line, and the behaviour is evaluated according to its slope.

$$\delta = w_{\text{cr}}^c + \sigma \left( \frac{\ell}{E} - \frac{w_{\text{cr}}^c}{\sigma_c} \right) \quad (3.7)$$

The slope is given by:

$$\frac{d\delta}{d\sigma} = \left( \frac{\ell}{E} - \frac{w_{\text{cr}}^c}{\sigma_c} \right) \quad (3.8)$$

If the slope is negative, the behaviour consists of a softening branch which is stable if loading is displacement controlled (Figure 3.6a).

$$\left( \frac{\ell}{E} - \frac{w_{\text{cr}}^c}{\sigma_c} \right) < 0 \quad (3.9)$$

If  $\frac{d\delta}{d\sigma}$  is equal to zero a vertical drop occurs (Figure 3.6b).

If  $\frac{d\delta}{d\sigma}$  is positive, a snap-back behaviour occurs (Figure 3.6c).

$$\left( \frac{\ell}{E} - \frac{w_{\text{cr}}^c}{\sigma_c} \right) > 0 \quad (3.10)$$

The Eqn.(3.10) can be rewritten as it follows:

$$\frac{w_{\text{cr}}^c/2b}{\epsilon_c \lambda} \leq \frac{1}{2} \quad (3.11)$$

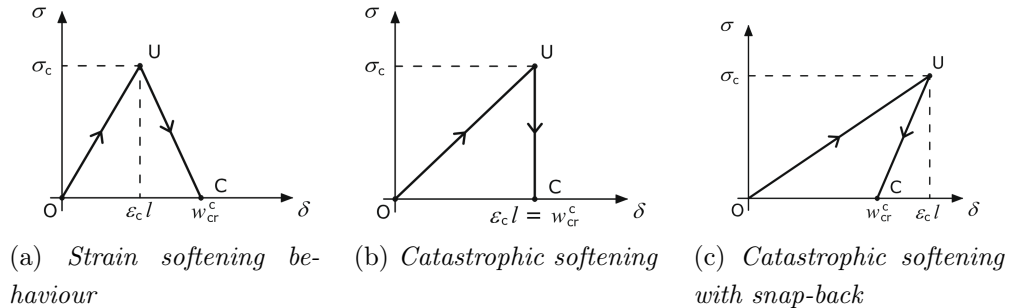


Figure 3.6: Stress-displacement response in compression, [62].

In analogy with the Cohesive Model, Eqn.(2.9), it is possible to introduce the *energy brittleness number in compression*,  $s_E^c$ .

$$s_E^c = \frac{w_{cr}^c}{2b} = \frac{G_C}{\sigma_c b} \quad (3.12)$$

Where,  $G_C = \frac{1}{2}\sigma_c w_{cr}^c$ .

Consequently, the condition to get the snap-back becomes:

$$\frac{s_E^c}{\epsilon_c \lambda} \leq \frac{1}{2} \quad (3.13)$$

## Chapter 4

# The cohesive/overlapping crack model

The *Cohesive/Overlapping Crack Model* and the related algorithm has been proposed by Carpinteri *et al.* [7, 62, 63] as a further development of the cohesive algorithm to introduce the compressive failure in the numerical procedure. It allows to model the cohesive crack in tension (Figure 4.1a) and the overlapping crack in compression (Figure 4.1b).

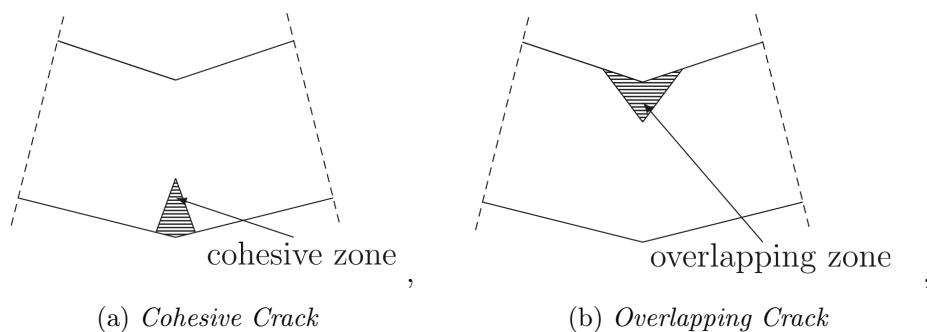


Figure 4.1: Tensile fracture with cohesive zone and compressive crushing with overlapping, [52].

The algorithm evaluates a specimen subjected to bending moment,  $M$  by means of a sectional analysis. The stress distribution is analysed as linear-elastic until the tensile stress at the intrados reaches the concrete tensile

strength or the compressive stress reaches the concrete compressive strength. When  $\sigma \geq \sigma_t$ , a cohesive crack starts to develop from the intrados, while, outside the crack, the material is modelled in the elastic field. In addition, if the crack mouth opening reaches the condition:  $w^t \geq w_{cr}^t$ , a stress free area arises. In the part of the specimen that is subjected to compression, when  $\sigma \geq \sigma_c$  crushing starts to develop in an analogous way. At the extrados, if  $w^c \geq w_{cr}^c$  the compressive stress drops to zero [63]. The Cohesive/Overlapping Crack Model represents an effective tool to investigate ductile-to-brittle transition and non-linear phenomena occurring in plain and reinforced concrete structures. In addition, it has been recently applied for the analysis of prestressed concrete elements subjected to flexural actions [66]. In particular, it is possible to study the effect of a straight steel strand layout, for a correct evaluation of the scale effects and the estimation of the maximum reinforcement percentage. Similarly to the evaluation of ordinary reinforcement, it is done by introducing the presence of the prestressed strands with a specific bond-slip constitutive law, to highlight the relationship between crack opening and steel response.

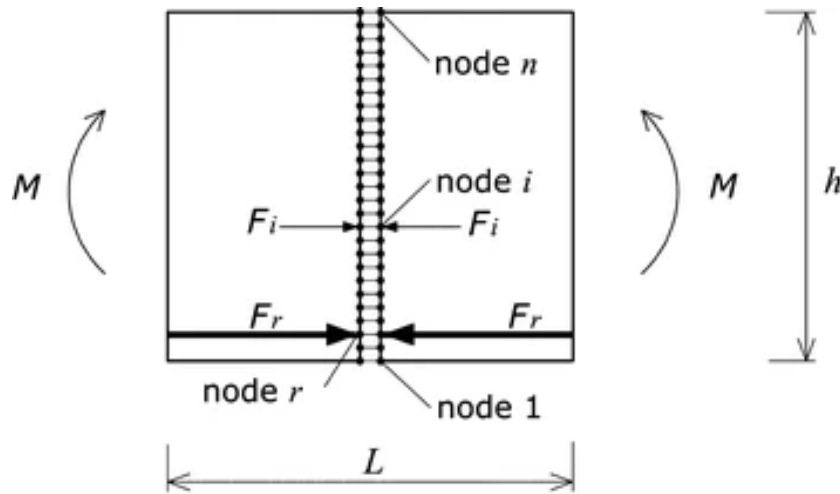


Figure 4.2: Cohesive/Overlapping Crack Model, finite nodes position in the numerical algorithm, [63].

The beam is modelled through a FEM approach, in which the midspan cross section is discretised in  $n$  nodes and  $(n - 1)$  segments. In this scheme, it

is possible to introduce the effect of ordinary reinforcement as well as prestressed steel strands at the node  $r$ , as shown in Figures 4.2-4.3.

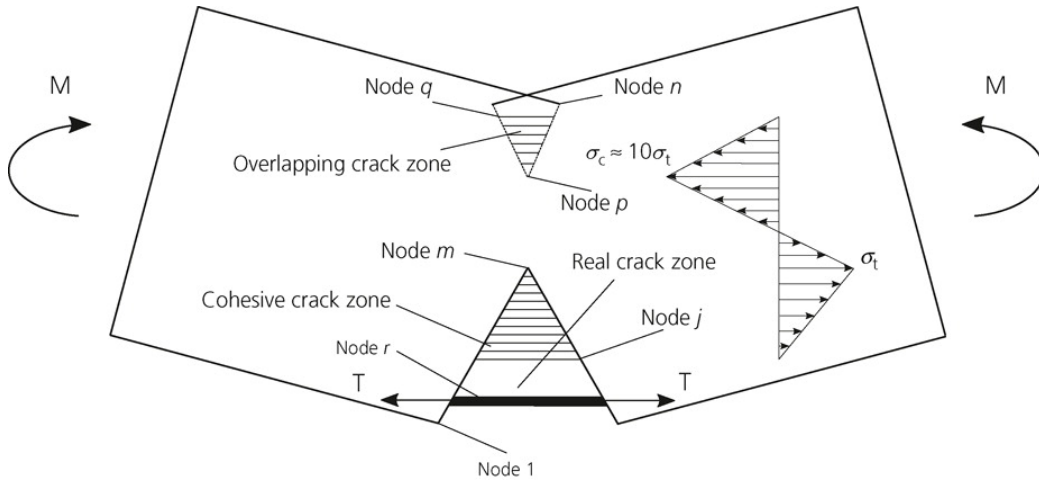


Figure 4.3: Cohesive/Overlapping Crack Model, force distribution according to the numerical algorithm, [67].

In Figure 4.3, the indices are referred to:

- $j$ : real cohesive crack tip;
- $m$ : fictitious cohesive crack tip;
- $p$ : fictitious overlapping crack tip;
- $q$ : real overlapping crack tip;
- $r$ : reinforcement node position.

The numerical step-by-step routine is controlled by the positions of the cohesive fictitious crack tip and of the overlapping fictitious crack tip. At each step, the tip that reaches the ultimate condition is computed and moved forward.

The governing system is:

$$\{w\} = [H]\{F\} + \{C\}M \quad (4.1)$$

In which:

- $\{w\}$ : vector of nodal crack opening/overlapping displacement;
- $[K]$ : matrix of coefficients of influence, with nodal displacements for unit applied nodal force  $\{F\}$ ;
- $\{F\}$ : vector of nodal forces;
- $\{C\}$ : vector of coefficients of influence, with nodal displacements for unit applied bending moment  $M$ ;
- $M$ : applied bending moment;

As shown in Figure 4.3, the model is solved taking into account the following conditions:

$$F_i = 0, \quad i = 1, 2, \dots, (j - 1), i \neq r \quad (4.2a)$$

$$F_i = F_t \left( 1 - \frac{w_i}{w_{cr}^t} \right), \quad i = j, \dots, (m - 1) \quad (4.2b)$$

$$w_i = 0, \quad i = m, \dots, p \quad (4.2c)$$

$$F_i = F_c \left( 1 - \frac{w_i}{w_{cr}^c} \right), \quad i = (p + 1), \dots, q \quad (4.2d)$$

$$F_i = 0, \quad i = (q + 1), \dots, n \quad (4.2e)$$

$$F_i = f(w_i) \quad i = r, \quad (4.2f)$$

Therefore, the system is given by  $2n$  equations and  $(2n + 1)$  unknowns,  $\{w\}$ ,  $\{F\}$  and  $M$ . An additional condition is needed, and it derives from the strength criterion governing the propagation process [68]. Starting from the original positions of the cohesive and the overlapping fictitious crack tips, the routine evaluates the external load that leads node  $m$  to reach the ultimate tensile force and the one that leads node  $p$  to reach the ultimate compressive force. The value of  $M$  is given by the minimum between the two external loads previously evaluated. Only the tip that reaches the ultimate strength is moved forward for the subsequent step of the analysis. Thus, crack opening and crushing are distinct phenomena that can take place independently.

The localised beam rotation,  $\theta$ , is given by:

$$\{D_F\}^T \{F\} + D_M M \quad (4.3)$$

Where:

- $\{D_F\}$  is the vector of coefficients of influence with the rotation generated by init nodal forces,  $\{F\}$ ;
- $D_M$  is the coefficient of influence that gives the rotation generated by unit bending moment,  $M$ .

As shown in Eqn.(4.2f), the beam reinforcement is taken into account as a specific layer, that is modelled by means of a bond-slip law. In case of ordinary reinforcement, the law proposed by Ruiz *et al.* [69] and Model Code 2010 [70] can be used:

$$\sigma_s = \sigma_y \frac{w^t}{w_y} \quad (4.4)$$

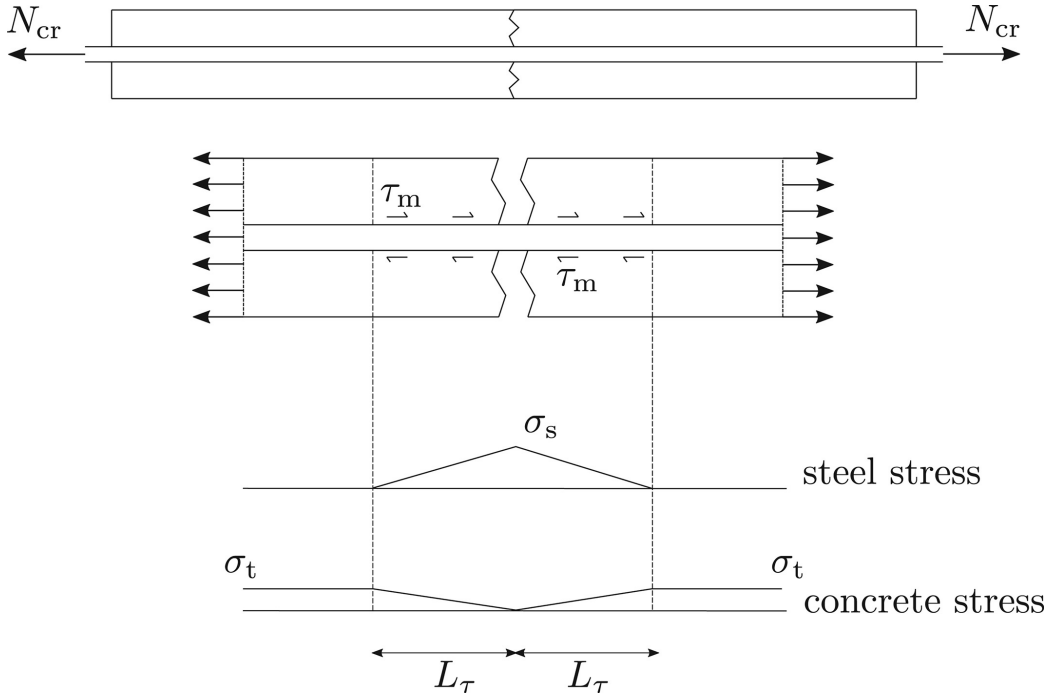


Figure 4.4: Steel-concrete interaction, [67].

A reinforced element of length  $2L_\tau$  and a crack at midspan is considered, as shown in Figure 4.4. This element is subjected to the action in steel,  $\sigma_s A_s$ , and to the shearing stress,  $\tau(x)$ , which is mutually transferred between concrete and steel. From the equilibrium of the element:

$$\sigma_s A_s = \int_0^{L_\tau} \pi \Phi \tau(x) dx \quad (4.5)$$

If an average value of the shearing stress is assumed:  $\tau(x) = \tau_m$ , the value of the stress transferring length,  $L_\tau$ , is given as in Eqn.(4.6)

$$L_\tau = \frac{\sigma_s A_s}{\pi \Phi \tau_m} \quad (4.6)$$

The crack opening can be written as the slip between concrete and steel along  $2L_\tau$ :

$$w^t = 2 \int_0^{L_\tau} [\epsilon_s(x) - \epsilon_{c0}] dx \quad (4.7)$$

Neglecting concrete contribution and introducing Eqn.(4.6) in Eqn.(4.7):

$$w^t = \frac{\sigma_s^2 A_s}{E_s \pi \Phi \tau_m} \quad (4.8)$$

From Eqn.(4.8) and Eqn.(4.4), it is possible to evaluate  $w_y$  and define steel constitutive law, as shown in Figure 4.5.

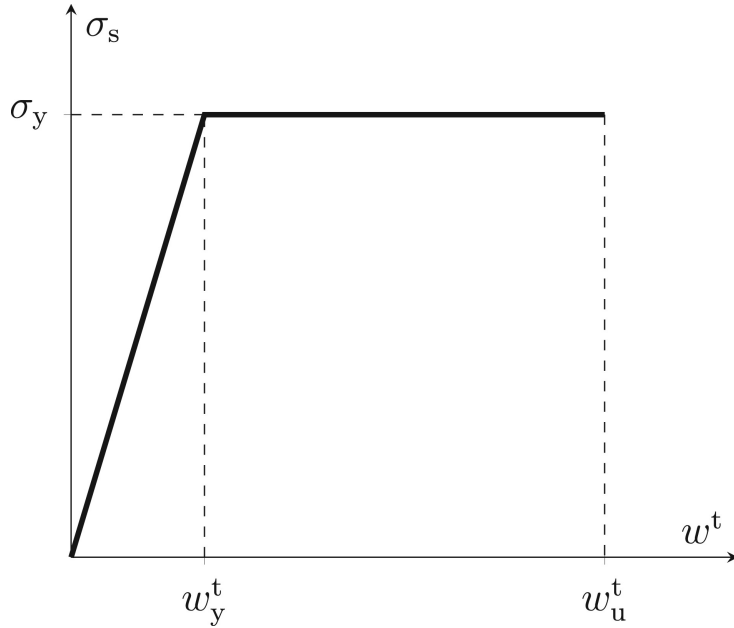


Figure 4.5: Steel constitutive law, [67].

The algorithm can analogously consider the presence of steel prestressed strands. In this case, the bond-slip relationship takes into account a linear variation of the steel stress from the cracked cross section,  $\sigma_p$ , to the point

at the distance  $L_\tau$ ,  $\sigma_0$ . Consequently, Eqn.(4.8) becomes:

$$w^t = \frac{(\sigma_p - \sigma_0)^2 A_{sp}}{E_s \pi \Phi_{\tau_m}} \quad (4.9)$$

In addition, the governing system of  $n$  equations has an additional term due to the nodal forces generated by prestressing,  $\{F_p\}$ .

$$\{w\} = [H]\{F\} + \{C\}M + [H]\{F_p\} \quad (4.10)$$

## Chapter 5

# A new algorithm for arches analysis

The following part of the Thesis describes an algorithm for arches structural analysis, adopting the principles of Non-Linear Fracture Mechanics and exploiting a FEM framework. In detail, the algorithm adopts the Cohesive/Overlapping Crack Model, which is described in the previous chapters, and it is developed as a further extension of the studies on the problem of off-centre compression in arches, carried out in the field of Linear Elastic Fracture Mechanics. The program is written using MatlabR2021a [71] and Python programming language [72]. In particular, the main routines of PyFEM software are exploited [73].

For the analysis of the arch global behaviour, it is necessary to consider the eventual initiation of fractures along the whole finite element model in different cross sections, and not just in one critical cross section, which should be formerly defined by the user. Thus, it requires the introduction of specific non-dimensional elements in the mesh, that are the so-called *zero-thickness elements*, in which the Cohesive/Overlapping law has to be introduced. The arch is firstly described by continuous elements only and failure criteria for the opening of cracks and for crushing are defined. When one of these criteria is reached, the mesh of the model is updated introducing the cohesive or overlapping zero-thickness elements, according to the type of failure. The concept of mesh updating, or remeshing, to represent a crack had been previ-

ously used by Needleman and Tvergaard [74, 75], even if in their first studies the finite element that reached failure was directly taken to vanish, without changing the nodal points. Afterwards, Needleman also introduced a cohesive zone type interface model [76] and, to allow for a more arbitrary direction of crack propagation, Xu and Needleman proposed the introduction of interface elements equipped with a cohesive zone between all continuum elements of the mesh [77].

## 5.1 Zero-thickness elements

In a FEM analysis, the opening and development of cracks can be analysed by introducing special joint elements. They are defined as *interface elements*, or *zero-thickness elements*, because they do not have geometrical dimensions. Therefore, they do not modify the model geometry but only the structural response. Zero-Thickness elements were idealised in 1967 by Ngo and Scordelis [78] for reinforced concrete beams to represent a crack opening (Figure 5.1). It was done through a separation of the elements adjacent to the section where the crack formation was assumed, assigning different nodal points and introducing a linkage between each side of the crack with linear springs (Figure 5.2). In addition, linkage elements may also be used to simulate weak discontinuities as the bonding relationship between steel and concrete.

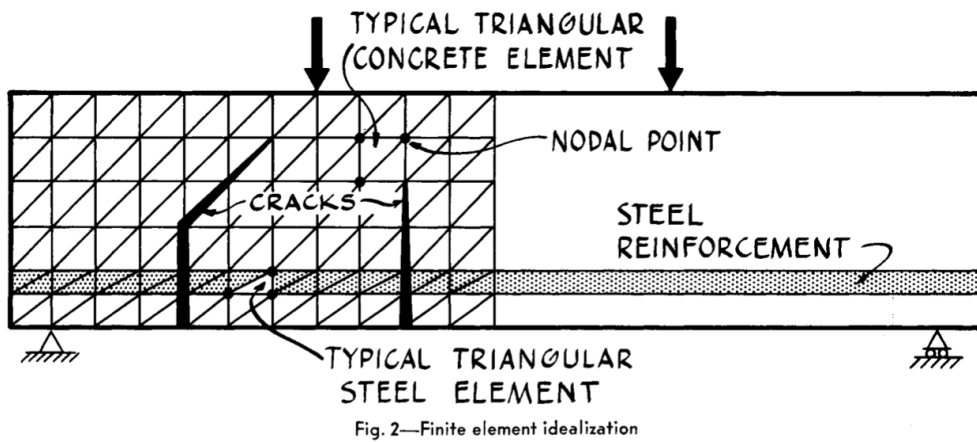


Figure 5.1: Finite Element idealisation with cracks according to Ngo and Scordelis, [78].

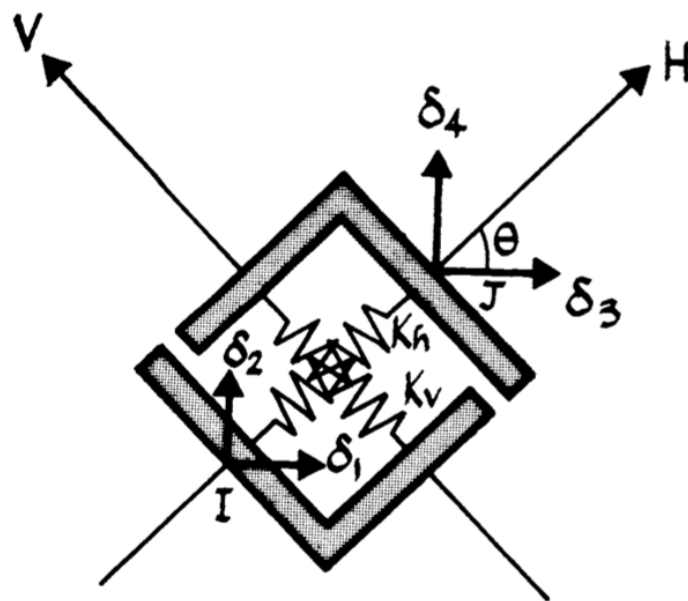


Figure 5.2: Linkage element from Ngo and Scordelis, [78].

Afterwards, in 1987, Wawrzynek and Ingraffea, from the Cornell Fracture Group, developed FRANC2D (FRacture ANalysis Code 2D) ([79] and Figure 5.3), a finite element based program that allows analysing crack propagation according to the classical criteria of Linear Elastic Fracture Me-

chanics. Shortly after, the Cornell Fracture Group began the development of FRANC3D to design a program capable of simulating 3D crack growth in engineering structures. Besides, in 1991, the Cohesive Crack Program (CCRAP) has been proposed by Valente *et al.* [80].

Further developments in this field have been proposed by Ingraffea and Saouma [81], and Rots [82], with a focus on reinforced concrete and prestressed reinforced concrete elements.

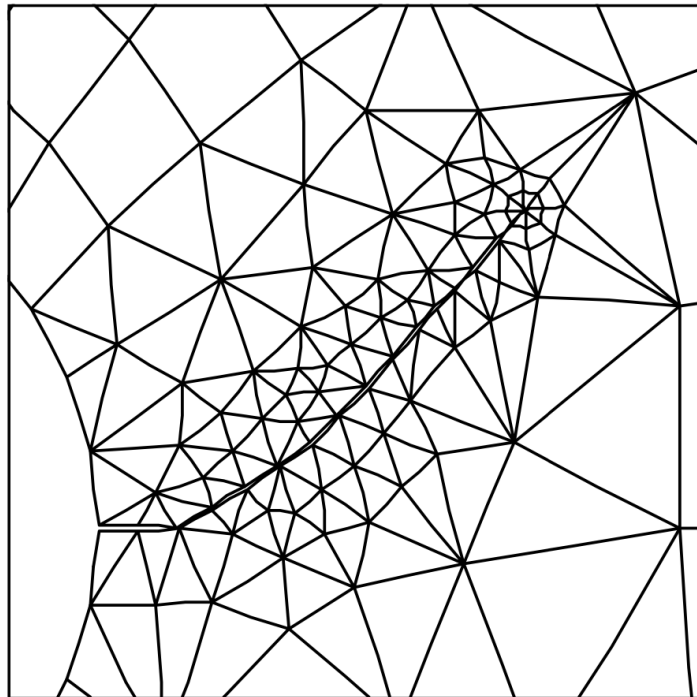


Figure 5.3: Finite Element mesh with a crack, [79].

More recently, the adoption of these elements has been enhanced due to the development of open-source programs, such as DEIP (Discontinuous Element Insertion Program) [83], the program proposed by Vinh Phu Nguyen [84], and PyFEM, which has been proposed by De Borst in 2012 [73]. The DEIP algorithm allows the introduction of zero-thickness elements, called *couplers* in 2D or 3D meshes. Each coupler is made of nodes from two elements between the surfaces of a possible fracture section, also called *facet*. It is realised through duplication of the nodes lying on the shared facet to effectively split the mesh along that surface, as shown in Figure 5.4. Thus,

the two sides initially coincide but may separate apart during the following steps of the analysis. Consequently, element connectivity is also updated allowing the introduction of different typologies of interface elements. DEIP has been integrated into WARP3D, an open-source code for nonlinear analysis of solids, which has been supported by many organisations (e.g. The U.S. Nuclear Regulatory Commission, NASA Ames Research Center, NASA Marshall Spaceflight Center, Air Force Research Laboratory) and is primarily used for fatigue and fracture simulations for materials under static, dynamic and thermal loadings [85].

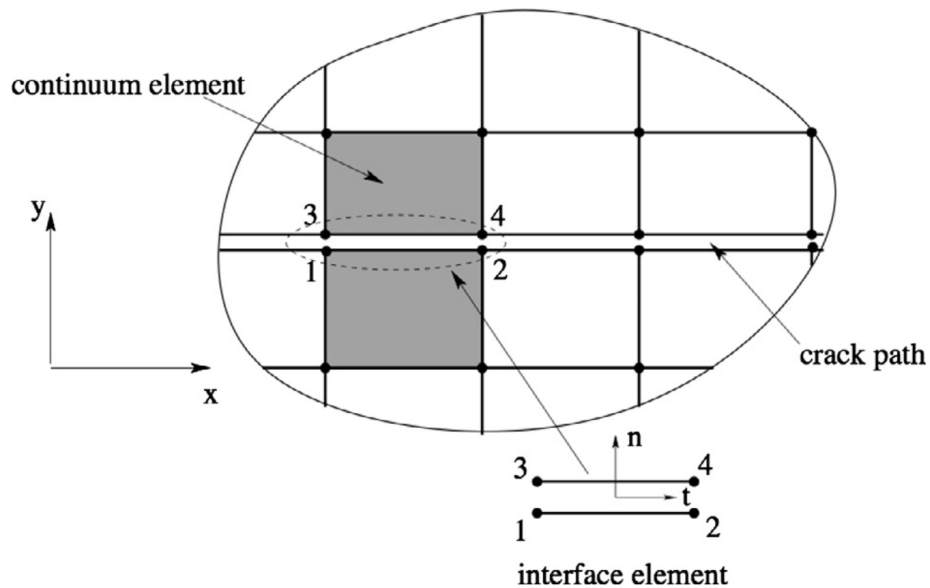


Figure 5.4: Discretisation of a generic domain with continuum elements and zero-thickness interface elements, [84].

## 5.2 Algorithm definition

The following section describes the theoretical framework of the algorithm. The system is firstly idealised as an assemblage of continuous finite elements which are interconnected at structural joints, with the possibility to introduce the interfaces in a reduced number of cross sections, that are defined as control sections, to reduce the algorithm computational effort.

The standard formulation for the finite element solution is the displacement-based method, and its primary relationship is the Virtual Work Principle. It asserts the equality between external virtual work (forces for relative displacements) and internal virtual work (stresses for relative deformations). More precisely, it can be asserted that the Virtual Work Principle constitutes the very definition of internal deformation work. It is also known as the “weak form” of the equilibrium equations because the equilibrium is only ensured for a subset of virtual displacement fields and may not be satisfied pointwise, which leads to an approximate solution of the actual displacement field.

Given a generic solid body and being  $V$  the three-dimensional domain occupied by the body and  $S$  the frontier of that domain, it is possible to define the statically admissible system of external forces (the volume loads,  $\{F\}$ , and the surface loads,  $\{t\}$ ).

In addition, a kinematically admissible system of displacements,  $\{u\}$ , and deformations,  $\{\epsilon\}$ , is introduced. For the Virtual Work Principle, in the case of the undamaged solid, the equilibrium is defined as:

$$\int_V \delta\{\epsilon\}^T \{u\} dV = \int_V \delta\{u\}^T \{F\} dV + \int_S \delta\{u\}^T \{t\} dS \quad (5.1)$$

In the case of a damaged solid having  $n$  cracks and  $r$  overlapping zones, the last term of the previous equation can be decomposed as:

$$\begin{aligned} \int_S \delta\{u\}^T \{t\} dS &= \sum \int_{S_{c,n}} \delta\{u\}^T \{p_c\} dS + \\ &+ \sum \int_{S_{t,r}} \delta\{u\}^T \{p_t\} dS + \int_{S_{res}} \delta\{u\}^T \{p\} dS \end{aligned} \quad (5.2)$$

In which  $S_{res} = S - \sum S_c - \sum S_t$ .

The first of the three terms represents the cohesive forces on the cracked

interface, while the second term represents the overlapping forces along the respective zone. The last term represents the real surface loads  $\{p\}$ , as shown in Figure 5.5.

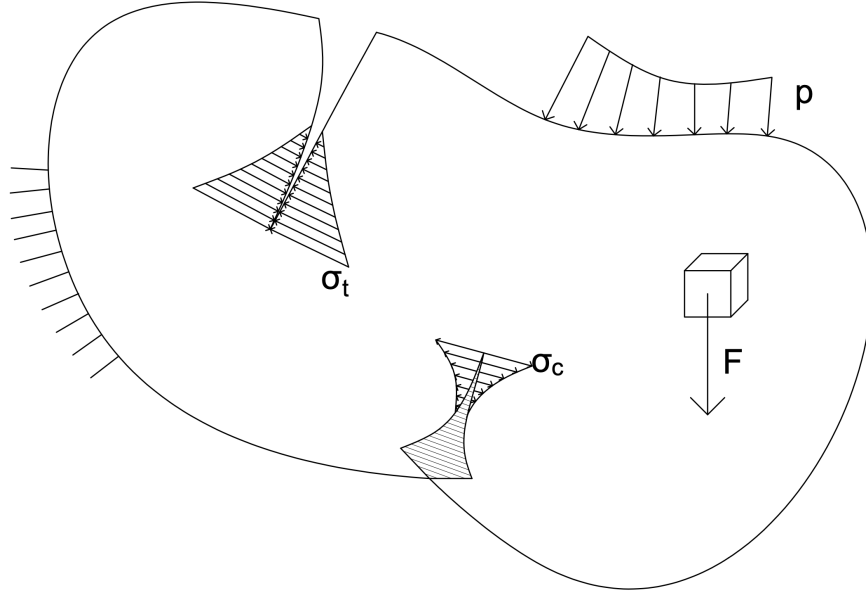


Figure 5.5: Scheme of a generic body subjected to crack opening and crushing.

In the finite element framework, the integration is carried out over the single elements domains, and the results are summed. The main variables are the displacement vectors at all the element nodes, called the nodal displacements,  $\{\bar{u}\}$ , and the elements variables are given by the following relationships:

$$\{u\} = [N]\{\bar{u}\} \quad (5.3)$$

$$\{\epsilon\} = [B]\{\bar{u}\} \quad (5.4)$$

$$\{\sigma\} = [D]\{\epsilon\} \quad (5.5)$$

Where,  $\sigma$  and  $\epsilon$  are the elements stress and strain, and  $\{u\}$  is the vector of the elements displacements.

- $[N]$  is the displacement interpolation matrix;
- $[B]$  is the strain-displacement matrix, in which the rows are obtained by appropriately differentiating and combining the rows of the  $[N]$  matrix;
- $[D]$  is the matrix of the constitutive law.

In detail, the first term of the Eqn.(5.1) is the internal virtual work and it can be rewritten as it follows, adopting Eqn.(5.4) and Eqn.(5.5) and introducing the sum over the elements, m:

$$\delta\{\bar{u}\}^T \sum_m \int_V [B]^T [D] [B] dV \{\bar{u}\} \quad (5.6)$$

Neglecting the external virtual work given by the volume loads, it is possible to study the effect of surface loads only.

The constitutive laws for the cohesive and overlapping interface elements have to be defined. These elements are introduced only when the nodal stress reaches the tensile ultimate condition,  $\sigma_t$ , or the compressive ultimate condition,  $\sigma_c$ . Therefore, the constitutive laws should model the behaviour of the process zone and the stress-free area. Assuming linear cohesive and overlapping softening laws and neglecting the shearing stresses on the crack faces, the cohesive and the overlapping softening matrices are evaluated as follows.

$$[C] = \begin{bmatrix} \sigma_t/w_{cr}^t & 0 & 0 \\ 0 & 0 & 0 \\ 0 & 0 & 0 \end{bmatrix} \quad (5.7)$$

$$[T] = \begin{bmatrix} \sigma_c/w_{cr}^c & 0 & 0 \\ 0 & 0 & 0 \\ 0 & 0 & 0 \end{bmatrix} \quad (5.8)$$

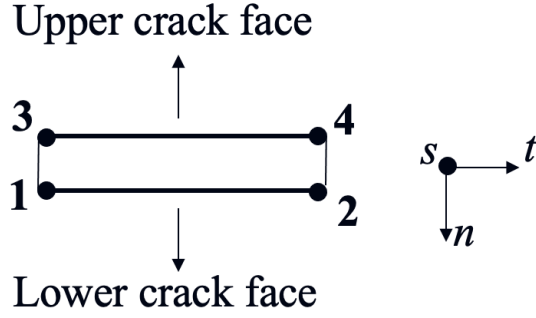


Figure 5.6: Scheme of an interface element.

The interface element is divided in the upper and the lower crack faces, as shown in Figure 5.6. Consequently, the displacements of these two faces are evaluated by means of the shape functions,  $N_1$  and  $N_2$ :

$$\begin{bmatrix} N_1 \\ N_2 \end{bmatrix} = \begin{bmatrix} 0.5(1 - \xi) \\ 0.5(1 + \xi) \end{bmatrix} \quad (5.9)$$

$$\begin{pmatrix} u_n^i \\ u_n^s \\ u_t^i \\ u_t^s \\ u_s^i \\ u_s^s \end{pmatrix} = \begin{bmatrix} N_1 & N_2 & 0 & 0 & 0 & 0 & 0 & 0 & 0 & 0 & 0 & 0 \\ 0 & 0 & N_1 & N_2 & 0 & 0 & 0 & 0 & 0 & 0 & 0 & 0 \\ 0 & 0 & 0 & 0 & N_1 & N_2 & 0 & 0 & 0 & 0 & 0 & 0 \\ 0 & 0 & 0 & 0 & 0 & 0 & N_1 & N_2 & 0 & 0 & 0 & 0 \\ 0 & 0 & 0 & 0 & 0 & 0 & 0 & 0 & N_1 & N_2 & 0 & 0 \\ 0 & 0 & 0 & 0 & 0 & 0 & 0 & 0 & 0 & 0 & N_1 & N_2 \end{bmatrix} \begin{pmatrix} u_{n1} \\ u_{n2} \\ u_{n3} \\ u_{n4} \\ u_{t1} \\ u_{t2} \\ u_{t3} \\ u_{t4} \\ u_{s1} \\ u_{s2} \\ u_{s3} \\ u_{s4} \end{pmatrix} \quad (5.10)$$

Eqn.(5.10) can be concisely written as:  $\{u\} = [N]\{\bar{u}\}$ .

The interface elements response depends on the crack opening  $w$ , or the analogous overlapping, which is evaluated adopting the matrix  $L$ :

$$\{w\} = [L]\{u\} \quad (5.11)$$

Where:

$$[L] = \begin{bmatrix} -1 & 1 & 0 & 0 & 0 & 0 \\ 0 & 0 & -1 & 1 & 0 & 0 \\ 0 & 0 & 0 & 0 & -1 & 1 \end{bmatrix} \quad (5.12)$$

$$\{w\} = \begin{pmatrix} w_n \\ w_t \\ w_s \end{pmatrix} \quad (5.13)$$

Thus, the stress transferred through the crack faces is defined as:

$$\{\sigma\} = [S]\{w\} = [S][L][N]\{\bar{u}\} \quad (5.14)$$

In which,  $[S]$  is the generic softening matrix, and it is equal to  $[C]$  or  $[T]$  according to the kind of failure. Introducing Eqn.(5.14) into Eqn.(5.2), the contribution from the cracked zone is written as:

$$\int_{S_{c,n}} \delta\{u\}^T \{p_c\} dS = \delta\{\bar{u}\}^T \sum_m \int_{S_{c,m}} [C][L][N] dS \{\bar{u}\} \quad (5.15)$$

In analogy, the contribution from the overlapping zone is written as:

$$\int_{S_{t,n}} \delta\{u\}^T \{p_t\} dS = \delta\{\bar{u}\}^T \sum_m \int_{S_{t,m}} [T][L][N] dS \{\bar{u}\} \quad (5.16)$$

In addition, introducing the load factor,  $\lambda$ :

$$\int_{S_{res}} \delta\{u\}^T \{p\} dS = \delta\{\bar{u}\}^T \lambda \sum_m \int_{S_{res,m}} \{p_0\} dS \quad (5.17)$$

As the equilibrium should be satisfied for each value of  $\delta\{\bar{u}\}^T$ , the governing equation can be written as:

$$\begin{aligned} & \left( \sum \int [B]^T [D] [B] dV - \sum \int [C][L][N] dS - \sum \int [T][L][N] dS \right) \{\bar{u}\} = \\ & = \lambda \sum \int \{p_0\} dS \end{aligned} \quad (5.18)$$

Introducing :

- $[K] = \sum \int [B]^T [D] [B] dV;$
- $[S_C] = \sum \int [C] [L] [N] dS;$
- $[S_T] = \sum \int [T] [L] [N] dS.$

The governing equation becomes:

$$\left( [K] - [S_C] - [S_T] \right) \{\bar{u}\} = \lambda \{f\} \quad (5.19)$$

This result is equal to the one obtained by Bocca, Carpinteri, Valente (1991) [80]. In the first step of the analysis,  $[S_C]$  and  $[S_T]$  are null matrices, and the equation is simplified. When failure is reached, and interface elements are introduced through remeshing, the softening matrices modify the first term of the Eqn.(5.19), thus, the equilibrium is not satisfied, and an error can be evaluated. Consequently, an iterative procedure is applied to solve the system reducing the error until a specific tolerance is reached.

# Chapter 6

## Description of the routines

In this part of the Thesis, the new algorithm is presented by means of a detailed description of its routines. The program for the elastic-plastic-softening evolutionary analysis of arch structures is mainly written using Python programming language, adopting the basic routines introduced in PyFEM and keeping the theoretical framework of the Cohesive/Overlapping Crack Model. It is constituted by the main routine, called *Master.py* and a series of subroutines that are separate codes used for specific functionalities of the program.

### 6.1 The routine *Master.py*

The routine *Master.py* is the main script of the program. It is able to call the other subroutines and define the procedures to be repeated for each step of the analysis until a termination criterion is reached. In detail, this routine firstly defines the initial mesh that represents the arch structure in the FEM framework. To do so, it calls the routine *MeshGenerator.py* and reads in the input file, which has the extension ".dat".

It reads as well a second input file, with the extension ".pro", from which it gets the information about the elements constitutive laws, the solver and the primary output management.

Afterwards, it processes the input data by identifying a subset of the arch cross sections as the control sections. It is theoretically possible to consider all the cross sections generated by the model discretisation. However,

a reduced number of them allows reducing the computational effort of the program.

Finally, the routine *Master.py* defines the sequence of instructions that must be repeated in each analysis cycle until the number of cycles reaches the maximum value imposed by the user or until four hinges are formed. The criterion of hinges formation is related to the principles of plastic Limit Analysis, and in this algorithm, a hinge is introduced when the cracking failure affects the entire cross section, except for one element.

In each cycle:

- The system is firstly solved through the Newton-Raphson iterative method implemented in the sub-routine *CohesiveOverlappingSolver.py*;
- Assuming a linear behaviour of the structure for a small calculation step, the routine evaluates the load factor,  $\lambda$ , that generates the ultimate strength in each fictitious tip (in tension as well as in compression). In the initial phase, the fictitious crack tips are defined as the external nodes of each control section;
- From the list of load factors, the critical value of  $\lambda$  is assumed as the minimum of the absolute values;
- The algorithm identifies which is the node that reaches the ultimate strength and the kind of failure;
- Given the critical  $\lambda$ , the external load vector is updated, and the system is solved a second time with the same iterative method;
- The mesh is updated introducing the cohesive or overlapping interface elements in the positions found in the previous steps. To do so, DEIP MatLab tool is exploited. In addition, the fictitious crack tips are updated according to the new mesh.

## 6.2 The routine `MeshGenerator.py`

*MeshGenerator.py* is the routine that enables the definition of the initial mesh. It defines the arch geometry and its discretisation. Indeed, it evaluates the coordinates of the nodes, the continuous elements, the external constraints, and the initial external forces. The arch geometry can be easily estimated through the parametric equations of an ellipse or a circumference. It is possible to adopt a fixed cross section depth  $s$ , or a variable one, as in the case of Mosca Bridge. In the case studies, arcs of circumferences have been used. Given the arch span length,  $\ell$ , and its rise,  $r$ , the routine evaluates which are the characteristics of the arch of the circumference to be used, i.e., the radius,  $R$ , and the arch inclination at the abutment level,  $\theta_0$ . From these input data, it generates the mesh. The external constraints are modelled to rigidly fix the arch at the abutments, while the external forces are designed to be uniformly distributed along the span length. *MeshGenerator.py* finally writes the input file *arch.dat* according to the syntax requirements imposed by PyFEM.

## 6.3 The file `arch.pro` and the related sub-routines

The *arch.pro* file is used as an additional input file, which provides all information about materials, constitutive laws, solver type, and the required output. In the first input file, *arch.dat*, each element is assigned to a specific category. In the first cycle, there are only continuous elements but, from the second cycle, cohesive and overlapping interface elements may be present as well. Therefore, in the file *arch.pro*, these elements categories are defined by assigning the constitutive law and the required mechanical properties.

The constitutive laws are reported on the following sub-routines:

- *PlaneStress.py* ;
- *Cohesive.py*;
- *Overlapping.py*.

The continuous elements follow the constitutive law defined by *PlaneStress.py*, in accordance with the theory of small deformations. They are modelled with

a linear elastic behaviour, which is governed by the material elastic modulus,  $E$ , and the Poisson coefficient,  $\nu$ .

The zero-thickness elements, or interfaces, are instead defined with more specific constitutive laws, to correctly represent the process zone.

The routine *Cohesive.py* is governed by the values of the fracture energy,  $G_F$ , and the ultimate tensile strength,  $\sigma_t$ . The stress state on the element is defined as a function of the crack opening,  $w$ , with a linear behaviour.

Therefore:

$$w_{cr}^t = 2 \frac{G_F}{\sigma_t} \quad (6.1)$$

If  $w < w_{cr}^t$ :

$$\begin{cases} \sigma = \sigma_t(1 - w/w_{cr}^t) \\ \tau = 0 \end{cases} \quad (6.2)$$

Else:

$$\begin{cases} \sigma = 0 \\ \tau = 0 \end{cases} \quad (6.3)$$

In analogy, the routine *Overlapping.py* is governed by the values of the crushing energy,  $G_C$ , and the ultimate compressive strength,  $\sigma_c$ . The stress state on the element is defined as a function of the fictitious overlapping,  $w$ , with a linear behaviour.

Therefore:

$$w_{cr}^c = 2 \frac{G_C}{\sigma_c} \quad (6.4)$$

If  $w < w_{cr}^c$ :

$$\begin{cases} \sigma = \sigma_c(1 - w/w_{cr}^c) \\ \tau = 0 \end{cases} \quad (6.5)$$

Else:

$$\begin{cases} \sigma = 0 \\ \tau = 0 \end{cases} \quad (6.6)$$

The *arch.pro* file also defines the basic output properties through some PyFEM subroutines (i.e. *OutputManager.py*, *OutputWriter.py*, *MeshWriter.py* and *GraphWriter.py*). They allow to derive graphs (load-displacement), lists with stress values and properties of each node of interest, and animations of the model. In addition, *arch.pro* defines the system solver, which is described by the *CohesiveOverlappingSolver.py* routine.

## 6.4 The routine *CohesiveOverlappingSolver.py*

The *CohesiveOverlappingSolver.py* sub-routine is the one in which the resolution procedure is implemented. It is recalled several times in the master file, so as to initially solve the system with the new mesh, then evaluate the load increment required to reach cracking, and evaluate the state of the system in the incipient cracking condition.

In the preamble, the routine initialises the basic parameters of the solver method, such as the tolerance and the maximum number of iterations. Consequently, the sub-routine defines the function *run*, which is called in the *Master.py*. After the evaluation of the solver status, the function retrieves the state of the system:

- $\{a\}$ : state of the system in terms of displacements;
- $\{\Delta a\}$ : displacements variation at the present step;
- $\{\hat{f}\}$ : vector of external forces at the present step.

The error is fixed to a unit value and then the stiffness matrix,  $[K]$  and the internal forces  $\{f_{\text{int}}\}$ , are evaluated. The governing equation is given by:

$$[K]\{\delta a\} = \{\hat{f}\} - \{f_{\text{int}}\} \quad (6.7)$$

The model is solved by exploiting an approximate method, which allows the Eq.(6.7) result to be obtained with a high degree of accuracy. It is the Newton-Raphson iterative method, also called the method of tangents, which is based on the geometrical idea of approximating, at each step, the graph of the function by the tangent line.

While the error is higher than the imposed tolerance, the Eq.(6.7) is solved to get  $\{\delta a\}$  and it is used to update the displacements:

$$\{\Delta a\} = \{\Delta a\} + \{\delta a\} \quad (6.8a)$$

$$\{a\} = \{a\} + \{\delta a\} \quad (6.8b)$$

The values of  $[K]$  and  $\{f_{\text{int}}\}$  are evaluated again with the new displacement state and the error is analysed:

$$\text{error} = \frac{\|\{\hat{f}\} - \{f_{\text{int}}\}\|}{\|\{\hat{f}\}\|} \quad (6.9)$$

## 6.5 The routine `MeshManagement.py`

The *MeshManagement.py* sub-routine is a crucial one. It allows updating the mesh, introducing the interface elements and specifying their constitutive law. In the first version of the algorithm, this routine adopts the functions of DEIP [83], which is written in the MatLab environment. Therefore, it is necessary to import MatLab engine in Python, to be able to exploit DEIP re-meshing capability.

The function *MeshUpdater* requires the definition of the following quantities:

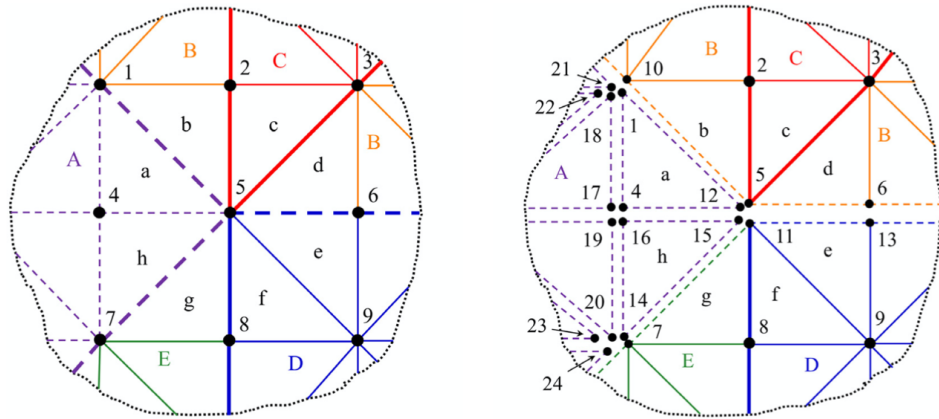
- *Coordinates*, a list that gives the coordinates of each node and its ID.
- *NodesOnElement*, which gives the nodes that compose each finite element and its ID.
- *RegionOnElement*, which defines the regions, i.e. the sets of contiguous elements giving a non convex sub-domain. These regions are used to insert the interface elements, they are helpful to represent fibres or grains in polycrystalline materials. However, in this case, each element constitutes a single region.
- *Intertypes*, which gives the positions where interface elements should be introduced.

It is a square lower triangular matrix having the dimension of the number of regions. It has only zero and unit values. The position  $(i, j)$  of

each unit value denotes that it is necessary to insert an interface element (also called coupler) in the facet between the regions  $i$  and  $j$ . If  $Intertypes$  has unit values in the diagonal positions, it means that all elements within the corresponding region must be split.

Given a target position, that defines the nodes where the failure occurs, the *MeshUpdater* updates the  $Intertypes$  by introducing a unit value in the corresponding position. Consequently, it applies the DEIP functions to duplicate the nodes and update the above-mentioned lists (*Coordinates*, *NodesOnElement*, *RegionOnElement*) An example of node duplication and re-meshing is given in Figure 6.1, where 5 regions are defined and the  $Intertypes$  is the one defined in Eqn.(6.10)

$$Intertypes = \begin{bmatrix} 1 & 0 & 0 & 0 & 0 \\ 1 & 0 & 0 & 0 & 0 \\ 1 & 0 & 0 & 0 & 0 \\ 1 & 1 & 0 & 0 & 0 \\ 1 & 0 & 0 & 0 & 0 \end{bmatrix} \quad (6.10)$$



(a) Conforming mesh containing regions that illustrate interfaces (between regions) and intrafaces (within a specific region) (b) Resulting mesh after node duplication along cut interfaces and intrafaces

Figure 6.1: Example 2D linear triangular finite element mesh, in which the regions are identified by capital letters, the elements are identified by lower-case letters and the nodes are identified by numbers, [83].

Finally, the routine writes a new input file, *arch.dat*, in which the cohesive and overlapping interface elements are specified.

## 6.6 The routine `OutputDiagrams.py`

The *OutputDiagrams* sub-routine is realised in order to export the results in the desired step of the analysis. It allows to get the stress data for each node and to evaluate the stress components in the polar reference system  $(\sigma_n, \sigma_\theta)$ . Consequently, it evaluates the resulting axial force,  $N$ , for each cross section of the arch model as well as the resulting bending moment,  $M$ , and it gives the eccentricity,  $e$ , of the compressive force:

$$M = Ne \tag{6.11}$$

These output data are subsequently used to plot the diagrams of the arch stress characteristics and the thrust line. The load-displacement curves, as well as the mesh representation, are instead provided by the original PyFEM output routines, which are recalled in the *arch.pro* file.

# Chapter 7

## Algorithm results

The new algorithm for arches evolutionary analysis is applied for the evaluation of different case studies. After the first section on the assumed mechanical properties, the second section presents a parametric analysis on the arches scale effects, and the third section presents the real case study of the Mosca bridge. The analyses are specialised for circular arches, and the capability to implement a variable depth is introduced for the Mosca bridge case study. A focus is given to the effects of the mesh discretisation and the mechanical parameters.

### 7.1 Material mechanical properties

The definition of the model in the FEM framework requires the assignment of the materials constitutive laws and their mechanical parameters, which are reported in the *arch.pro* file. For concrete simulation, these parameters reflect the average mechanical characteristics that are given by plain concrete. Therefore, for the continuous elements, the elastic modulus,  $E$ , and the Poisson coefficient,  $\nu$ , are fixed to:

- $E = 30000$  MPa;
- $\nu = 0.15$ .

The cohesive interface elements are described by the values of the fracture energy,  $G_F$ , and the ultimate tensile strength,  $\sigma_t$ :

- $G_F = 0.14$  N/mm;
- $\sigma_t = 2.6$  MPa.

The overlapping interface elements are described by the values of the crushing energy,  $G_C$ , and the ultimate compressive strength,  $\sigma_c$ :

- $G_C = 30.0$  N/mm;
- $\sigma_c = 30.0$  MPa.

A deep analysis would be necessary to correctly fix the masonry constitutive laws for each case study. However, from the literature review, it is observed that the evaluation of masonry mechanical characteristics may be complex, especially in terms of fracture energy,  $G_F$ , and crushing energy,  $G_C$ . Consequently, masonry arches mechanical properties are firstly assumed, as follows, mainly with reference to the Mosca bridge case study with the LEFM approach [33].

The continuous elements are described by the elastic modulus,  $E$ , and the Poisson coefficient,  $\nu$ :

- $E = 50000$  MPa;
- $\nu = 0.2$ .

The ultimate strength in tension as well as in compression are fixed to:

- $\sigma_t = 0.3$  MPa;
- $\sigma_c = 50.0$  MPa.

The value of the fracture energy,  $G_F$ , is evaluated from the relationship between  $G_F$  and the critical stress intensification factor  $K_{Ic}$  which in Mode I is given by the following formula:

$$G_F = \frac{K_{Ic}^2}{E} \quad (7.1)$$

This equation expresses the equivalence between the local or tensional fracture propagation criterion proposed by Irwin and the global or energetic criterion proposed by Griffith.

In which:

- $K_{Ic} = 100 \text{ daN/cm}^{3/2}$ ;
- $G_F = 0.02 \text{ N/mm}$ .

Due to the lack of experimental values for the determination of  $G_C$ , it is fixed to  $50\text{N/mm}$  keeping an increase of approximately three orders of magnitude with respect to the value of  $G_F$ .

## 7.2 Scale effects analysis

The algorithm is adopted for the analysis of scale effects that may occur in arches. Three different scales are analysed in order to compare the resulting behaviours.

The geometry of the three arcs is defined based on the span  $\ell$ , the rise,  $r$ , and the depth,  $h$ . The shallowness ratio is fixed to  $1 : 3.3$ , while the slenderness ratio is fixed to  $1 : 10$ . Instead, the scale factor between the models is  $1 - 10 - 100$ .

The small scale arch has:

- $\ell = 2 \text{ m}$ ;
- $r = 0.3 \text{ m}$ ;
- $h = 0.1 \text{ m}$ .

The medium scale arch has:

- $\ell = 20 \text{ m}$ ;
- $r = 3 \text{ m}$ ;
- $h = 1 \text{ m}$ .

The large scale arch has:

- $\ell = 200$  m;
- $r = 30$  m;
- $h = 10$  m.

Each arch is analysed with the same mesh discretisation and the same mechanical properties to carry out a comparison. In addition, the number of controlled cross sections (i.e. the cross sections where the damaging process may occur) is fixed to 17 to reduce the computational effort, with respect to the evaluation of the damaging process in each cross section of the mesh. The same comparison is reiterated by adopting two mesh discretisations, to highlight the mesh effect on the local instabilities. The result is given in terms of load-displacement curves, as shown in Figure 7.1.

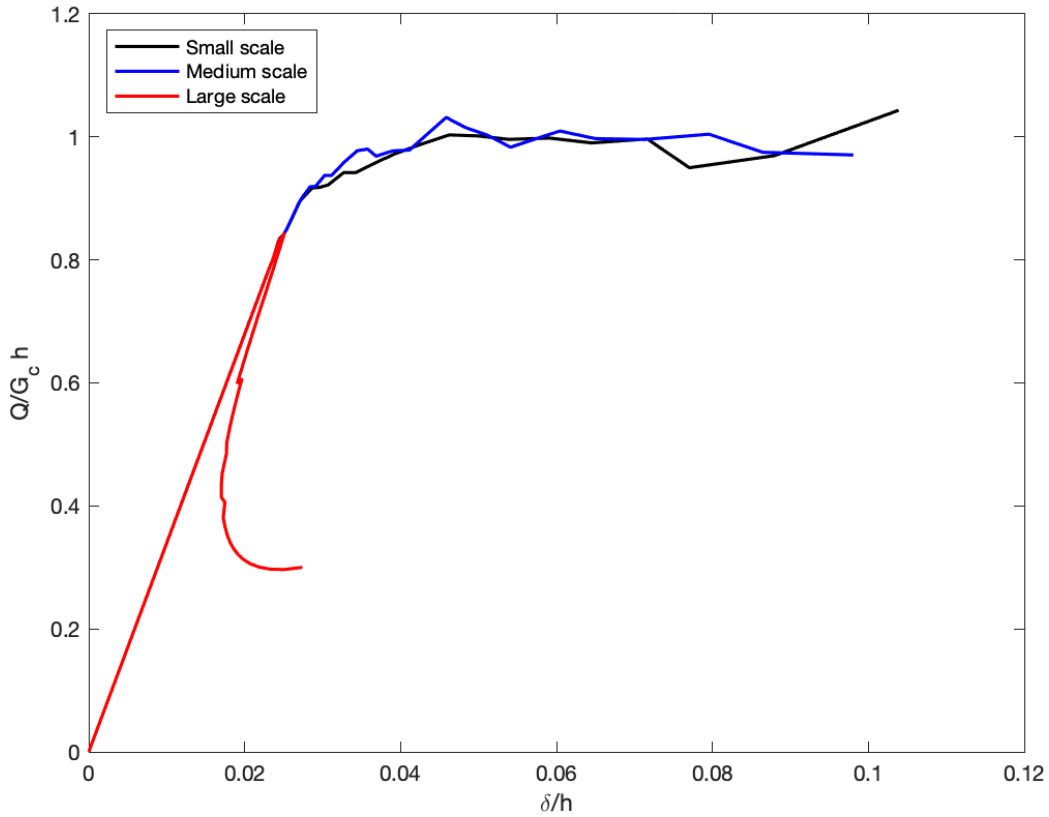


Figure 7.1: Comparison between the Load-Displacement curves for the key-stone node of the three arch scales, with a dense mesh.

In these curves, the vertical axis represents the total variable load,  $Q$ , that is applied on the structure as a uniformly distributed one,  $q$ . To get comparable results, it is reduced to a dimensionless form:  $Q/(G_C h)$ . In analogy, the vertical displacement,  $\delta$  is divided by the related value of  $h$ .

The curve for the medium scale and the curve for the small scale are similar. It is observed that the large scale model exhibits a globally brittle behaviour, with a global snap-back and a pseudo-plastic plateau section. In contrast, the smaller scale models exhibit a pseudo-ductile behaviour.

A second effect can be observed, as the peak value of the large scale model occurs for lower values of load with respect to the smaller models. In addition, local snap-backs are also present in all three models since the analysis is

driven by the cracking process. Although notably, such local instabilities are higher in the larger scale arches, while, in the smaller scale arch, the curve is less jagged.

The results proposed in Figure 7.1 are obtained with an averagely dense mesh with 5781 nodal points and 5600 finite elements. Since the computational effort is high, the analysis is reiterated with a less dense mesh having 1491 nodal points, and 1400 finite elements, (Figure 7.2). This discretisation is necessary to accurately simulate the development of the process zone on the arch depth, still guaranteeing a good shape factor in the finite elements.

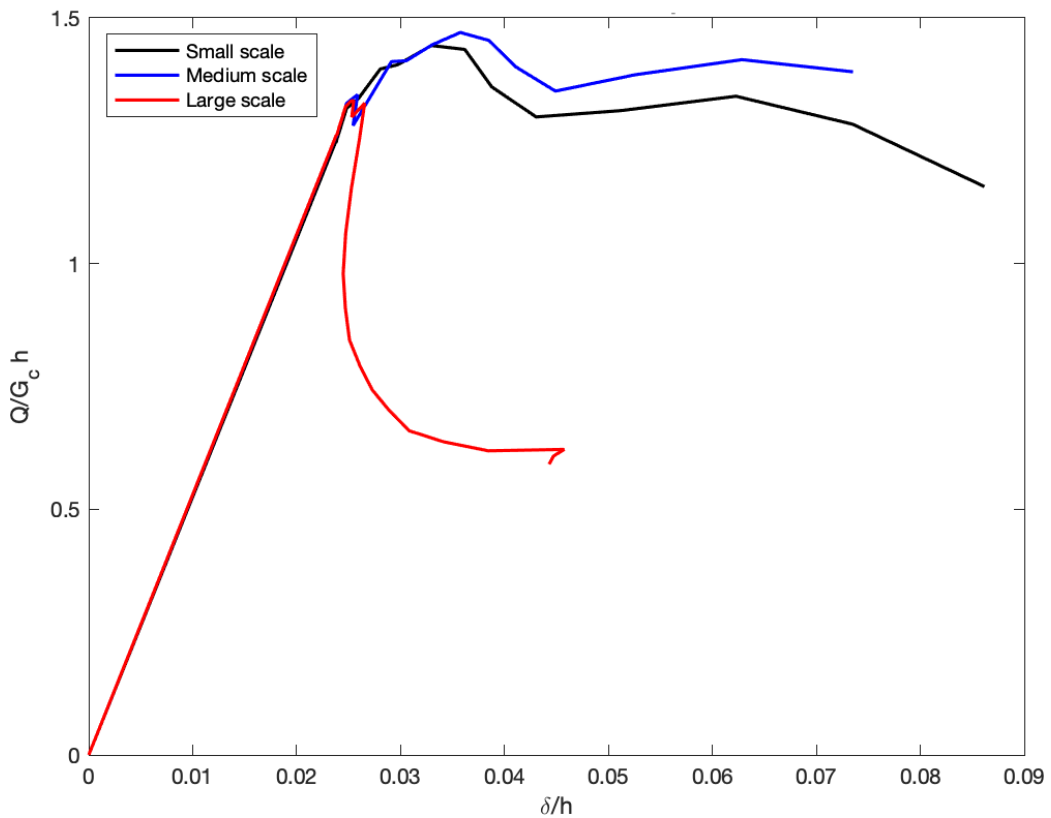


Figure 7.2: Comparison between the Load-Displacement curves for the key-stone node of the three arch scales, with a less dense mesh.

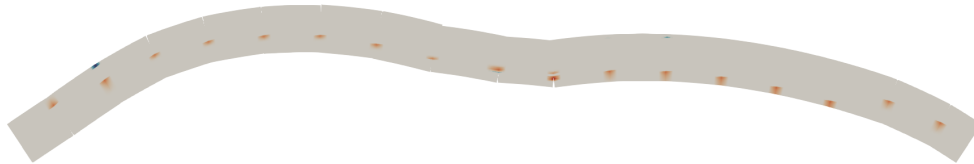
The main difference between the two discretisations is the degree of curve detail, i.e., the visibility of local instabilities, which disappears with the looser

mesh. However, the global behaviour is still correctly evaluated.

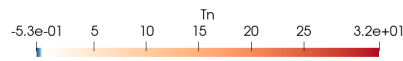
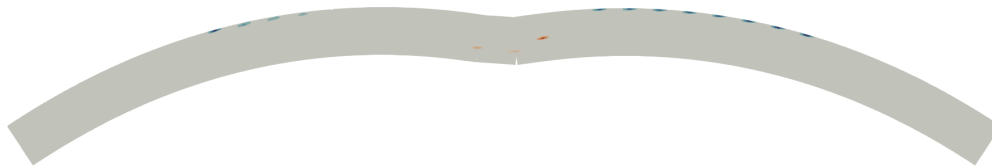
It can be seen that each of the three arch models reaches failure after the realisation of three hinges in the central part of the arch (Sections 8-9-10). In these cross sections, crushing failure at the arch extrados is initially prevalent, while, in the second part of the analysis, cracking also occurs at the arch intrados. It is shown in Figure 7.3, which represents the tensions at the interfaces for the different models.



(a) *Small scale arch.*



(b) *Medium scale arch.*



(c) *Large scale arch.*

Figure 7.3: Comparison between the three arch models in the deformed configuration with the interface tensions, from ParaView. The displacements are subjected to a scaling factor equal to 10.

In the small and medium scale arches, crushing is also prevalent at the intrados of the other cross sections (Figures 7.3a-7.3b). Instead, the large scale model shows a higher effect of cracking at the extrados of the lateral cross sections (Figure 7.3c). With a focus on the large scale arch, Figure 7.4 shows

the process of damage that occurs in the three central cross sections, where both the cohesive and the overlapping process zones are visible, and Figure 7.5 shows the process of cracking that occurs in the last step of the analysis at the extrados of the arch. These figures report the displacements with a scale factor equal to 10 in order to enhance their clarity.

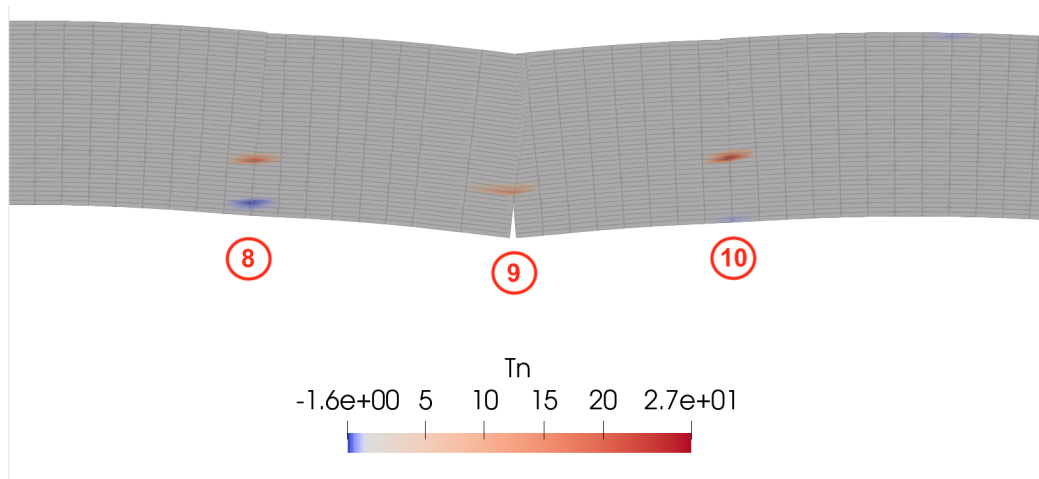
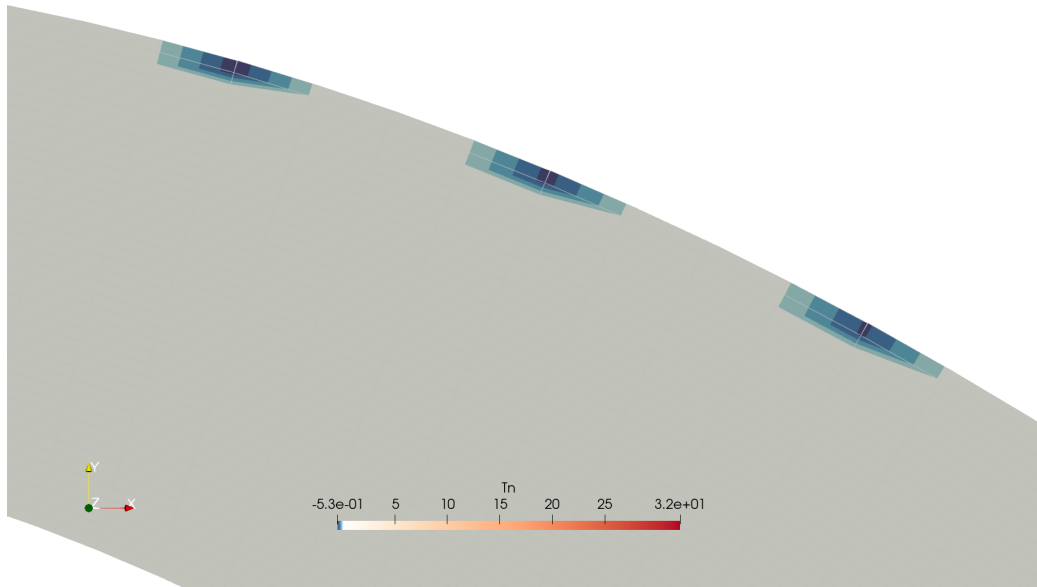
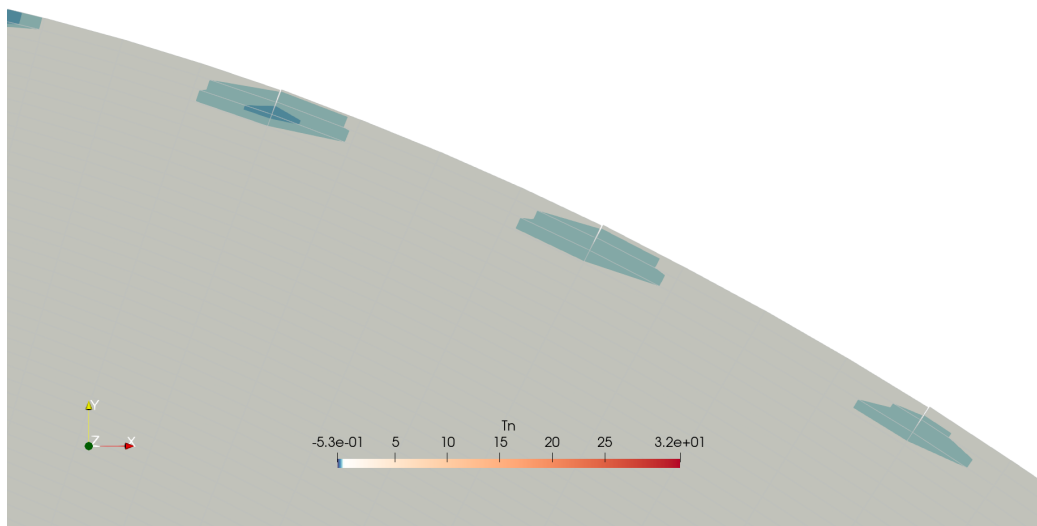


Figure 7.4: Detail of the keystone cross section in the deformed configuration with the interface tensions at the end of the analysis, from ParaView. The displacements are subjected to a scaling factor equal to 10.



(a) *Step 31.*



(b) *Step 32.*

Figure 7.5: Detail of the lateral cross sections in the deformed configuration with the interface tensions at the two final steps of the analysis, from ParaView. The displacements are subjected to a scaling factor equal to 10.

The load-displacement curve of the small scale arch is afterwards analysed by means of the identification of three significant steps, as shown in Figure 7.6. The curve shows an initial elastic branch until it reaches the peak value of  $q$  in step 9. In this phase, the process is governed by the crushing failure of the central cross section. In the second phase, between steps 17 and 25, the arch shows a pseudo-plastic plateau which corresponds to a distributed process of damage over different cross sections.

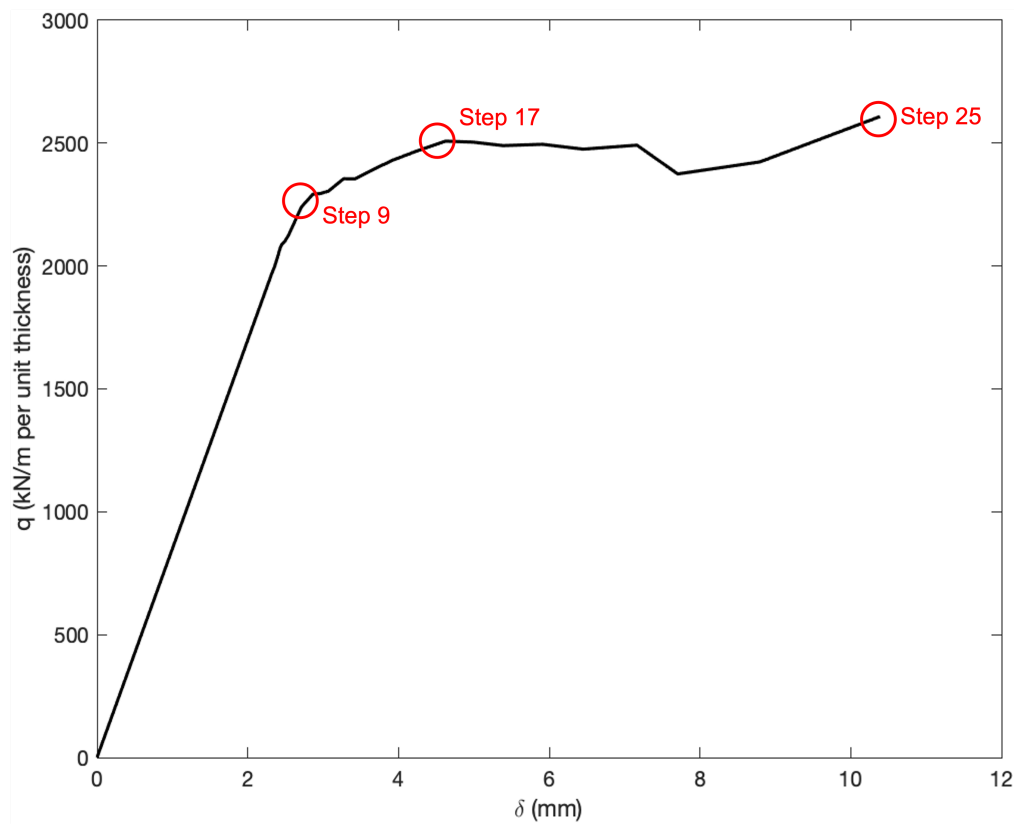


Figure 7.6: Load-displacement curve of the small scale arch.

In these steps it is possible to evaluate the pattern of the axial force,  $N$ , and the bending moment,  $M$ , to study the arch thrust lines, which are shown in Figures 7.7 - 7.8 - 7.9.

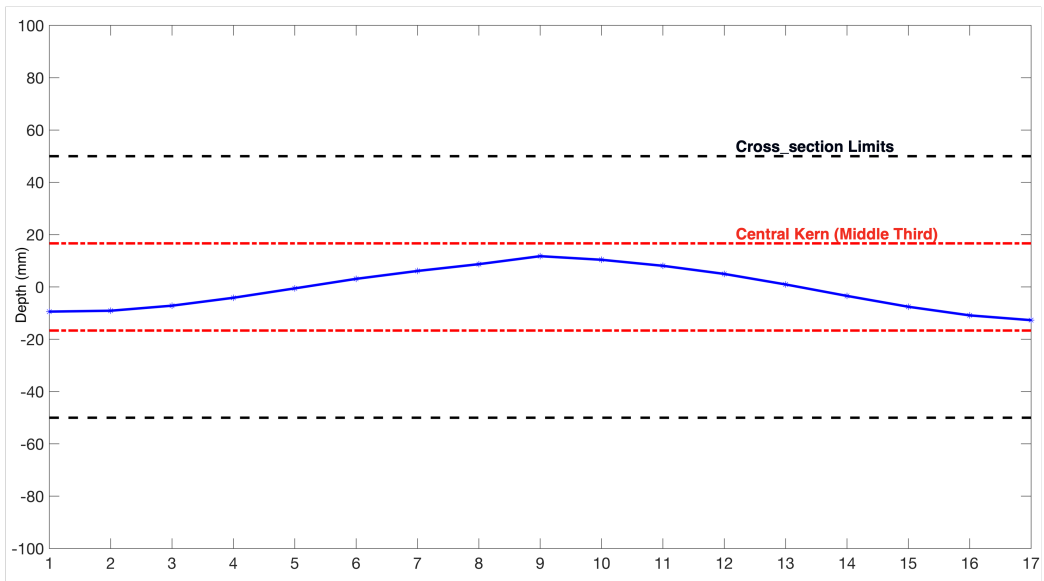


Figure 7.7: Thrust line of the small scale arch for the 17 sections, step 9.

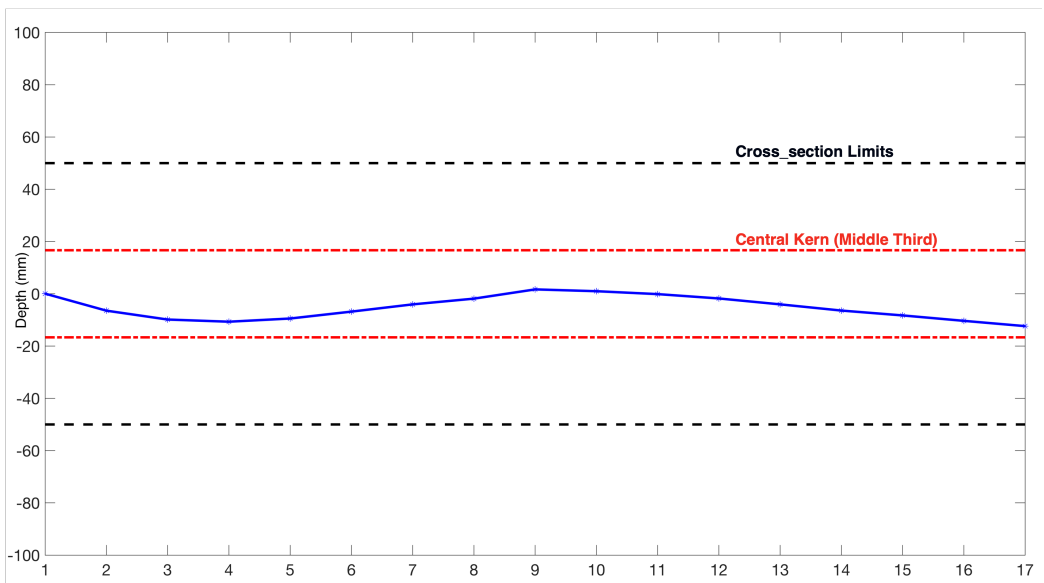


Figure 7.8: Thrust line of the small scale arch for the 17 sections, step 17.

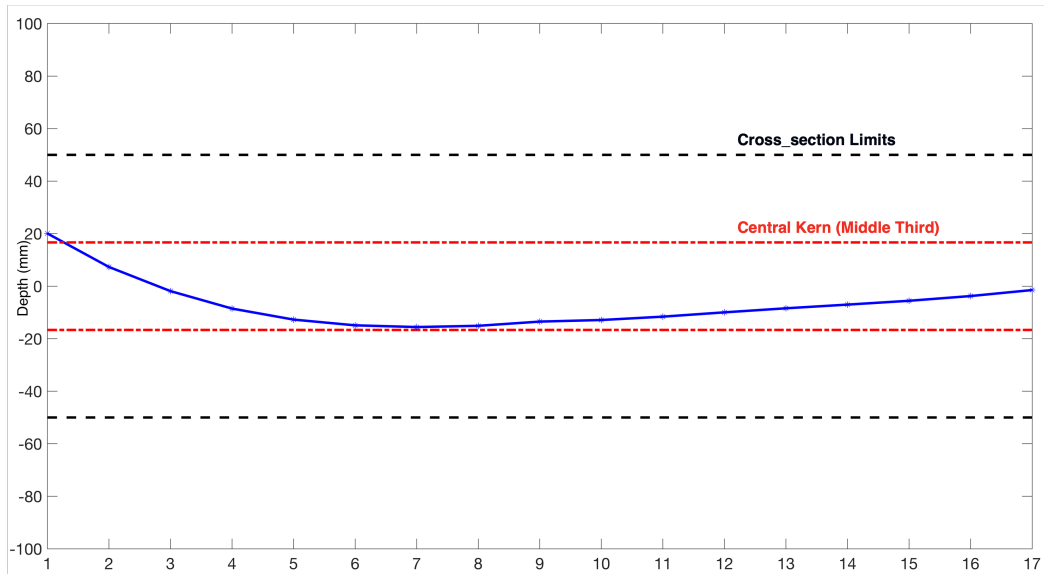


Figure 7.9: Thrust line of the small scale arch for the 17 sections, step 25.

The thrust lines show that the arch at the initial steps is purely subjected to compression, with crushing in section 9 ( Figure 7.7). Subsequently, the thrust line is subjected to a recentering, as the eccentricity is reduced for the central section. However, there is an increase in eccentricity for the side sections, which are subject to damage in the pseudo-plastic plateau phase (Figure 7.9).

The medium scale arch model shows similar results, which are shown in Figure 7.10 in terms of the load-displacement curve and in Figures 7.11 - 7.12 - 7.13 in terms of thrust lines.

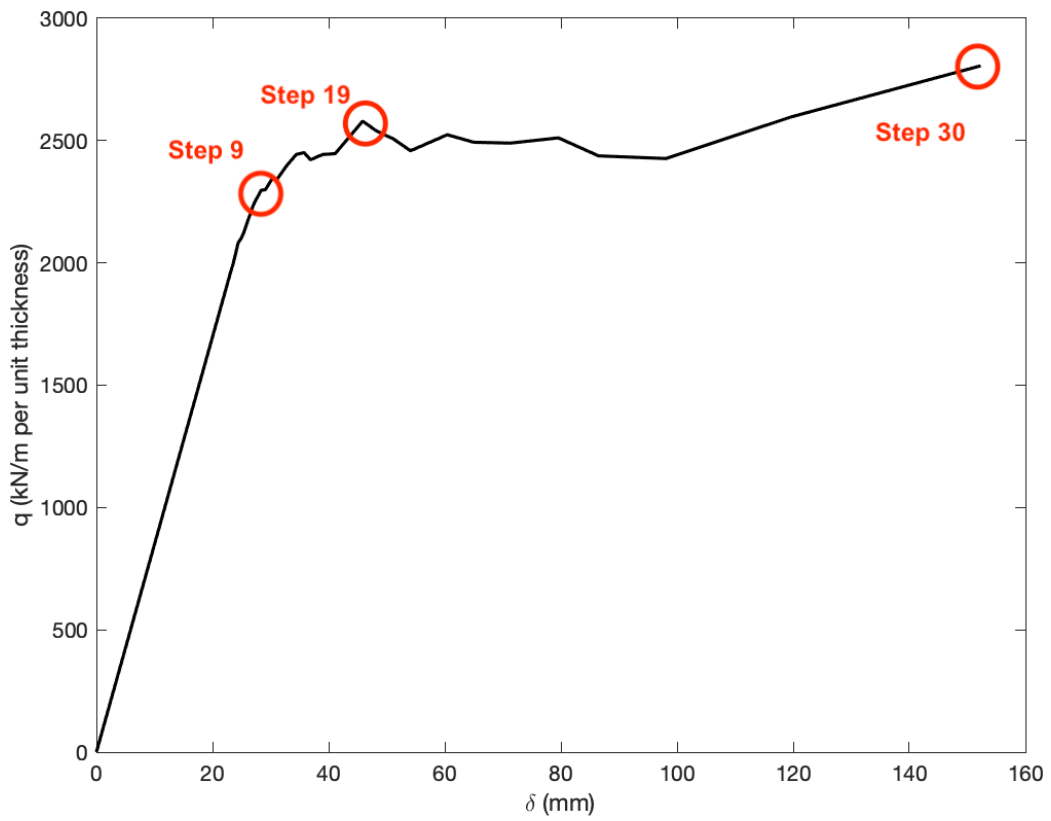


Figure 7.10: Load-displacement curve of the small scale arch.

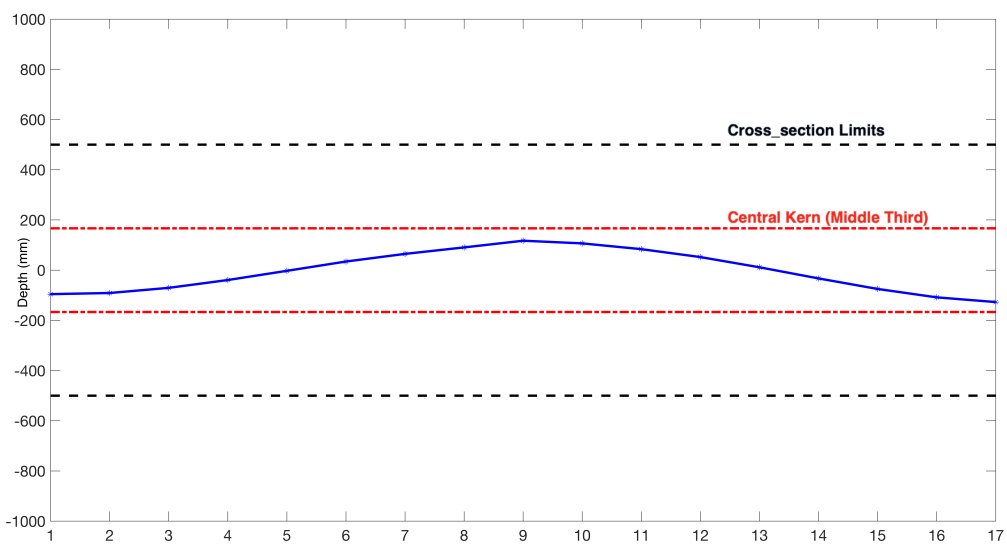


Figure 7.11: Thrust line of the medium scale arch for the 17 sections, step 9.

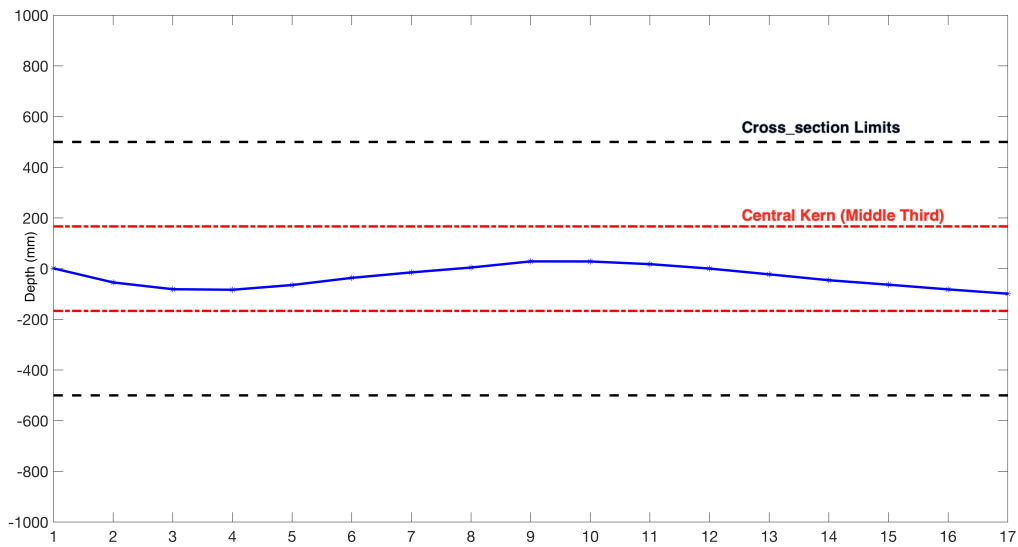


Figure 7.12: Thrust line of the medium scale arch for the 17 sections, step 19.

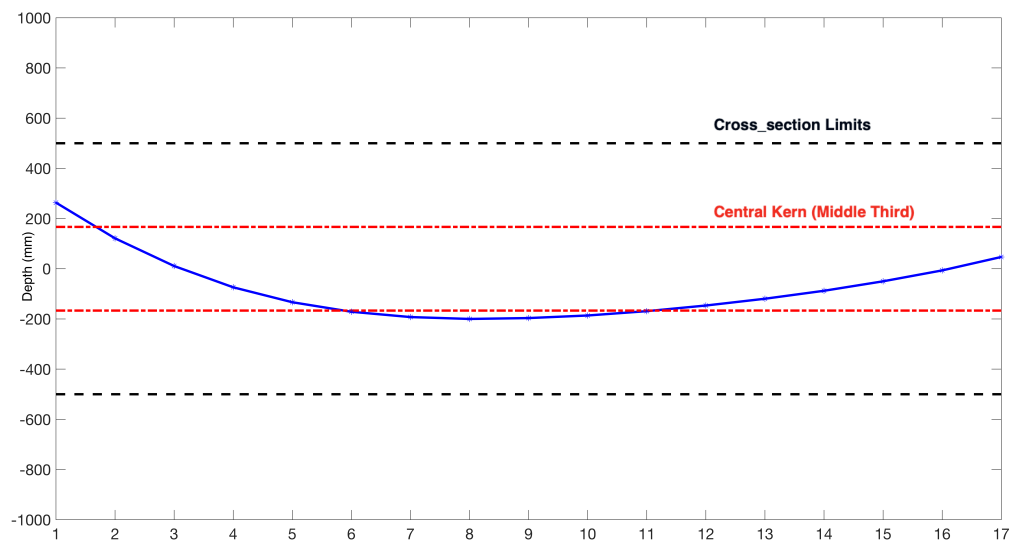


Figure 7.13: Thrust line of the medium scale arch for the 17 sections, step 30.

The results of the large scale arch model are analysed through four significant steps (Figure 7.14). Step 6 identifies the load peak value at the end of the

elastic brach, which occurs due to the initiation of the overlapping failure in the central cross section (9). Between steps 6 and 12, crushing occurs in the three central cross sections (8-9-10), and in step 12, there is the initiation of a crack in section 9, which propagates until a hinge is generated. In the last steps, the damage process develops with the formation of cracks at the extrados of the arch. However, it globally remains more limited to just the middle sections.

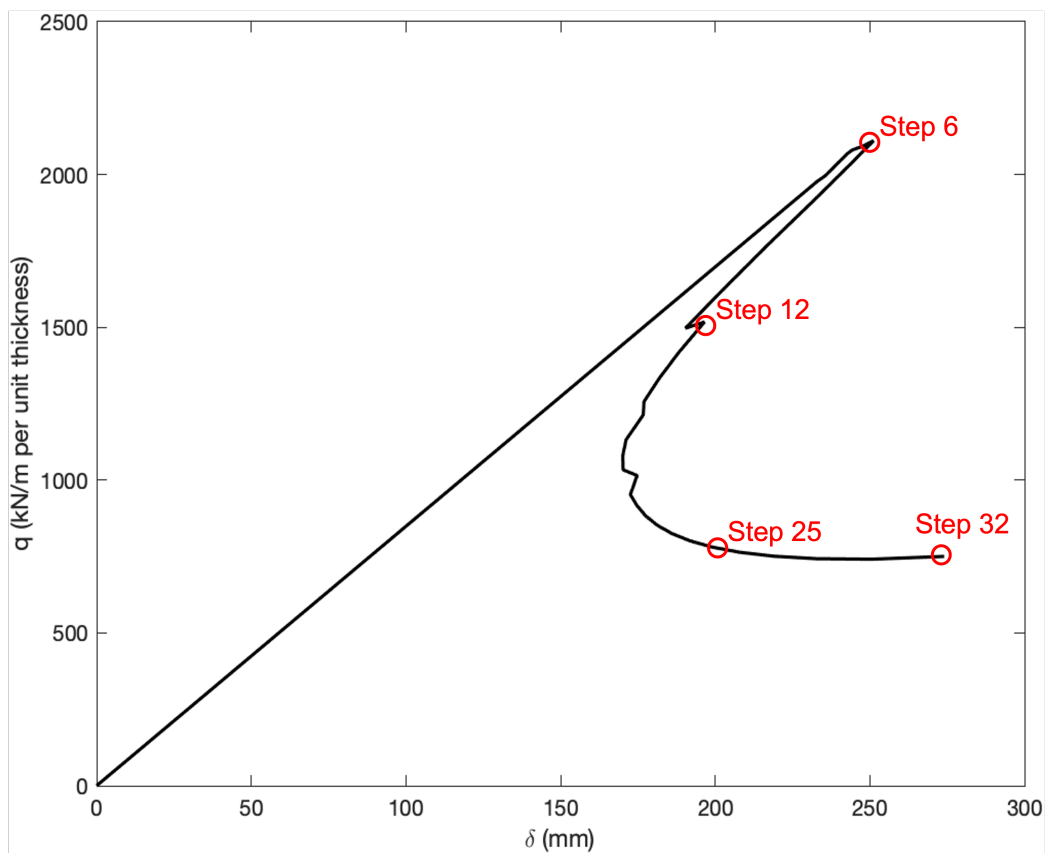


Figure 7.14: Load-displacement curve of the small scale arch.

As shown by the thrust lines (Figures 7.15 - 7.16 - 7.17), the recentering effect between steps 6 and 25 is less evident, if compared to the other arches. In addition, the cracking failure in the last step is highlighted by the thrust line, which exceeds the limit of the middle third of the cross section (Figure 7.18).

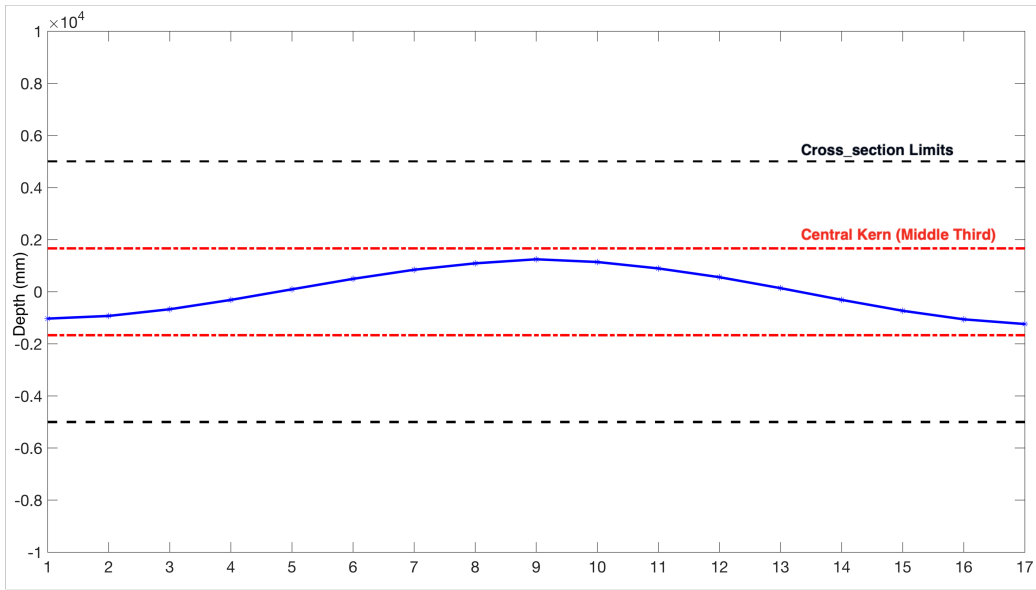


Figure 7.15: Thrust line of the large scale arch for the 17 sections, step 6.

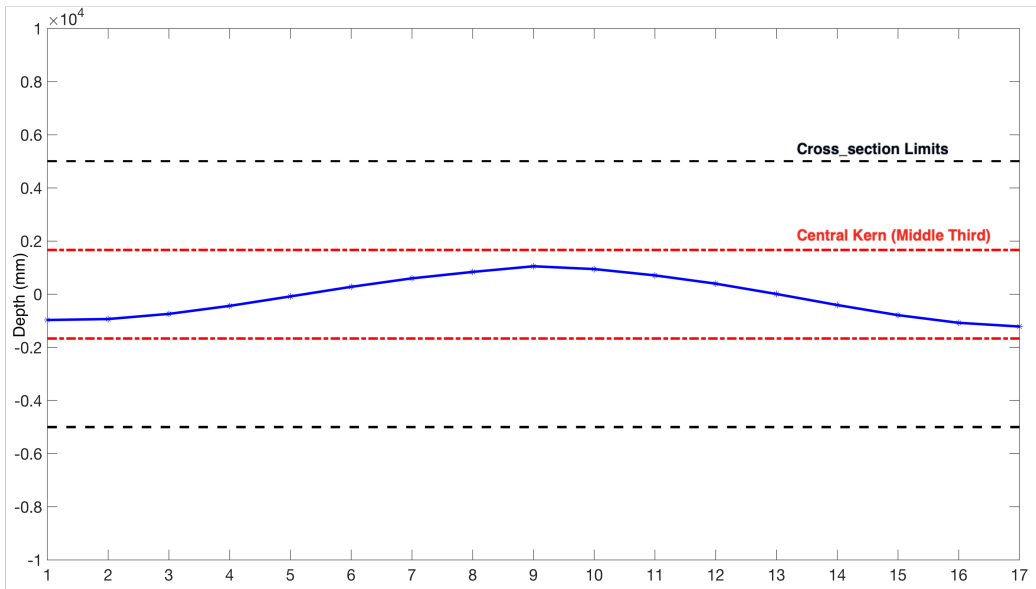


Figure 7.16: Thrust line of the large scale arch for the 17 sections, step 12.

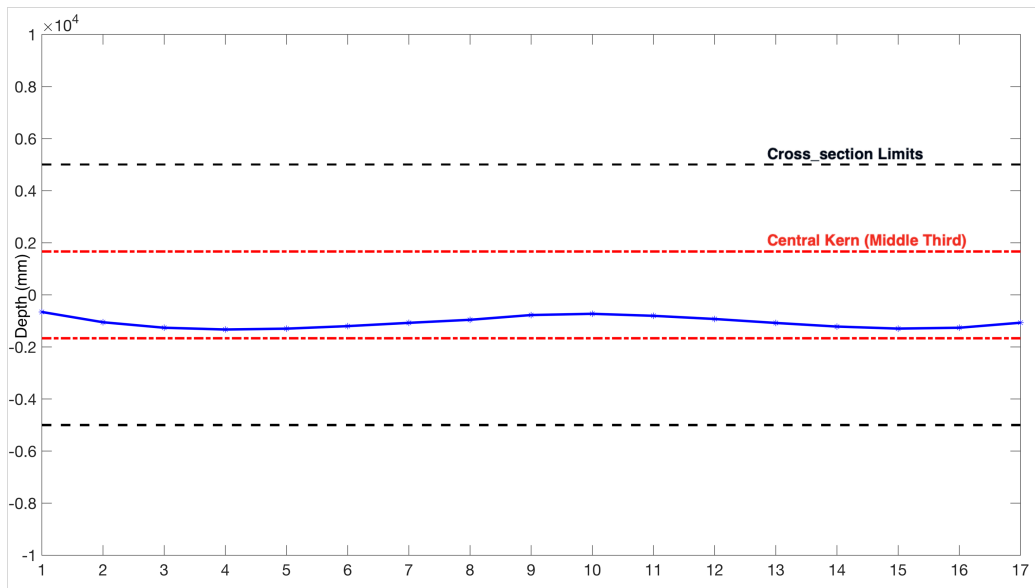


Figure 7.17: Thrust line of the large scale arch for the 17 sections, step 25.

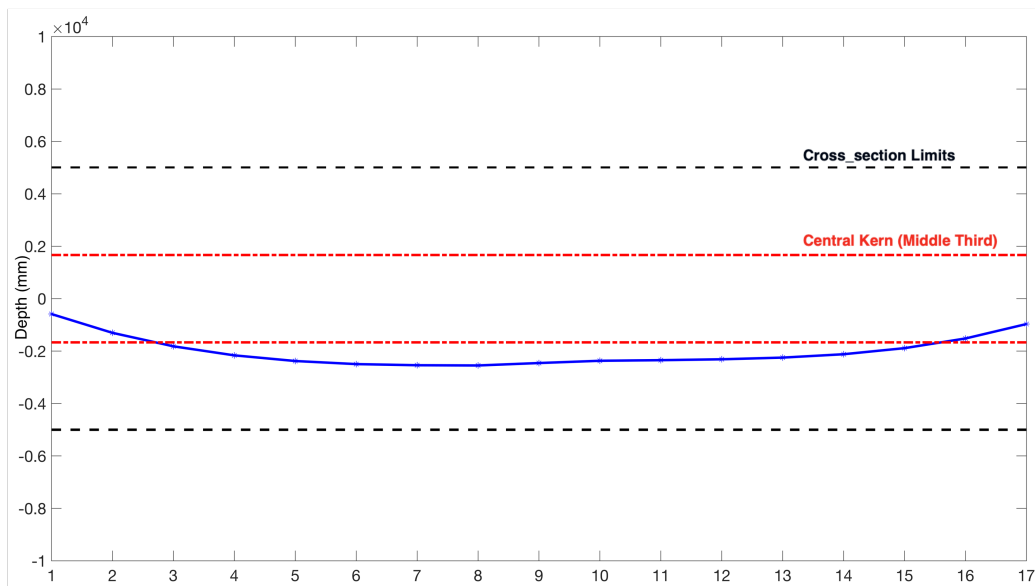


Figure 7.18: Thrust line of the large scale arch for the 17 sections, step 32.

### 7.3 The Mosca bridge case study

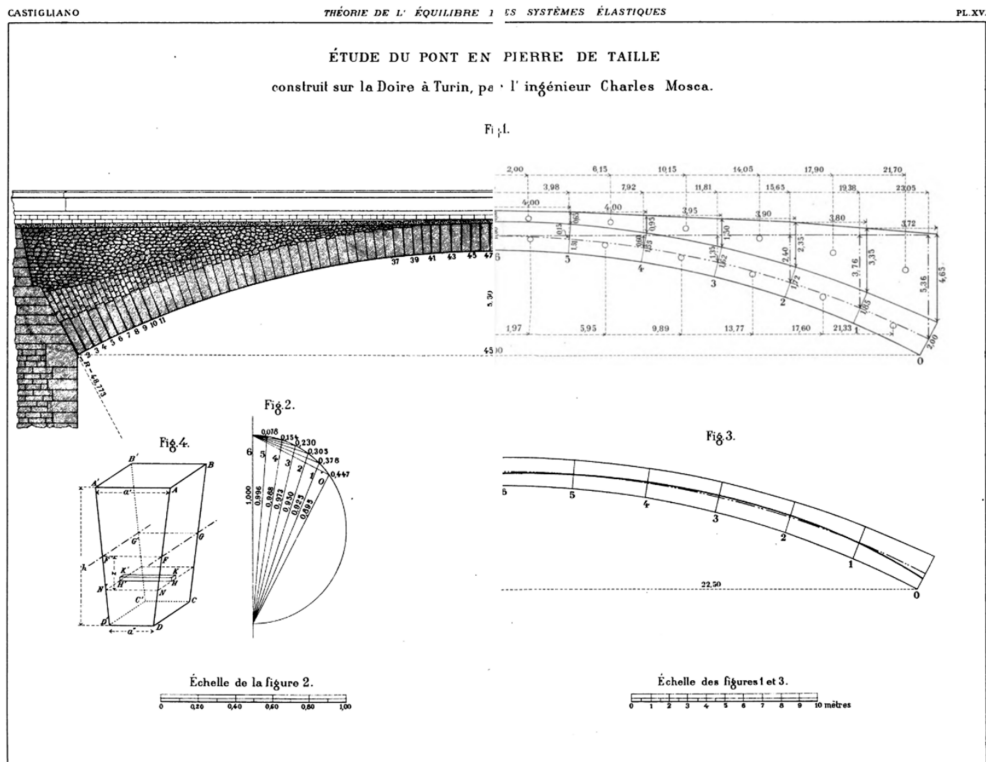
The following case study refers to the Mosca bridge, located in Turin, Italy (Figure 7.19). The Mosca bridge is the most daring construction built in Turin in the first half of the XIXth century. The total length of the arch bridge is 129 m, and its width is 13.7 m. The principal structure, entirely cut in stone, is a single shallow arch with a span of 45 m, a rise of 5.5 m, and a depth that goes from 2.0 m, at the abutments, to 1.5 m at the keystone. Therefore, the arch structure shallowness ratio is approximately 1 : 8, and its slenderness ratio is approximately 1 : 30. The structural material of the arch is Melanaggio stone, a greenish-grey gneiss with mechanical characteristics similar to those of granite.

The model of the Mosca bridge follows a circular shape with the abovementioned values of length and rise. The depth is modelled as linearly varying between the abutment and the keystone. The external constraints are two rigidly fixed joints at the abutments, and the external variable load is uniformly distributed along the length ( $\hat{f}$ ). The mesh is subdivided by means of 17 cross sections, in which the opening of cracks and the crushing failure can be simulated.

The analysis firstly considers the effects of the permanent loads given by the arch self-weight and the effect of the filling. The assumed value of density for the Manalaggio Granite is 27 kN/m<sup>3</sup>, while the density of the filling is 23 kN/m<sup>3</sup>. These actions are represented by a parabolic load distribution, in which amplitude can be incremented until the total permanent loads are applied. From this analysis, it is possible to assess the formation of a symmetric crack pattern at the springings, which arises due to the application of permanent loads only. The value of ( $\hat{f}$ ) is updated through the load factor,  $\lambda$ , from the initial value, ( $\hat{f}_0$ ).



(a)



(b)

Figure 7.19: Mosca bridge, Turin (Italy): Overview, [33] (a); Arch sketch by Alberto Castigliano, 1879, [87] (b).

After the application of the permanent loads, the stress reaches the ultimate tensile value at the springings, at the extrados of the arch (Figure 7.20). At this level of load, there is the initiation of two symmetric cracks, as shown in Figure 7.21 and in the detail of Figure 7.22

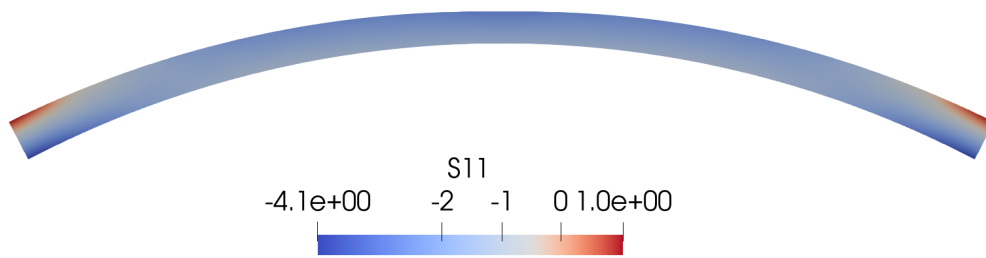


Figure 7.20: Stress distribution in Mosca bridge after the application of the permanent loads, from ParaView.

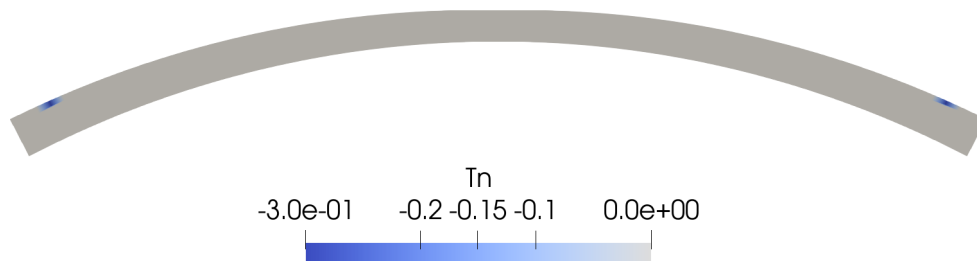


Figure 7.21: Distribution of tensions at the crack interfaces in Mosca bridge after the application of the permanent loads, from ParaView.

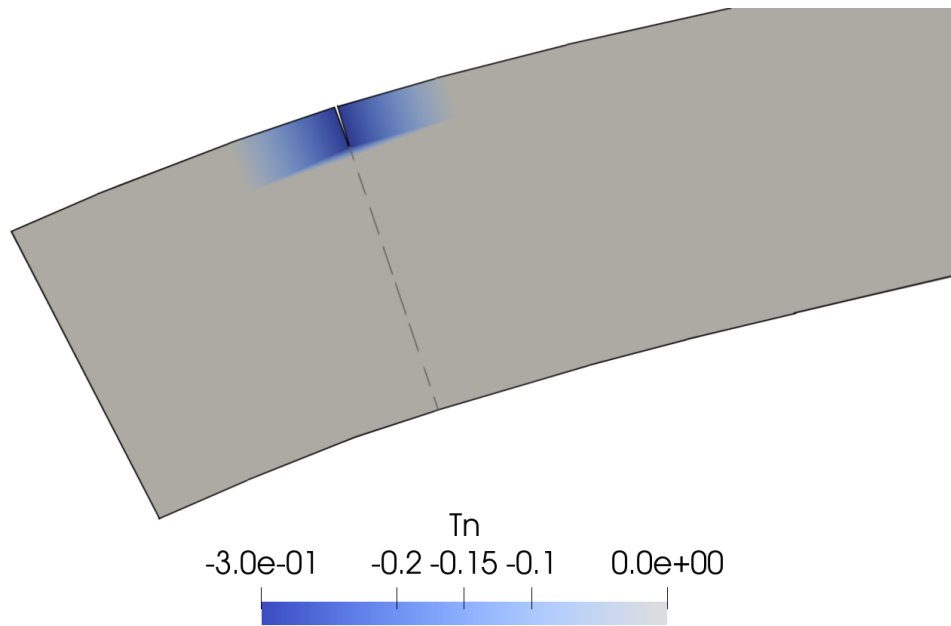


Figure 7.22: Detail of Mosca bridge springings with the crack process zone after the application of the permanent loads. Deformed configuration from ParaView.

The cohesive process zone at the bridge lateral cross section can grow for low values of variable loads (6 kN/m per unit thickness), in agreement with the analysis performed by Castigliano [87]. However, for higher values of variable loads, the fracturing processes presents a crack closure, and the arch remains stable until a crushing failure occurs. The principal result of the analysis is given in terms of the load-displacement diagram (Figure 7.23). It shows a maximum live load of  $q_{\text{live}} = 1030$  kN/m per unit thickness. As, from elastic analysis, the arch is subjected to cracks with  $q_{\text{live}} = 0$  kN/m, the "*fracturing benefit*" is equal to  $q_{\text{live}} = 1030$  kN/m. This result is higher than the one evaluated with the linear elastic fracture mechanics approach ( $q_{\text{live}} = 870$  kN/m), but it is lower than the "*plastic benefit*" of 1190 kN/m given by the limit analysis [33].

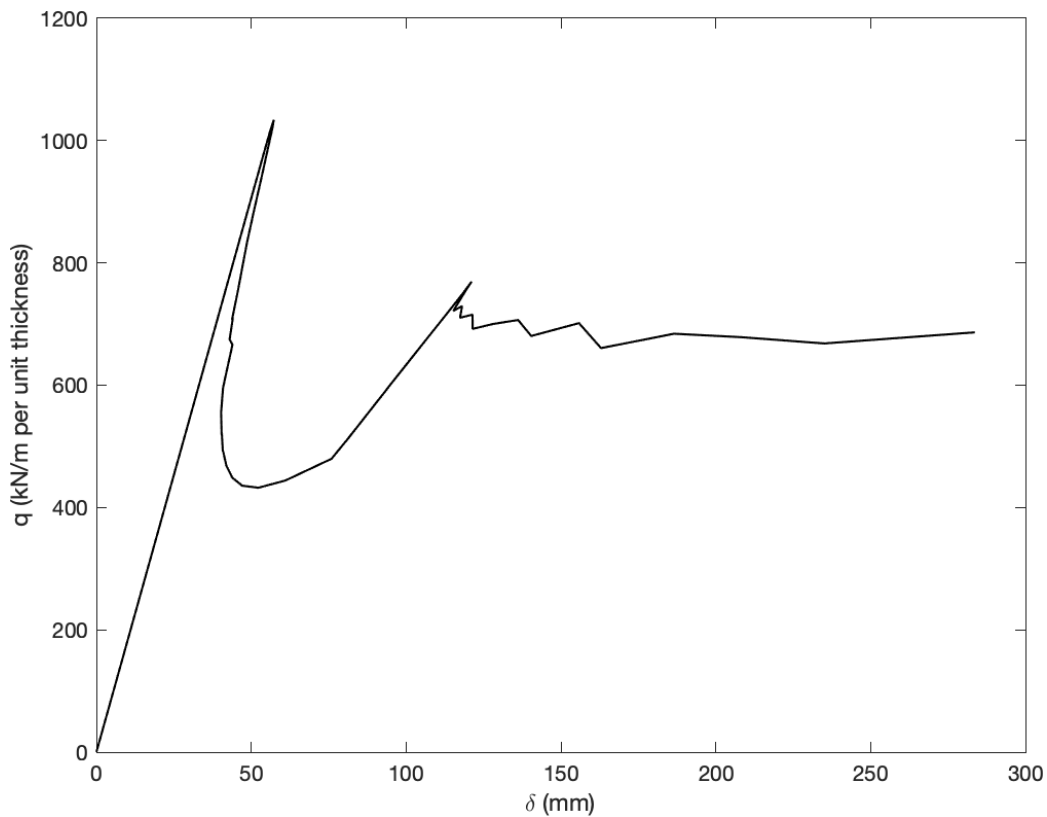


Figure 7.23: Load-Displacement curve for the keystone node of Mosca Bridge in vertical direction.

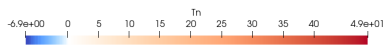
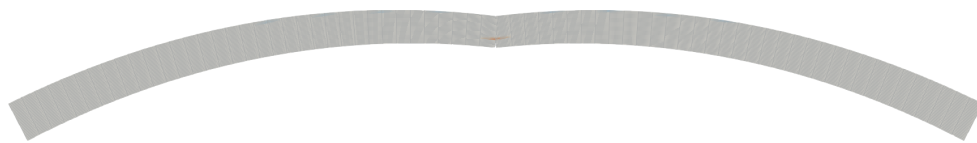
From Figure 7.23, it is possible to identify a first elastic branch, until the arch reaches the peak distributed load, a softening branch, in which a snap-back instability is present, a load resumption and a final branch which represents a pseudo-plastic plateau until the arch reaches the ultimate displacement. Some local instabilities (local snap-backs) are visible as well, especially in the final branch. By modifying the mesh, increasing the number of nodes, the global snap-back tends to become more detailed, highlighting the local instabilities. The output listing shows that the snap-back is governed by the crushing failure in the central cross section (section 9) in steps 1-25 (Figures 7.24-7.25 ). Instead, after the global snap-back, the arch is subjected to a more diffused failure process, in which both crushing and cracking occur (Figure 7.26).



(a) *Step 5.*



(b) *Step 20.*



(c) *Step 30.*

Figure 7.24: Mosca bridge, representation of the arch model in the FEM framework in the deformed configuration with the interface tensions, from ParaView.

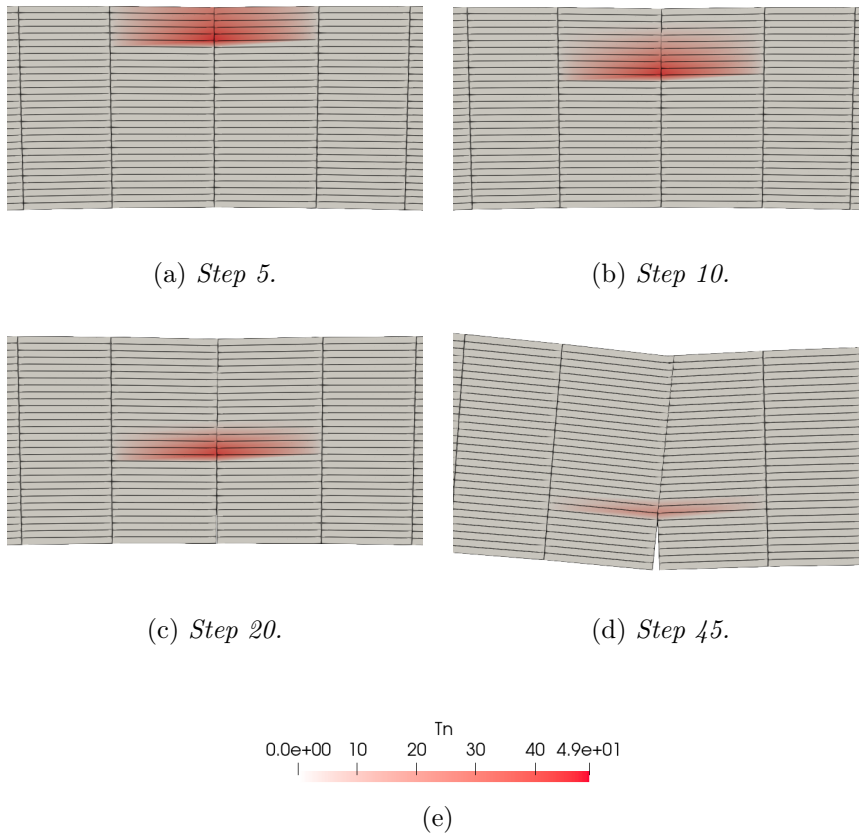


Figure 7.25: Mosca bridge, detail of the keystone cross section in the deformed configuration with the interface tensions, from ParaView.

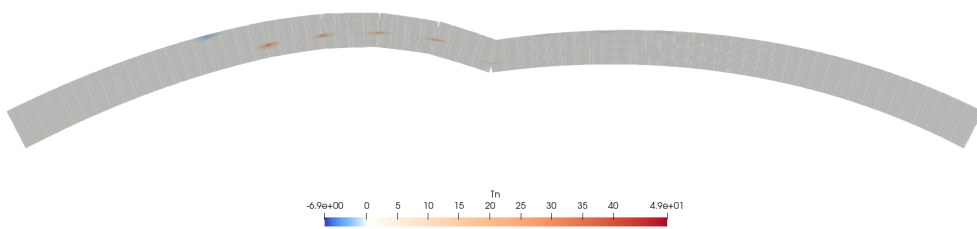


Figure 7.26: Mosca bridge, representation of the arch model in the FEM framework at step 45, in the deformed configuration with the interface tensions, from ParaView.

Adopting PyFEM output writer and *OutputDiagrams.py*, for each analysis step, the thrust lines can be represented as well as the diagrams of axial force and bending moment. In this case study, four significant steps are identified, as shown in Figure 7.27, and for each one the thrust line is presented to highlight the process of crushing that occurs after the peak load and the damage process that subsequently arise in the lateral cross sections (Figures 7.28 - 7.29 - 7.30 - 7.31).

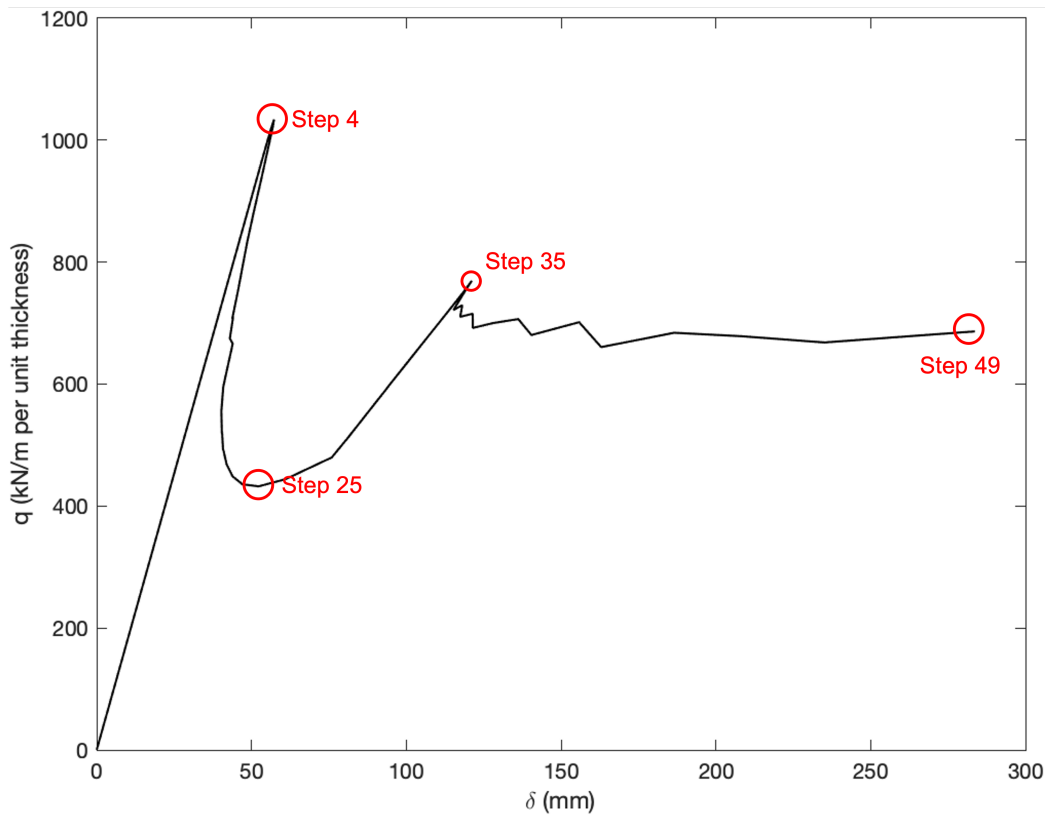


Figure 7.27: Load-Displacement curve for the keystone node of Mosca Bridge in vertical direction. Identification of the steps for the representation of the thrust lines.

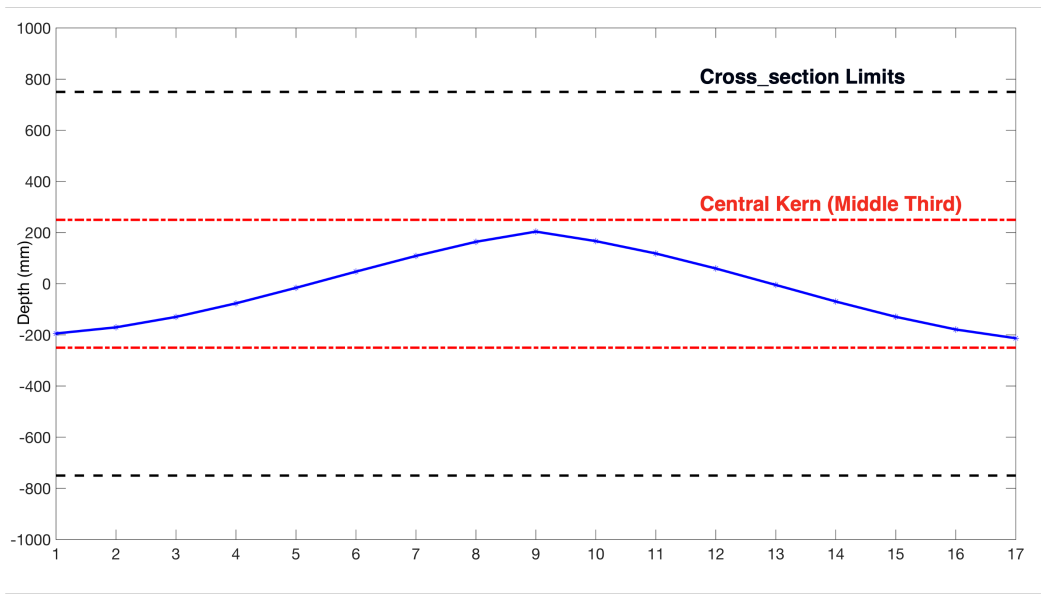


Figure 7.28: Thrust line of the Mosca bridge for the 17 sections, step 4.

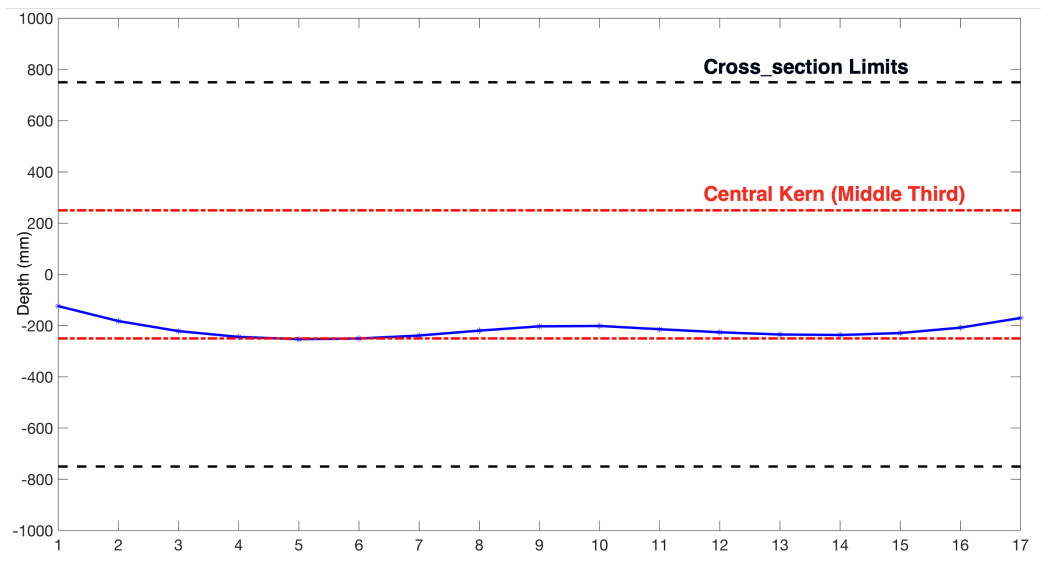


Figure 7.29: Thrust line of the Mosca bridge for the 17 sections, step 25.

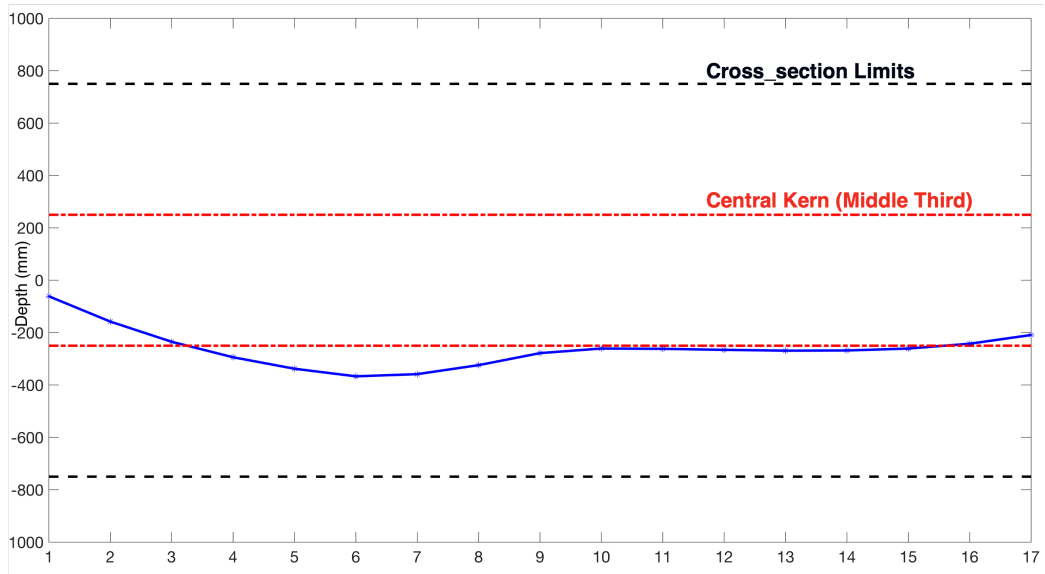


Figure 7.30: Thrust line of the Mosca bridge for the 17 sections, step 35.

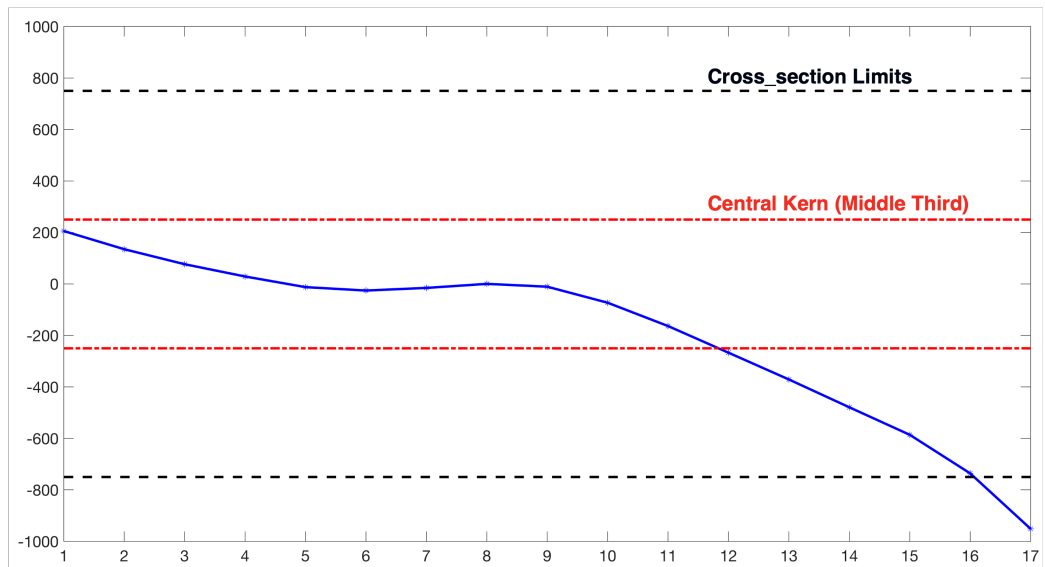


Figure 7.31: Thrust line of the Mosca bridge for the 17 sections, step 49.

The analysis of the Mosca bridge is reiterated with a modification of the mechanical parameters. In particular, the constitutive laws are updated by introducing the average characteristics of concrete, as shown in Section 7.1. The load-displacement curve is presented in Figure 7.32. It shows the variable

load with the same global behaviour given in Figure 7.23, therefore, the effect of material properties is lower if compared to the effect of arch shape.

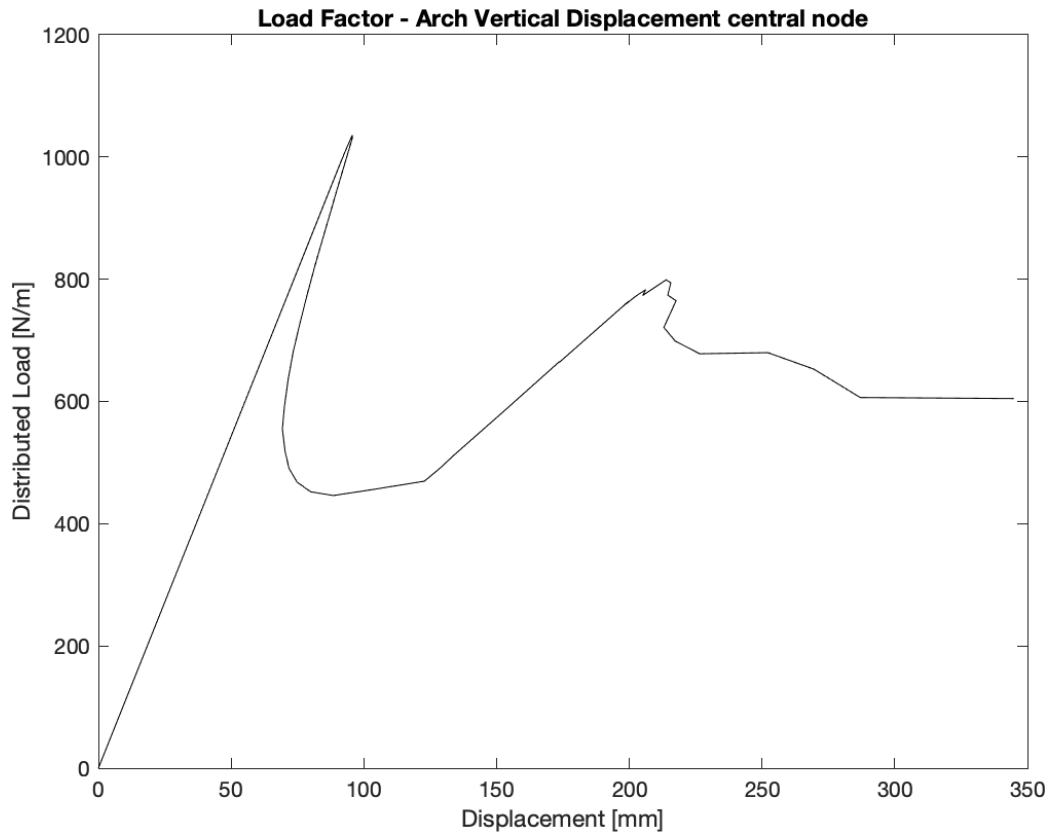


Figure 7.32: Load-Displacement curve for the keystone node of Mosca Bridge in vertical direction, with concrete mechanical properties.

# Chapter 8

## Conclusions

The present work proposes an algorithm for arches analysis, showing the potentiality of the cohesive/overlapping crack model to perform their elasto-plastic-softening evolutionary analysis, describing their non-linear response due to crushing and cracking failure. The algorithm is formulated in the FEM framework, exploiting the introduction of zero-thickness elements to update the mesh and simulate the cohesive process zone as well as the overlapping one.

In agreement with the linear elastic fracture mechanics-based procedure, it is possible to determine the maximum admissible live load and to compare it with the load predicted by elasticity theory, studying the *fracturing benefit*. Furthermore, the whole load-displacement response can be evaluated, and the scale effects can be highlighted.

The aforementioned non-linear fracture mechanics-based method allows studying the effects of off-centre compression on masonry structures. This compressive stress state leads to a prevalent crushing failure for high levels of live loads. It also leads to an internal stress redistribution, detectable from the analysis of the arch thrust line, in which a re-centring trend occurs after crack formation.

It is interesting to note that the curvature effect is of primary importance on the overall arch behaviour. It acts similarly to the effects given by the reinforcement in reinforced concrete elements. Therefore, this tendency may be analysed by adopting the algorithm on different arch models realised as

the shallowness ratio varies.

The current version of the algorithm only considers a Mode I failure. Consequently, it may be generalised to acknowledge the effects of Mode II failure and realise a more comprehensive analysis of arches collapse mechanisms. However, the application of the cohesive/overlapping model for masonry arches requires the knowledge of the fracture properties of materials, i.e. the fracture energy,  $G_F$ , and the crushing energy,  $G_C$ , which are rarely evaluated in experimental studies, so, further investigation is required.

# List of Figures

1.1	Poleni’s drawing of his analysis of the Dome of St. Peter’s in Rome, [14]. . . . .	4
1.2	Stirling’s arched assembly of smooth spheres with the profile of an inverted catenary and Poleni’s slicing of a dome into arched lunes, [14]. . . . .	5
1.3	Four Hinges arch-collapse mechanism, [4]. . . . .	7
1.4	Arch segment subjected to off-centre Compression, [33]. . . . .	9
1.5	Snap-Through Instability for off-centre Compression ( $h=b$ ), [6].	11
1.6	Crack closure curve, [6]. . . . .	12
1.7	Scale effects in masonry arch structures: Dimensionless load of brittle crack propagation versus normalised crack depth, $\xi$ , for $e/h = 0.15$ (a); $e/h = 0.20$ (b); $e/h = 0.35$ (c), [33]. . . . .	14
2.1	Representation of the plastic zone on a crack according to Dugdale model [48] , from Carpinteri, Advanced Structural Mechanics, [49]. . . . .	18
2.2	Developing of the macrocrack, still partially sutured by inclusions, aggregates, or fibres (a); $\sigma - w$ law (b), from Carpinteri, Advanced Structural Mechanics, [49]. . . . .	19
2.3	Simplified Cohesive Crack Model relationship, [52]. . . . .	20
2.4	Loading process of a specimen, fixed at the base and subjected to tensile stress, [53]. . . . .	21
2.5	Post peak stress-displacement response, [54]. . . . .	23
2.6	Potential fracture line: physical and numerical schemes, from Carpinteri algorithm, [10]. . . . .	25
2.7	Three Point Bending Test with Carpinteri algorithm, [55]. . .	27

3.1	Compressive stress-strain relationship, with an ascending stress-strain curve and a descending stress-deformation curve, [56]. . . . .	30
3.2	Overlapping Crack Model relationship, [7]. . . . .	32
3.3	Estimation of the localised interpenetration, $w^c$ , from the total shortening of the specimen, $\delta$ , [65]. . . . .	33
3.4	Simplified Overlapping Crack Model relationship, [52]. . . . .	33
3.5	The loading process of a uniaxial compression test, [65]. . . . .	34
3.6	Stress-displacement response in compression, [62]. . . . .	35
4.1	Tensile fracture with cohesive zone and compressive crushing with overlapping, [52]. . . . .	37
4.2	Cohesive/Overlapping Crack Model, finite nodes position in the numerical algorithm, [63]. . . . .	38
4.3	Cohesive/Overlapping Crack Model, force distribution according to the numerical algorithm, [67]. . . . .	39
4.4	Steel-concrete interaction, [67]. . . . .	41
4.5	Steel constitutive law, [67]. . . . .	42
5.1	Finite Element idealisation with cracks according to Ngo and Scordelis, [78]. . . . .	46
5.2	Linkage element from Ngo and Scordelis, [78]. . . . .	46
5.3	Finite Element mesh with a crack, [79]. . . . .	47
5.4	Discretisation of a generic domain with continuum elements and zero-thickness interface elements, [84]. . . . .	48
5.5	Scheme of a generic body subjected to crack opening and crushing. . . . .	50
5.6	Scheme of an interface element. . . . .	52
6.1	Example 2D linear triangular finite element mesh, in which the regions are identified by capital letters, the elements are identified by lowercase letters and the nodes are identified by numbers, [83]. . . . .	61
7.1	Comparison between the Load-Displacement curves for the keystone node of the three arch scales, with a dense mesh. . . . .	67

7.2	Comparison between the Load-Displacement curves for the keystone node of the three arch scales, with a less dense mesh.	68
7.3	Comparison between the three arch models in the deformed configuration with the interface tensions, from ParaView. The displacements are subjected to a scaling factor equal to 10. . .	70
7.4	Detail of the keystone cross section in the deformed configuration with the interface tensions at the end of the analysis, from ParaView. The displacements are subjected to a scaling factor equal to 10. . . . .	71
7.5	Detail of the lateral cross sections in the deformed configuration with the interface tensions at the two final steps of the analysis, from ParaView. The displacements are subjected to a scaling factor equal to 10. . . . .	72
7.6	Load-displacement curve of the small scale arch. . . . .	73
7.7	Thrust line of the small scale arch for the 17 sections, step 9. .	74
7.8	Thrust line of the small scale arch for the 17 sections, step 17.	74
7.9	Thrust line of the small scale arch for the 17 sections, step 25.	75
7.10	Load-displacement curve of the small scale arch. . . . .	76
7.11	Thrust line of the medium scale arch for the 17 sections, step 9.	76
7.12	Thrust line of the medium scale arch for the 17 sections, step 19. . . . .	77
7.13	Thrust line of the medium scale arch for the 17 sections, step 30. . . . .	77
7.14	Load-displacement curve of the small scale arch. . . . .	78
7.15	Thrust line of the large scale arch for the 17 sections, step 6. .	79
7.16	Thrust line of the large scale arch for the 17 sections, step 12.	79
7.17	Thrust line of the large scale arch for the 17 sections, step 25.	80
7.18	Thrust line of the large scale arch for the 17 sections, step 32.	80
7.19	Mosca bridge, Turin (Italy): Overview, [33] (a); Arch sketch by Alberto Castigliano, 1879, [87] (b). . . . .	82
7.20	Stress distribution in Mosca bridge after the application of the permanent loads, from ParaView. . . . .	83
7.21	Distribution of tensions at the crack interfaces in Mosca bridge after the application of the permanent loads, from ParaView. .	83

7.22	Detail of Mosca bridge springings with the crack process zone after the application of the permanent loads. Deformed configuration from ParaView. . . . .	84
7.23	Load-Displacement curve for the keystone node of Mosca Bridge in vertical direction. . . . .	85
7.24	Mosca bridge, representation of the arch model in the FEM framework in the deformed configuration with the interface tensions, from ParaView. . . . .	86
7.25	Mosca bridge, detail of the keystone cross section in the deformed configuration with the interface tensions, from ParaView.	87
7.26	Mosca bridge, representation of the arch model in the FEM framework at step 45, in the deformed configuration with the interface tensions, from ParaView. . . . .	87
7.27	Load-Displacement curve for the keystone node of Mosca Bridge in vertical direction. Identification of the steps for the representation of the thrust lines. . . . .	88
7.28	Thrust line of the Mosca bridge for the 17 sections, step 4. . .	89
7.29	Thrust line of the Mosca bridge for the 17 sections, step 25. . .	89
7.30	Thrust line of the Mosca bridge for the 17 sections, step 35. . .	90
7.31	Thrust line of the Mosca bridge for the 17 sections, step 49. . .	90
7.32	Load-Displacement curve for the keystone node of Mosca Bridge in vertical direction, with concrete mechanical properties. . .	91

# Bibliography

- <sup>1</sup>E. Méry, ‘Sur l’équilibre des voûtes en berceau’, in *Annales des ponts et chaussées*, Vol. 19 (1840), pp. 50–70.
- <sup>2</sup>C. Navier, *Resume des lecons donnees a l’ecole des ponts et chaussees sur l’application de la mecanique a l’etablissement des constructions et des machines par navier* (Societe Belge de librairie, 1839).
- <sup>3</sup>J. Heyman, ‘The stone skeleton’, in *International journal of solids and structures*, Vol. 2, 2 (Elsevier, 1966), pp. 249–279.
- <sup>4</sup>J. Heyman, *The masonry arch* (1982).
- <sup>5</sup>J. Heyman, *Structural analysis: a historical approach* (Cambridge University Press, 1998).
- <sup>6</sup>A. Carpinteri, G. Lacidogna, and F. Accornero, ‘Evolution of the fracturing process in masonry arches’, in *Journal of structural engineering*, Vol. 141, 5 (2015).
- <sup>7</sup>A. Carpinteri, M. Corrado, M. Paggi, and G. Mancini, ‘Cohesive versus overlapping crack model for a size effect analysis of rc elements in bending’, in *Proceedings of framcos-6* (2007), pp. 655–663.
- <sup>8</sup>M. Corrado, ‘Effetti di scala sulla capacità di rotazione plastica di travi in calcestruzzo armato’, PhD Thesis (PhD thesis, Politecnico di Torino, 2007).
- <sup>9</sup>A. Carpinteri, *Interpretation of the griffith instability as a bifurcation of the global equilibrium. in application of fracture mechanics to cementitious composites* (Springer, 1985), pp. 287–316.

- <sup>10</sup>A. Carpinteri, ‘Cusp catastrophe interpretation of fracture instability’, in *Journal of the mechanics and physics of solids*, Vol. 37, 5 (1989), pp. 567–582.
- <sup>11</sup>A. Carpinteri and G. Colombo, ‘Numerical analysis of catastrophic softening behaviour (snap-back instability)’, in *Computers & structures*, Vol. 31, 4 (Elsevier, 1989), pp. 607–636.
- <sup>12</sup>V. Pollio, *De architectura* (Harvard University Press, Cambridge, MA, 1914).
- <sup>13</sup>B. A. Vittone, G. Guarini, G. C. Bianchi, N. Dallamano, G. Le Poer, F. Peyrolery, M. L. Quarini, and F. Ripa, *Istruzioni diverse concernenti l’ufficio dell’architetto civile, ed inservienti d’elucidazione ed aumento alle istruzioni elementari d’architettura, già al pubblico consegnate: ove si tratta della misura delle fabbriche, del moto, e della misura delle acque correnti, dell’estimo de’beni, del miglio comune d’italia, dei ponti, e di pressoche ogni sorta di fabbriche, ed ornamenti d’architettura civile: divise in libri due e dedicate alla gran vergine e madre di dio maria santissima* (Per gli Agnelli e Comp., 1766).
- <sup>14</sup>G. Poleni, *Memorie istoriche della gran cupola del tempio vaticano, e de’danni di essa, e de’ristoramenti loro, divise in libri cinque* (Nella Stamperia del seminario, 1748).
- <sup>15</sup>T. Ruddock and E. Ruddock, *Arch bridges and their builders 1735-1835* (Cambridge University Press, 1979).
- <sup>16</sup>P. Block, ‘Equilibrium systems: studies in masonry structure’, PhD thesis (Massachusetts Institute of Technology, 2005).
- <sup>17</sup>P. Block, M. DeJong, and J. Ochsendorf, ‘As hangs the flexible line: equilibrium of masonry arches’, in *Nexus network journal*, Vol. 8, 2 (Springer, 2006), pp. 13–24.
- <sup>18</sup>P. Block, T. Ciblac, and J. Ochsendorf, ‘Real-time limit analysis of vaulted masonry buildings’, in *Computers & structures*, Vol. 84, 29-30 (Elsevier, 2006), pp. 1841–1852.

- <sup>19</sup>P. de La Hire, *Traité de mécanique, ou l'on explique tout ce qui est nécessaire dans la pratique des arts, & les propriétés des corps pesans lesquelles ont un plus grand usage dans la physique...* (La Compagnie des libraires, 1729).
- <sup>20</sup>P. Couplet, 'De la poussée des voûtes', in *Histoire de l'académie royale des sciences*, Vol. 79 (1729), p. 117.
- <sup>21</sup>L. Mascheroni, *Nuove ricerche sull'equilibrio delle volte dell'abate lorenzo mascheroni... coll'elogio scritto dal marchese ferdinando landi e con cinque tavole in rame*, Vol. 238 (per Giovanni Silvestri, 1829).
- <sup>22</sup>C. A. Coulomb, 'In memories de mathematique et de physique', in *Academic royal des sciences par divers sans*, Vol. 7 (1773), pp. 343–382.
- <sup>23</sup>F. Accornero, G. Lacidogna, and A. Carpinteri, 'Medieval arch bridges in the lanzo valleys, italy: case studies on incremental structural analysis and fracturing benefit', in *Journal of bridge engineering*, Vol. 23, 7 (2018).
- <sup>24</sup>A. Kooharian, 'Limit analysis of voussoir (segmental) and concrete arches', in *Journal proceedings*, Vol. 49, 12 (1952), pp. 317–328.
- <sup>25</sup>M. Gilbert and C. Melbourne, 'Rigid-block analysis of masonry structures', in *Structural engineer*, Vol. 72, 21 (1994).
- <sup>26</sup>A. W. Hendry, S. Davies, and R. Royles, *Test on stone masonry arch at bridgemill-girvan*, tech. rep. (1985).
- <sup>27</sup>D. O'Dwyer, 'Funicular analysis of masonry vaults', in *Computers & structures*, Vol. 73, 1-5 (Elsevier, 1999), pp. 187–197.
- <sup>28</sup>D. O'Dwyer, 'Limit state analysis of masonry vaults. m. eng. sc', PhD thesis (thesis, University College, Galway, Ireland. 31, 1991).
- <sup>29</sup>M. Crisfield and A. Packham, 'A mechanism program for computing the strength of masonry arch bridges', in *Research report-transport and road research laboratory*, 124 (1987).
- <sup>30</sup>G. Milani and P. B. Lourenço, '3d non-linear behavior of masonry arch bridges', in *Computers & structures*, Vol. 111 (2012), pp. 133–150.

- <sup>31</sup>A. Cavicchi and L. Gambarotta, ‘Lower bound limit analysis of masonry bridges including arch–fill interaction’, in *Engineering structures*, Vol. 29, 11 (2007), pp. 3002–3014.
- <sup>32</sup>F. Accornero, G. Lacidogna, and A. Carpinteri, ‘Evolutionary fracture analysis of masonry arches: effects of shallowness ratio and size scale’, in *Comptes rendus mécanique*, Vol. 344, 9 (2016), pp. 623–630.
- <sup>33</sup>F. Accornero and G. Lacidogna, ‘Safety assessment of masonry arch bridges considering the fracturing benefit’, in *Applied sciences*, Vol. 10, 10 (Multi-disciplinary Digital Publishing Institute, 2020), p. 3490.
- <sup>34</sup>A. Carpinteri and A. Carpinteri, ‘Softening and fracturing process in masonry arches’, in *Proceedings of the 6th international brick masonry conference, rome* (1982), pp. 502–510.
- <sup>35</sup>P. B. Lourenço, ‘Anisotropic softening model for masonry plates and shells’, in *Journal of structural engineering*, Vol. 126, 9 (2000), pp. 1008–1016.
- <sup>36</sup>A. Hillerborg, M. Modéer, and P. Petersson, ‘Analysis of crack formation and crack growth in concrete by means of fracture mechanics and finite elements’, in *Cement and concrete research*, Vol. 6, 6 (1976), pp. 773–781.
- <sup>37</sup>N. Taylor and P. Mallinder, ‘The brittle hinge in masonry arch mechanisms’, in *Structural engineer*, Vol. 71, 20 (1993).
- <sup>38</sup>F. International Union of Railways (UIC) Paris, *Recommendations for the assessment of the load carrying capacity of existing masonry and mass concrete arch bridges*, 1995.
- <sup>39</sup>A. Carpinteri, ‘Stiffness loss and fracture resistance of a cracked beam with circular cross-section’, in *Meccanica*, Vol. 18, 3 (1983), pp. 156–162.
- <sup>40</sup>T. G. Chondros and A. D. Dimarogonas, ‘Vibration of a Cracked Cantilever Beam’, in *Journal of vibration and acoustics*, Vol. 120, 3 (July 1998), pp. 742–746.
- <sup>41</sup>M. Krawczuk, A. Żak, and W. Ostachowicz, ‘Elastic beam finite element with a transverse elasto-plastic crack’, in *Finite elements in analysis and design*, Vol. 34, 1 (2000), pp. 61–73.

- <sup>42</sup>H. Okamura, K. Watanabe, and T. Takano, ‘Deformation and strength of cracked member under bending moment and axial force’, in *Engineering fracture mechanics*, Vol. 7, 3 (1975), pp. 531–539.
- <sup>43</sup>R. Parmeter, ‘A method for calculating the reduction in stress intensity factor due to an elastic foundation’, in *Engineering fracture mechanics*, Vol. 8, 3 (1976), pp. 539–546.
- <sup>44</sup>G. Lacidogna and F. Accornero, ‘Elastic, plastic, fracture analysis of masonry arches: a multi-span bridge case study’, in *Curved and layered structures*, Vol. 5, 1 (2018), pp. 1–9.
- <sup>45</sup>A. Carpinteri, *Nonlinear crack models for nonmetallic materials*, Vol. 71 (Springer Science & Business Media, 2012).
- <sup>46</sup>A. Carpinteri, ‘Stability of fracturing process in rc beams’, in *Journal of structural engineering*, Vol. 110, 3 (American Society of Civil Engineers, 1984), pp. 544–558.
- <sup>47</sup>A. Carpinteri and R. Massabo, ‘Continuous vs discontinuous bridged-crack model for fiber-reinforced materials in flexure’, in *International journal of solids and structures*, Vol. 34, 18 (Elsevier, 1997), pp. 2321–2338.
- <sup>48</sup>D. S. Dugdale, ‘Yielding of steel sheets containing slits’, in *Journal of the mechanics and physics of solids*, Vol. 8, 2 (Elsevier, 1960), pp. 100–104.
- <sup>49</sup>A. Carpinteri, *Structural Mechanics Fundamentals*, English (CRC Press, Boca Raton, FL, USA, Sept. 2013).
- <sup>50</sup>A. Carpinteri, P. Cornetti, F. Barpi, and S. Valente, ‘Cohesive crack model description of ductile to brittle size-scale transition: dimensional analysis vs. renormalization group theory’, in *Engineering fracture mechanics*, Vol. 70, 14 (Elsevier, 2003), pp. 1809–1839.
- <sup>51</sup>P. E. Petersson, ‘Crack growth and development of fracture zones in plain concrete and similar materials’, PhD thesis (Lund University, 1981).
- <sup>52</sup>A. Carpinteri, F. Accornero, and R. Cafarelli, ‘Scale-dependent maximum reinforcement percentage in reinforced concrete beams’, in *Structural concrete* (Wiley Online Library, 2021).

- <sup>53</sup>A. Carpinteri, ‘Snap-back and hyperstrength in lightly reinforced concrete beams’, in *Magazine of concrete research*, Vol. 40, 145 (Thomas Telford Ltd, 1988), pp. 209–215.
- <sup>54</sup>A. Carpinteri, ‘Snap-back and hyperstrength in lightly reinforced concrete beams’, in *Magazine of concrete research*, Vol. 40, 145 (Thomas Telford Ltd, 1988), pp. 209–215.
- <sup>55</sup>A. Carpinteri, *Advanced structural mechanics* (CRC Press, 2017).
- <sup>56</sup>A. Hillerborg, ‘Fracture mechanics concepts applied to moment capacity and rotational capacity of reinforced concrete beams’, in *Engineering fracture mechanics*, Vol. 35, 1-3 (Elsevier, 1990), pp. 233–240.
- <sup>57</sup>A. Carpinteri, F. Ciola, and N. Pugno, ‘Boundary element method for the strain-softening response of quasi-brittle materials in compression’, in *Computers & structures*, Vol. 79, 4 (Elsevier, 2001), pp. 389–401.
- <sup>58</sup>D. C. Jansen and S. P. Shah, ‘Effect of length on compressive strain softening of concrete’, in *Journal of engineering mechanics*, Vol. 123, 1 (American Society of Civil Engineers, 1997), pp. 25–35.
- <sup>59</sup>J. Van Mier, S. Shah, M. Arnaud, J. Balayssac, A. Bascoul, S. Choi, D. Dasenbrock, G. Ferrara, C. French, M. Gobbi, et al., ‘Strain-softening of concrete in uniaxial compression’, in *Materials and structures*, Vol. 30, 4 (Springer, 1997), pp. 195–209.
- <sup>60</sup>M. A. Van Vliet and J. M. Van Mier, ‘Experimental investigation of concrete fracture under uniaxial compression’, in *Mechanics of cohesive-frictional materials: an international journal on experiments, modelling and computation of materials and structures*, Vol. 1, 1 (Wiley Online Library, 1996), pp. 115–127.
- <sup>61</sup>H. Dahl and R. Brincker, ‘Fracture energy of high-strength concrete in compression’, in (Institute of Building Technology Structural Engineering, Aalborg University . . . , 1989).
- <sup>62</sup>A. Carpinteri, M. Corrado, G. Mancini, and M. Paggi, ‘The overlapping crack model for uniaxial and eccentric concrete compression tests’, in *Magazine of concrete research*, Vol. 61, 9 (Thomas Telford Ltd, 2009), pp. 745–757.

- <sup>63</sup>A. Carpinteri, M. Corrado, G. Mancini, and M. Paggi, ‘A numerical approach to modelling size effects on the flexural ductility of rc beams’, in *Materials and structures*, Vol. 42, 10 (Springer, 2009), pp. 1353–1367.
- <sup>64</sup>F. Indelicato and M. Paggi, ‘Specimen shape and the problem of contact in the assessment of concrete compressive strength’, in *Materials and structures*, Vol. 41, 2 (Springer, 2008), pp. 431–441.
- <sup>65</sup>A. Carpinteri and M. Corrado, ‘An extended (fractal) overlapping crack model to describe crushing size-scale effects in compression’, in *Engineering failure analysis*, Vol. 16, 8 (Elsevier, 2009), pp. 2530–2540.
- <sup>66</sup>F. Accornero, R. Cafarelli, and A. Carpinteri, ‘Cracking and crushing in prestressed concrete beams’, in *Aci structural journal*, Vol. 118, 2 (American Concrete Institute, 2021), pp. 101–109.
- <sup>67</sup>F. Accornero, R. Cafarelli, and A. Carpinteri, ‘The cohesive/overlapping crack model for plain and rc beams: scale effects on cracking and crushing failures’, in *Magazine of concrete research* (Thomas Telford Ltd, 2021), pp. 1–18.
- <sup>68</sup>A. Carpinteri and M. Corrado, ‘Upper and lower bounds for structural design of rc members with ductile response’, in *Engineering structures*, Vol. 33, 12 (Elsevier, 2011), pp. 3432–3441.
- <sup>69</sup>G. Ruiz, M. Elices, and J. Planas, ‘Size effect and bond-slip dependence of lightly reinforced concrete beams’, in *European structural integrity society*, Vol. 24 (Elsevier, 1999), pp. 67–97.
- <sup>70</sup>I. F. for Structural Concrete, *Fib model code for concrete structures 2010*, 2013.
- <sup>71</sup>I. The Mathworks, *The mathworks, inc. matlab*, version 2021a, Mar. 17, 2021.
- <sup>72</sup>G. V. Rossum, *Python software foundation. python language reference, version 2.7*, 1995.
- <sup>73</sup>R. De Borst, M. A. Crisfield, J. J. Remmers, and C. V. Verhoosel, *Nonlinear finite element analysis of solids and structures* (John Wiley & Sons, 2012).

- <sup>74</sup>V. Tvergaard and A. Needleman, ‘Analysis of the cup-cone fracture in a round tensile bar’, in *Acta metallurgica*, Vol. 32, 1 (Elsevier, 1984), pp. 157–169.
- <sup>75</sup>V. Tvergaard, ‘Influence of void nucleation on ductile shear fracture at a free surface’, in *Journal of the mechanics and physics of solids*, Vol. 30, 6 (Elsevier, 1982), pp. 399–425.
- <sup>76</sup>A. Needleman, ‘An analysis of tensile decohesion along an interface’, in *Journal of the mechanics and physics of solids*, Vol. 38, 3 (Elsevier, 1990), pp. 289–324.
- <sup>77</sup>X.-P. Xu and A. Needleman, ‘Numerical simulations of fast crack growth in brittle solids’, in *Journal of the mechanics and physics of solids*, Vol. 42, 9 (Elsevier, 1994), pp. 1397–1434.
- <sup>78</sup>D. Ngo and A. C. Scordelis, ‘Finite element analysis of reinforced concrete beams’, in *Journal proceedings*, Vol. 64, 3 (1967), pp. 152–163.
- <sup>79</sup>P. Wawrzynek and A. Ingraffea, ‘Franc2d: a two-dimensional crack propagation simulator. version 2.7: user’s guide’, in (1994).
- <sup>80</sup>P. Bocca, A. Carpinteri, and S. Valente, ‘Mixed mode fracture of concrete’, in *International journal of solids and structures*, Vol. 27, 9 (Elsevier, 1991), pp. 1139–1153.
- <sup>81</sup>A. R. Ingraffea and V. Saouma, ‘Numerical modeling of discrete crack propagation in reinforced and plain concrete’, in *Fracture mechanics of concrete: structural application and numerical calculation* (Springer, 1985), pp. 171–225.
- <sup>82</sup>J. G. Rots, ‘Smearred and discrete representations of localized fracture’, in *Current trends in concrete fracture research* (Springer, 1991), pp. 45–59.
- <sup>83</sup>T. J. Truster, ‘Deip, discontinuous element insertion program—mesh generation for interfacial finite element modeling’, in *Softwarex*, Vol. 7 (Elsevier, 2018), pp. 162–170.
- <sup>84</sup>V. P. Nguyen, ‘An open source program to generate zero-thickness cohesive interface elements’, in *Advances in engineering software*, Vol. 74 (Elsevier, 2014), pp. 27–39.

- <sup>85</sup>K. C. Koppenhoefer, A. S. Gullerud, C. Ruggieri, R. H. Dodds Jr, and B. Healey, *Warp3d: dynamic nonlinear analysis of solids using a preconditioned conjugate gradient software architecture*, tech. rep. (University of Illinois Engineering Experiment Station., 1994).
- <sup>86</sup>P. Bocca, A. Carpinteri, and S. Valente, ‘Size effects in the mixed mode crack propagation: softening and snap-back analysis’, in *Engineering fracture mechanics*, Vol. 35, 1-3 (Elsevier, 1990), pp. 159–170.
- <sup>87</sup>A. Castigliano, *Théorie de l’équilibre des systèmes élastiques et ses applications*, Vol. 1 (AF Negro, 1879).